Regarding the Role of Aggregation and Structural Order on the Mechanism of Molecular Doping of Semiconducting Polymers:

From Solutions to Films

Dissertation

zur Erlangung des akademischen Grades
doctor rerum naturalium (Dr. rer. nat.)
in der Wissenschaftsdisziplin Polymer Science

Eingereicht an der
Mathematisch-Naturwissenschaftlichen Fakultät
der Universität Potsdam

von

Malavika Arvind

Tag der Disputation: 26.02.2021

Supervisor: Prof. Dr. Dieter Neher

Reviewers: Prof. Dr. Thuc-Quyen Nguyen

Prof. Dr. Sabine Ludwigs

Prof. Dr. Dieter Neher

https://doi.org/10.25932/publishup-50060
https://nbn-resolving.org/urn:nbn:de:kobv:517-opus4-500606

Abstract

Polymeric semiconductors are strong contenders for replacing traditional inorganic semiconductors in electronic applications requiring low power, low cost and flexibility, such as biosensors, flexible solar cells and electronic displays. *Molecular doping* has the potential to enable this revolution by improving the conductivity and charge transport properties of this class of materials. Despite decades of research in this field, gaps in our understanding of the nature of dopant–polymer interactions has resulted in limited commercialization of this technology. This work aims at providing a deeper insight into the underlying mechanisms of molecular p-doping of semiconducting polymers in the solution and solid-state, and thereby bring the scientific community closer to realizing the dream of making organic semiconductors commonplace in the electronics industry. The role of 1) dopant size/shape, 2) polymer chain aggregation and 3) charge delocalization on the doping mechanism and efficiency is addressed using optical (UV-Vis-NIR) and electron paramagnetic resonance (EPR) spectroscopies. By conducting a comprehensive study of the nature and concentration of the doping-induced species in solutions of the polymer poly(3-hexylthiophene) (P3HT) with 3 different dopants, the unique optical signatures of the *delocalized polaron*, *localized polaron* and *charge-transfer complex* are identified and their extinction coefficient values are reported. Furthermore, with X-ray diffraction, atomic force microscopy and electrical conductivity measurements, the impact of processing technique and doping mechanism on the morphology and thereby, charge transport through the doped films is studied.

This work demonstrates that the doping mechanism and type of doping-induced species formed are strongly influenced by the *polymer backbone arrangement* rather than dopant shape/size. The ability of the polymer chain to aggregate is found to be crucial for efficient charge transfer (ionization) and polaron delocalization. At the same time, our results suggest that the high ionization efficiency of a dopant–polymer system in *solution* may subsequently hinder efficient charge transport in the *solid-state* due to the reduction in the fraction of *tie chains*, which enable charges to move efficiently between aggregated domains in the films. This study demonstrates the complex multifaceted nature of polymer doping while providing important hints for the future design of dopant-host systems and film fabrication techniques.

Zusammenfassung

Polymer-Halbleiter sind vielversprechende Kandidaten für den Ersatz traditioneller anorganischer Halbleiter in elektronischen Anwendungen, die einen geringen Stromverbrauch, niedrige Kosten und mechanische Flexibilität erfordern, wie z.B. Biosensoren, flexible Solarzellen und elektronische Bildschirme. Molekulare Dotierung hat das Potenzial, diese Revolution zu ermöglichen, indem sie die Leitfähigkeit und die Ladungstransporteigenschaften dieser Materialklasse verbessert. Trotz jahrzehntelanger Forschung auf diesem Gebiet hat das unvollständige Verständnis der Dotierstoff-Polymer-Wechselwirkungen nur zu einer begrenzten Kommerzialisierung dieser Technologie geführt.

Ziel dieser Arbeit ist es, einen tieferen Einblick in die zugrunde liegenden Mechanismen der molekularen p-Dotierung von halbleitenden Polymeren in Lösung und im festen Zustand zu geben und dadurch die wissenschaftliche Gemeinschaft näher an die Verwirklichung des Traums heran zu bringen, organische Halbleiter in der Elektronikindustrie alltäglich zu machen. Wir befassen uns mit der Rolle 1) der Größe/Form des Dotierstoffs, 2) der Polymerkettenaggregation und 3) der Ladungsdelokalisierung für den Dotierungsmechanismus und die Effizienz unter Verwendung optischer (UV-Vis-NIR) und elektronenparamagnetischer Resonanz (EPR) Spektroskopie. Mit Hilfe einer umfassenden Studie über die Art und Konzentration der dotierungsinduzierten Spezies in Lösungen des Polymers Poly(3-hexylthiophen) (P3HT) mit verschiedenen Dotierstoffen identifizieren wir die eindeutigen optischen Signaturen des delokalisierten Polarons, des lokalisierten Polarons und des Ladungstransferkomplexes und berichten die Werte ihrer Extinktionskoeffizienten. Außerdem untersuchen wir mittels Röntgenbeugung, Rasterkraftmikroskopie und elektrischen Leitfähigkeitsmessungen den Einfluss der Verarbeitungstechnik und des Dotierungsmechanismus auf die Morphologie und damit auf den Ladungstransport durch die dotierten Filme.

Diese Arbeit zeigt, dass der Dotierungsmechanismus und die Art der gebildeten, dotierungsinduzierten Spezies eher durch die Anordnung des Polymerrückgrats als durch die Form/Größe des Dotierstoffs beeinflusst werden. Die Fähigkeit der Polymerkette, zu aggregieren, stellt sich als entscheidend für einen effizienten Ladungstransfer (d.h. Ionisierung) und die Polaron-

Delokalisierung heraus. Gleichzeitig deuten unsere Ergebnisse darauf hin, dass die hohe Ionisationseffizienz eines Dotierstoff-Polymersystems in der Lösung eine Beinträchtigung des effizienten Ladungstransport im festen Zustand nach sich ziehen kann, da der Anteil der Verbindungsketten, die eine effiziente Bewegung von Ladungen zwischen aggregierten Domänen in dünnen Filmen ermöglichen, reduziert wird. Diese Arbeit verdeutlicht die komplexe, vielschichtige Natur der Polymerdotierung und gibt dabei wichtige Hinweise für das zukünftige Design von Dotierstoff-Wirtssystemen und Filmherstellungstechniken.

Contents

1. Introduction

Semiconductors are ubiquitous in today's world. Following the boom in smartphone technology, the past decade saw the birth of the *Internet of Things* (IoTs), with the ratio of devices/people connected to the internet increasing from 0.08 in 2003, to 1.84 in 2010.[1] This is mostly credited to advancements in low-power, low-cost semiconductor technology. Estimates say that by the year 2025, there will be more than 21 billion IoT devices worldwide. Currently, the *inorganic semiconductor* silicon makes up the majority of the microprocessors and sensors in the consumer electronics and IoT industry. Although silicon is the second most abundant element on the earth, the extraction and purification process is energy and cost intensive. Moreover, silicon and other conventional inorganic semiconductors are typically rigid and brittle in nature, which limits their scope of application in areas such as wearables and bioelectronics[2]. This calls for alternate low cost, flexible materials, which are suitable for mass production.[3] Polymers are ideal candidates.

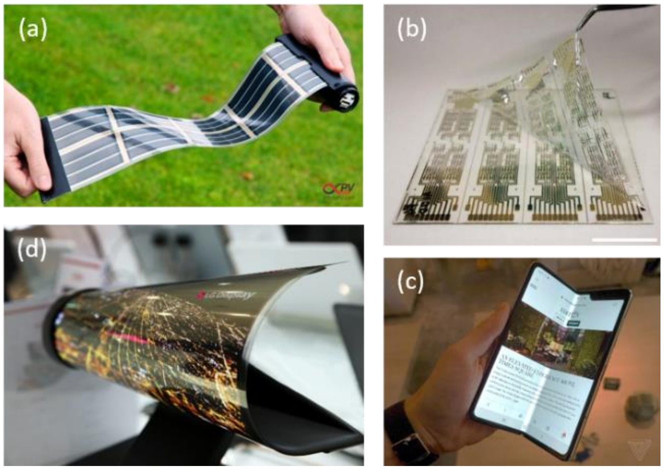

Figure 1.1. (a) HeLi-On: a pocketable flexible solar panel from infinityPV.[4] (b) An organic CMOS (complementary metal oxide semiconductor) logic circuit deposited on a 1μm thin substrate by Takeda et al.[5] (c) Samsung Galaxy Fold: a flagship device with a flexible 7.5" display.[6] (d) LG Display's 18" rollable OLED TV prototype presented in the CES 2016 conference.[7]

A unique advantage of organic/polymeric materials is the ability to finely tune their properties, already during synthesis. Polymers have replaced traditional materials such as metals and glass across various industries due to their high strength-to-weight ratio, durability and low cost. In the field of electronics however, they were historically only used in auxiliary parts such as circuit boards, cable housings and photoresists, since they were assumed to be exclusively insulating in nature.[8] In the late 1970s, first evidence of an electrically conductive polymer *polyacetylene* was presented by Hideki Shirakawa et al.[9] This paved the way for extensive research in this new class of conductive and semi-conductive organic materials in the following years, and ultimately led to the award of the Nobel Prize in Chemistry to Alan J. Heeger, Alan MacDiarmid and Hideki Shirakawa "*for the discovery and development of conducting polymers*" in the year 2000.[10]

Although polyacetylene itself is not a commercial success, mainly due to its poor processability, the conducting polymer poly(3,4-ethylenedioxythiophene) (PEDOT known commercially as Clevios^{TM}) is available on the market and used for antistatic and conductive coatings.[11] Today, *organic semiconductors* – a class of materials that comprises both organic small molecules as well as polymeric materials – have found applications in devices such as thin film transistors, photovoltaics and light emitting diodes.[12] These devices typically consist of an active semiconducting material sandwiched between conductive electrodes (also known as *transport layers*). Depending on a material's electronic properties, it can either be used as the active element in a device, or as transparent or flexible electrodes which transport charges to/from the active element. Therefore, a crucial requirement is efficient charge transport not only through the active material or electrodes, but also between the active material and the electrodes.[13] This is where organic materials fall behind conventional ones such as silicon. Typically, *charge carriers* (electrons or holes) in organic semiconductors tend to be "trapped" easily, and do not contribute to the conductivity. Additionally, due to their disordered morphology, organic semiconductors have much lower *charge carrier mobility* than inorganic materials. Another disadvantage of organic semiconductors is that most of the currently available materials tend to degrade when exposed to oxygen, humidity, or UV light, which complicates their use in normal environments as such.[14-18]

Doping was the key concept that revolutionized the inorganic semiconductor industry in the last century. Through the introduction of specific materials called *dopants* to the semiconductor, the *type* (electron or hole) and *concentration* of *charge carriers* in the host material could be modified. This allowed for precise control of the electronic properties of the semiconductor, and ultimately led to the development of the *p-n junction*, which is the backbone of all solid-state electronic devices (e.g. diodes and transistors).

The concept of doping also applies to organic semiconductors, and has been known for a long time. In fact, the highly conductive polyacetylene sample reported by Shirakawa in 1977 was doped with iodine.[9] In the initial years of research, halogens and alkali metals were actively employed as dopants for organic semiconductors.[19-23] Despite leading to high conductivity of the doped layers, devices made using these materials often suffered from stability issues due to dopant diffusion.[23-24] Therefore, *molecular dopants* were subsequently developed. Today, we have a plethora of materials ranging from molecular compounds of varying shapes and sizes, to acids and bases that serve as dopants for organic semiconductors.[25] Molecular doping has enabled the fabrication of efficient p-i-n multilayer junctions with ohmic contacts as well as the reduction of losses in the transport layers of organic photovoltaics (OPVs)[26-27] and organic light-emitting diodes (OLEDs)[24, 28]. In organic field-effect transistors (OFETs), aside from improving the conductivity of the contacts, molecular doping has led to increased device stability[29] and reduced threshold voltages.[30-31] Doped organic semiconductor/polymeric films are also effectively used as transport layers in *perovskite solar cells*, which are currently the strongest contenders to replace the traditional silicon-based solar cells.[32-35]

Given the numerous studies in favor of doping-induced improvement in the optoelectronic properties of organic semiconductors over the last two decades, one would expect organic electronic devices (with doped layers) to be commonplace today. However, unlike with doped inorganic semiconductors, stable and reliable doping of organic semiconductors is difficult to achieve. This is because our understanding of the fundamental processes that occur during doping of organic materials is still incomplete.[25]

For example, experimental and theoretical studies during the past years led to the conclusion that there are two mechanisms of charge transfer between the dopant and organic semiconductors – *integer charge transfer* (ICT), in which there is complete transfer of an electron from the host to the dopant or vice versa, and which is analogous to the mechanism in conventional semiconductors, or *charge transfer complex* (CTC) formation, in which the frontier orbitals of the host and the dopant interact, resulting in a partial charge transfer.[36-37] Overall, ICT is preferred over CTC formation, since the latter requires additional thermal or optical excitation for the creation of mobile charge carriers. Yet, the exact factors determining the doping mechanism in some of the dopant-host systems are unknown. Although electronic parameters were initially thought to be the primary determinant, recent publications have highlighted the role of structural order and packing.[38-39]

Another barrier to efficient devices is the lack of morphological control in doped polymer films. A huge advantage of polymeric semiconductors over small molecule organic semiconductors is their ability to be solution processed (unlike the latter, which typically require energy intensive vacuum deposition methods), thereby making them ideal for large scale deposition techniques such as roll-to-roll, inkjet printing etc. However in dopant-polymer solution blends, aside from interactions with the solvent, doping typically induces *polymer chain aggregation*, which negatively impacts the morphology in the film, and subsequently its conductivity.[40] Therefore, a deeper understanding of the processes occurring in solution, will enable a better control of the dopant-polymer interactions, and the morphology in films.

Along with investigating doped solutions, the development of alternative processing techniques, which could potentially avoid the issue of pre-aggregation in solution, is important. Recently, various research groups have reported the use of *sequential doping*, in which the dopant is introduced into a pre-cast polymer film by spin-coating from an *orthogonal solvent* or by vapor deposition in order to obtain homogeneous films with high electrical conductivity.[25, 40-41]

A prototypical p-dopant in the field of organic electronics is 2,3,5,6-tetrafluoro-7,7,8,8-tetracyanoquinodimethane (F_4TCNQ). Despite its success in improving the electronic properties of organic small molecule as well as polymeric semiconductors, it has certain drawbacks such as poor solubility, aggregation at high dopant concentration, and a tendency to easily diffuse through the layers due to its small size.[42] To combat this, scientists have been on the look out for alternative "bulky" dopants. In the last few years, Lewis acids, and in particular trispentafluorophenylborane (BCF), have gained a lot of interest in the field.[43-47] As a part of my master thesis, I investigated BCF doping of the model semiconducting polymer poly(3-hexylthiophene) (P3HT) in its regioregular form and found that BCF doping led to improved film morphology and higher conductivity in comparison to F_4TCNQ doped P3HT films.[48-49] However, there were still many unanswered questions regarding the actual doping mechanism. Another class of materials that are now popular as p-dopants are the organometallic complexes based on molybdenum trisdithiolene ($Mo(tfd)_3$)[50] and its soluble derivatives[35, 51], due to their bulky 3D structure and air stability.

This thesis is aimed at providing further insight into molecular p-doping of semiconducting polymers by studying the role of polymer chain aggregation and structural order on the doping mechanism in solutions as well as films. To that end, the polymeric semiconductor P3HT has been chosen for our studies. This is because, firstly, depending on the *regioregularity* of the polymer batch and the sample preparation conditions, a wide range of chain conformations and film morphologies can be accessed for this polymer.[52-53] For example, *regiorandom* P3HT chains always adopt a coiled conformation in solutions and films due to steric effects, whereas *regioregular* P3HT chains adopt a twisted/ coiled conformation when surrounded by a good solvent, but planarize and aggregate while forming films or in the presence of a poor solvent.[52-53] Secondly, a vast archive of previously conducted research is available for this material,[40-41, 52, 54-59] which serves as an ideal basis for our work.

The primary characterization technique used in this work is *UV-Vis-NIR spectroscopy*. This is a simple but powerful tool which can be used to 1) confirm the occurrence of charge transfer (doping) in a dopant-host system 2) identify the doping mechanism 3) quantify the degree of charge transfer 4) verify the presence of aggregates, in solutions as well as films. A complementary technique to characterize doping is *electron paramagnetic resonance* (EPR) spectroscopy, which is sensitive to the presence of unpaired electrons in the system, as well as the nature/strength of interactions between the unpaired electron and magnetic nuclei in its environment. Therefore, this non-invasive technique is ideal for supplementing and validating the findings from optical spectroscopy. The changes occurring in the morphology and microstructure of the polymeric films upon doping have been investigated using *atomic force microscopy* (AFM) and *grazing incidence X-ray diffraction* (GIXRD), respectively. The corresponding changes in the conductivity of the sample were measured using the *four-point probe* (4PP) technique. Although p- as well as n-doping processes are crucial for devices, this work is restricted to p-doped systems.

This thesis is structured as follows: The important fundamental concepts related to organic semiconductors and doping are explained in Chapter 2. In Chapter 3, the experimental techniques used to study the doped systems are explained, along with a description of the host and dopant materials used, and the general sample preparation methods. Chapters 4 – 6 contain the main results and discussions of this work. First, the influence of external parameters such as light and pre-aggregation on polaron formation in BCF doped P3HT solutions is discussed in Chapter 4.

Following this, a detailed study on the nature of the optical signatures observed in p-doped P3HT solutions with 3 different dopants is presented in Chapter 5. Finally, the impact of dopant and processing technique on the morphology and charge transport in doped films is discussed in Chapter 6. The important findings of this work are summarized in Chapter 7.

2. Fundamental Concepts

In this chapter, the important concepts needed for the understanding of the work presented in this thesis, are explained. Since the backbone of this thesis pertains to organic semiconductors, we first try to understand what allows certain organic compounds to be semiconductors, followed by the ideal morphology in films, and the impact on charge transport and conductivity in organic/polymeric thin films. Then, the theory and mechanism of doping in organic semiconductors is explained, along with a description of the p-dopants widely used in the community. Finally, the different techniques for making doped films, and the implications on the electronic or morphological properties are discussed. A more detailed explanation of the concepts and ideas presented in this chapter can be found in the various textbooks[8, 12, 55, 60] and review articles[25, 31, 61] that have been used as reference.

2.1 Organic Semiconductors

Organic compounds are materials based on hydrocarbons, which often also contain other heteroatoms such as oxygen, sulfur and nitrogen. As a result of its low atomic size, and intermediate electron affinity, carbon exhibits the property of "*catenation*", which is the affinity towards bonding with other carbon atoms, thereby leading to a vast repository of chemicals with straight, branched, or cyclic chains, of varying lengths and chemical/physical properties. *Polymers* are a sub-set of this class of materials and consist of long chains of hydrocarbons made of repeating units.

Organic semiconductors are organic compounds which are semiconducting in nature i.e. they are able to conduct electricity under certain conditions (vide infra). Organic semiconductors can be further classified into small molecule or polymeric semiconductors, based on the molecular weight and length of the chain. While inorganic semiconductors are made of *covalently* bonded atoms in a crystalline lattice structure, organic semiconductors comprise of molecules which interact via the weaker *van der Waals* force. As a result of this, the classical *band theory* used to describe inorganic semiconductor physics does not entirely hold true for organics. In order to understand the semiconducting properties of organic molecules, we first need to look at the electronic structure of carbon.

2.1.1 Electronic Structure and Energy Levels

Carbon contains a total of six electrons in its ground state (electronic configuration $1s^2 2s^2 2p^2$), four of which are in the valence shell ($2s^2 2p^2$) and able to form bonds with other atoms. When covalently bonding with another atom, the valence s- and p-orbitals linearly combine after some energetically favorable rearrangement, to form new *hybrid orbitals*. These hybridized orbitals are called sp, sp^2, or sp^3, depending on whether the 2s orbital combines with one, two, or all three of the 2p orbitals. For semiconductors, the sp^2 hybridized orbital is most relevant. Here, one s-orbital combines with two p-orbitals (e.g. p_x, p_y) to form three sp^2 hybridized orbitals, whereby the four valence electrons individually occupy the three sp^2 orbitals (which are degenerate) and the remaining p_z-orbital. The three hybridized sp^2 orbitals are coplanar and the p-orbital is perpendicular to this plane. The simplest case of a molecule with sp^2 hybridization is ethylene ($CH_2{=}CH_2$), shown in Figure 2.1. When the sp^2 orbitals of two C atoms overlap, it leads to the formation of a strong, localized covalent σ-bond. Similarly, the other two sp^2 hybridized orbitals of each C atom form localized σ-bonds with the s-orbitals of two H atoms. The remaining p_z-orbitals (which are perpendicular to the plane of the σ-bonds) overlap above and below this plane to form a π-bond, thereby resulting in a double bond between the C atoms.[12]

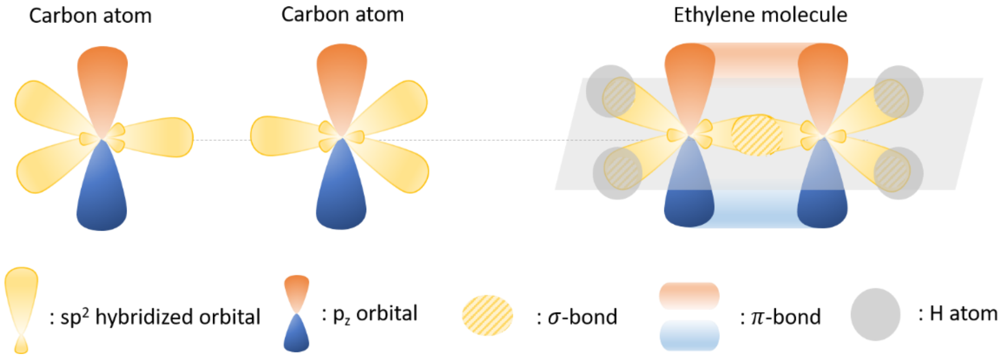

Figure 2.1. Scheme of the orbitals in an sp^2 hybridized C atom, and the covalent bonding between two such sp^2 hybridized C atoms to form an ethylene molecule, with σ -bonds on the nodal plane and a π-bond above and below the plane.

The formation of the *molecular orbitals* can be described by the theory of *linear combination of atomic orbitals* (LCAO). When two atomic orbitals overlap, two molecular orbitals (MOs) with different energies are formed (see Figure 2.2). The lower energy state is known as the *bonding* (σ or π) MO, since it is formed by constructive interference of the atomic orbital wavefunctions and leads to a stable bond between the two nuclei. On the contrary, when destructive interference of the atomic orbital wavefunctions occurs between the nuclei, an *anti-bonding* (σ* or π*) MO with a higher energy is formed. Since σ-bonds are characterized by strong orbital overlap, the σ bonding and anti-bonding (σ*) orbitals are energetically far apart. However, since π-bonds lie farther away from the nuclei and have a lower degree of overlap between the p-orbitals, the corresponding π bonding and π^* anti-bonding orbitals lie energetically closer to each other. Therefore, in a molecular system containing π-bonds, the π- and π^*- orbitals are the *highest occupied molecular orbital* (HOMO) and the *lowest unoccupied molecular orbital* (LUMO), respectively. The corresponding electronic transition $\pi \rightarrow \pi^*$ has the lowest energy, and this energy difference is known as the *band gap* (E_G) of the material, analogous to the terminology used in inorganic semiconductor physics. The HOMO and LUMO of a conjugated molecule are known as the *frontier orbitals*, since they play an important role in determining the optical and electrical properties of the system. When the band gap is low enough that electrons from the HOMO can be excited to the LUMO by thermal or optical energy, the material becomes semiconducting in nature.[60]

If we consider the bonding between a series of sp^2 hybridized carbon atoms, planar σ-bonds formed by strong wavefunction overlap constitute the backbone of the molecule, whereas the (weaker) overlap between the remaining p_z-orbitals leads to the formation of π-bonds wherein the electrons are delocalized over many carbon atoms. Such a system consisting of delocalized electrons is known as a *conjugated* system. Increase in the *conjugation length* results in a monotonic decrease in the band gap, as the HOMO and LUMO come closer together. This is illustrated in Figure 2.2.

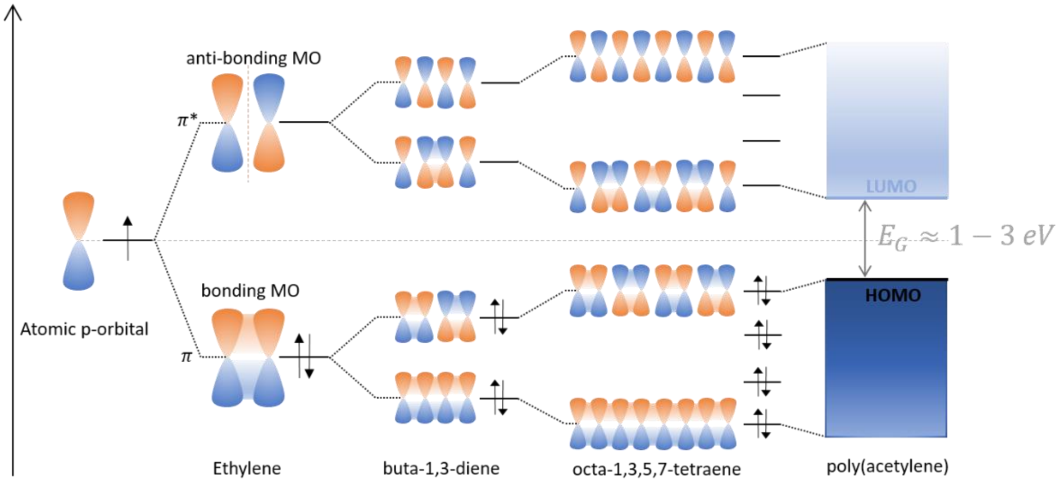

Figure 2.2. Illustration showing the linear combination of atomic (p_z) orbitals (LCAO) of carbon to form bonding (π) and anti-bonding (π*) molecular orbitals (MOs) in ethylene, butadiene, etc. The energetic gap between the bonding and anti-bonding orbitals decreases with increasing number of carbon atoms, ultimately forming two "bands" analogous to the conduction and valence bands of inorganic materials. Due to Peierls instability, conjugated polymers such as polyacetylene have a finite band gap instead of being "metal-like".

In a *conjugated polymer* such as polyacetylene, which can be modeled as an infinitely long chain of sp^2 hybridized carbon atoms, this would imply the absence of a band gap and therefore a "metal"-like behavior. However, such quasi one-dimensional systems are structurally unstable, as stated in *Peierls' Theorem.*[62] Instead of having a linear structure with uniform bond length between the carbon atoms in the chain, polyacetylene chains in reality have alternating short and long bonds, which leads to a finite band gap in the range of 1.5-3 eV. Therefore, conjugated polymers show semiconducting behavior instead of conducting behavior. Moreover, in real samples, conjugation is typically interrupted due to chemical defects/impurities as well as folds or kinks in the polymeric chains.[12] Therefore, the system is effectively a group of molecules of varying conjugation lengths, also known as *chromophores*. A direct consequence of this is a distribution of energy levels in the system, in which the ensemble of bonding/anti-bonding levels can be compared to the *valence/ conduction bands* (VB or CB) in inorganic semiconductors, respectively.

2.1.2 Morphology in Films

Although a highly conjugated hydrocarbon backbone is beneficial for charge transport, the resulting chain stiffness significantly reduces the processability of these materials. For this reason, flexible alkyl side chains which improve the solubility, are typically introduced into the material during synthesis. In many cases, specific heteroatoms or functional groups are also included in the structure in order to modify the position of the HOMO or LUMO, or impart a specific functionality.[8] Organic semiconductor films are fabricated either by vapor deposition under vacuum (only viable for small molecules), or via solution processing. When forming films, the nature and structure of these side chains and functional groups impact the *lamellar*- (vertical) and *π-stacking* (co-facial) distances between the backbone (see Figure 2.3), which in turn influences the final morphology, and charge transport in the film.[63]

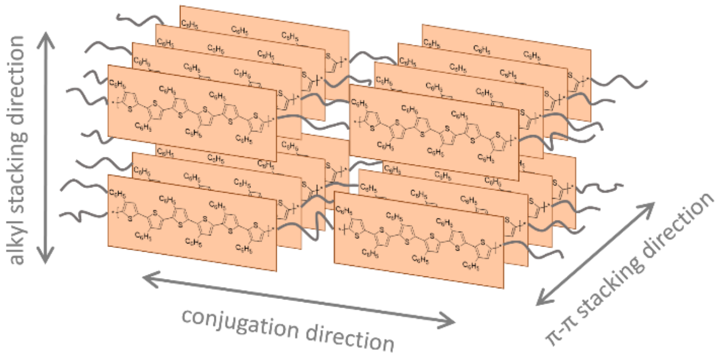

Figure 2.3. Schematic representation of "edge-on" oriented regioregular P3HT chains, showing the conjugation direction, the lamellar stacking direction and π-π stacking direction of the chains. (Redrawn after [64])

Due to the complex chemical structures and weak van der Waals forces holding the molecules or chains together, organic semiconductors can exhibit a vast range of morphologies in the solid state. A perfectly crystalline microstructure is nearly impossible to achieve, particularly for polymers, which have a distribution of molecular weights (chain lengths). Therefore, most organic semiconductors can be thought of as crystalline domains dispersed in an amorphous matrix, or vice versa. The size of the domains will vary depending on the *degree of crystallinity* of the sample.

The conjugated polymer P3HT has been studied extensively in this field, primarily due to the ease of control during synthesis and processing of this material. Since the monomer 3-hexyl thiophene is an asymmetrical molecule, *regioisomers* are formed upon its polymerization. When coupling between repeating units is predominantly of a *head-to-tail* (HT) nature, the resulting polymer is called regioregular P3HT (rreP3HT) (see Figure 2.4). RreP3HT is able to self-organize to form highly ordered structures since the backbone consists of fully conjugated sp^2 hybridized C atoms, which leads to a planar backbone morphology and π-stacking between adjacent chains. However, when the coupling is more irregular (a mixture of head-to-head, tail-to-tail and HT), the alkyl side-groups which are too close to each other experience steric repulsion, thereby leading to twisting or coiling of the polymer backbone at these sites, as shown in Figure 2.4. Consequently, these irregular polymer chains have reduced conjugation lengths, and are unable to form highly ordered structures. Regiorandom P3HT (rraP3HT), a material with highly irregular couplings, is an amorphous polymer.[55]

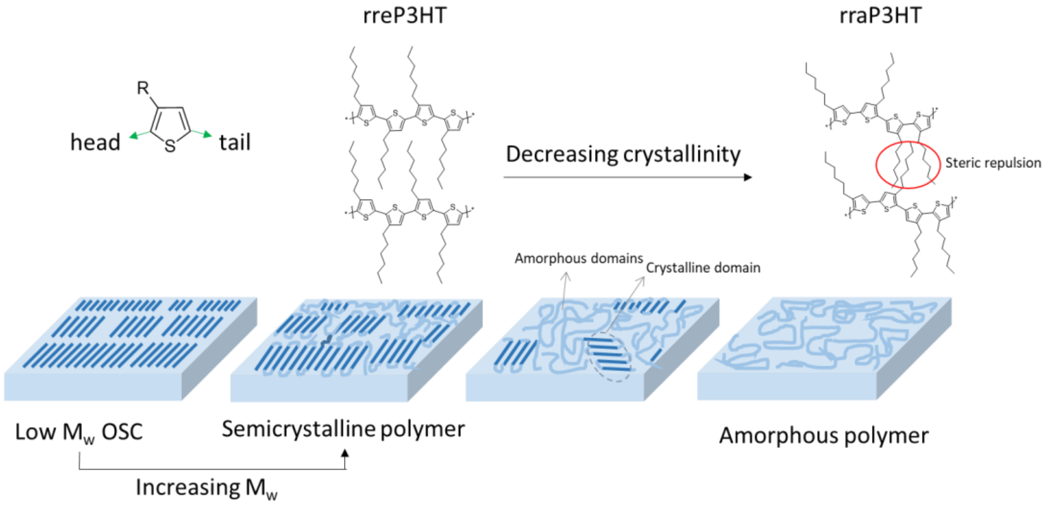

Figure 2.4. Illustration of the impact of molecular weight and microstructure on the film morphology.

The average molecular weight[a] of an organic semiconductor also impacts the morphology in films.[65] Spin coated low molecular weight (<10 kg mol^{-1}) rreP3HT has a well-defined nanorod

---

[a] The molecular weight of polymers is typically reported as an *average* rather than a single value, due to the difference in chain lengths within a sample. Therefore, depending on whether the *number fraction* of chains or the *weight fraction*

morphology,[66] whereas higher molecular weight P3HT (ca. 27 kg mol^{-1}) produces a less defined morphology.[67] Remarkably, it was found that these films with higher molecular weight had significantly improved charge transport despite the reduction in order. This is attributed to the presence of *tie chains*, which are long chains that connect two or more crystalline domains in these samples, thereby facilitating improved macroscopic charge transport. In the low molecular weight films on the other hand, the charges remain trapped at the grain boundaries (see Figure 2.5).[68]

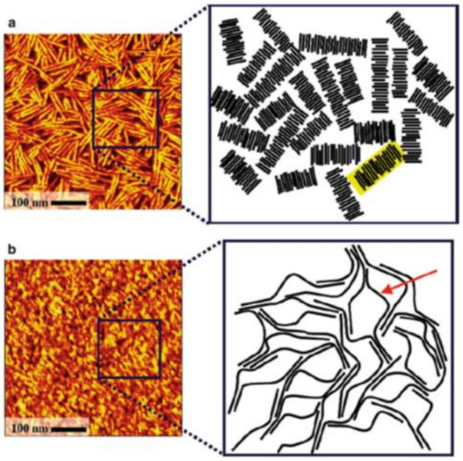

Figure 2.5. Morphology of spin-coated P3HT films showing a) well-defined but disconnected ribbons in the case of a low molecular weight (M_n < 4 kg mol^{-1})[a] sample and b) less-defined arrangement of chains in a high molecular weight (M_n > 30 kg mol^{-1})[a] sample, in which the crystalline domains are connected by tie chains (indicated by the red arrow). [Reproduced from Kline et al.[68] Copyright (2005) American Chemical Society]

Apart from the chemical composition and structure, the film processing conditions also influence the microstructure. The solvent polarity, boiling point, deposition technique, as well as substrate surface properties have all been shown to impact film morphology and subsequently, the optoelectronic and charge transport properties of solution processed films.[69] For example, atomic force microscopy (AFM) and X-ray diffraction (XRD) measurements have shown that P3HT films spin coated from chloroform (CF, boiling point ca. 62°C) have a less ordered microstructure when compared to films spin coated from higher boiling point solvents such as trichlorobenzene (TCB, boiling point ca. 219°C).[70] This is attributed to the P3HT chains having more time to self-organize

---

of chains is considered for the calculation, either the *number average molecular weight* (M_n) or the *weight average molecular weight* (M_w) is obtained, respectively.

(aggregate) into the thermodynamically preferred crystalline motif in the slow evaporating TCB.[70] Park et al. demonstrated that the addition of a small amount of a non-solvent to the well-dissolved polymer solution prior to film casting induced additional chain aggregation.[71] Various groups have also demonstrated the use of post-processing techniques such as solvent annealing[72-73], and thermal annealing[74-75] to increase the size of the crystalline domains in polymer films.

2.1.3 Charge Transport and Conductivity

All modern optoelectronic devices such as solar cells, light emitting diodes, and field effect transistors operate on the basis of *charge transport*. In order to effectively employ organic semiconductors in these devices, it is crucial to understand how charges move in these materials, and how charge transport differs from that in inorganic systems. The main reason for increased operational complexity in organic semiconductors can be attributed to the structural disorder (and thereby energetic disorder) in these materials. As a result of the weak van der Waals forces between the molecules (versus the covalently bonded crystal structure in inorganics), charged organic semiconductors are subject to *polarization effects*. When an electron is added to, or removed from a LUMO or HOMO, respectively, the adjacent units undergo deformation to accommodate and compensate for the new charge. This occurs in a series of steps, as depicted in Figure 2.6. First, the charge induces dipoles (*electronic polarization*) in the adjacent molecules, thereby stabilizing itself. This is followed by *intramolecular relaxation*, upon which the electronic levels (HOMO/ LUMO) and the nuclei within the molecules undergo reorganization. In the final step, the lattice structure surrounding the charge gets distorted (*lattice relaxation*) in order to stabilize the polarized system. These effects imply that a moving charge in an organic semiconductor is not identical to a conventional free charge carrier, which isn’t accompanied by structural and energetic distortions. This quasi-particle comprising a moving charge and the polarization around it is called a *polaron*. Since these particles have a higher effective mass than a free electron (or hole), their Coulombic binding energy will also be higher.

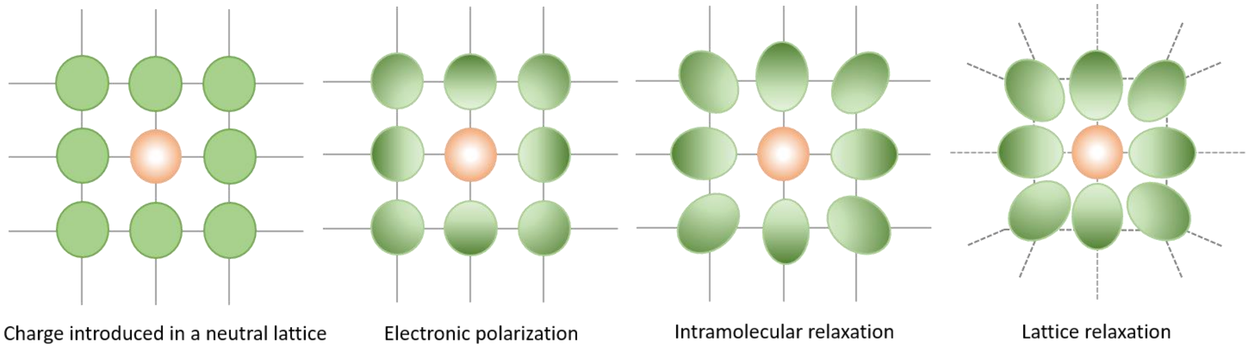

Figure 2.6. Schematic illustration of the polarization and subsequent relaxation processes of the molecules in an organic semiconductor lattice upon the introduction of a charge (orange). [Redrawn after [76]]

There are different models that propose how charge transport occurs, depending on the degree of order in the system. To keep the discussion relevant to this thesis, we will focus on just two of them – *band transport* and *hopping transport*. Perfect crystals, as seen in metals and conventional semiconductors, exhibit band transport since their wavefunctions are delocalized over the entire system, thereby allowing free charge carriers to move uninterrupted in a wave through the material. In this regime, charge transport is inhibited by increase in temperature, as lattice vibrations (phonons) reduce the mean free path of the charge carriers. Highly pure small molecule organic semiconductor crystals of naphthalene and TIPS-pentacene have also been shown to have band-like transport.[77-78] In less pure samples, the presence of impurities or defect states at grain boundaries disrupt transport by "trapping" the charge carrier, since the wavefunctions are localized at these positions. This hinders charge transport. The impurities and defects also increase the disorder in the material, which results in a distribution of the available *density of states* (DOS) for the charge carrier. In organic semiconductors, the DOS is commonly described by a Gaussian distribution model that was developed by Bässler et al. (see Figure 2.7).[79]

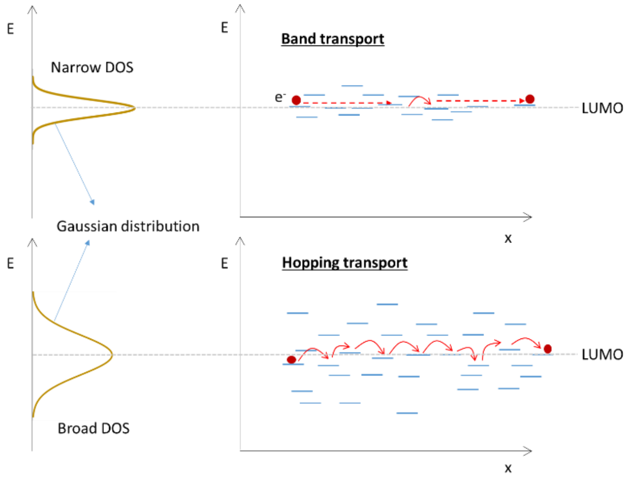

Figure 2.7. A simplified illustration of band transport and hopping transport processes in materials having a narrow and broad Gaussian distribution of the density-of-states (DOS), respectively.

Most organic semiconductors, and in particular conjugated polymers, have a higher degree of disorder than that in pure crystals, and hence, a broader DOS. Therefore, an alternate model is used, in which thermally assisted charge tunneling (or "hopping") takes place. In these materials, charge carriers move coherently within the chromophore, but "hop" from one chromophore to another. Conversely, in non-conjugated systems (such as poly(vinyl carbazole)), transport occurs purely via the hopping process.[8] Whereas band transport is *phonon inhibited*, hopping transport is a *phonon assisted* process, since the additional energy can help in overcoming the energetic barrier.

An important parameter for characterizing charge transport is *charge carrier mobility* (μ), which describes the mean drift velocity (v_D) of a charge carrier (electron or hole) under the influence of an externally applied electric field (E).

$$\mu = \frac{v_D}{E} \tag{2.1}$$

Since the mobility of charges through a material depends on a number of factors such as temperature, degree of order, presence of impurities, electric field, etc., a wide range of values can be expected for different material classes and microstructures. At room temperature (300K), crystalline silicon exhibits charge carrier mobility values in the order of $10^2 – 10^3$ cm^2 V^{-1} s^{-1}.[80] In highly ordered single crystals of rubrene, charge carrier mobility values of 20 – 30 cm^2 V^{-1} s^{-1} using FET measurements have been reported.[81] On the other hand, the charge carrier mobility in polymeric semiconductors range from ca. 10^{-6} – 10^{-3} cm^2 V^{-1} s^{-1} in disordered systems to ca. 0.1 cm^2 V^{-1} s^{-1} (via FET) in materials that are able to self-organize into ordered structures.[54, 82]

The charge transport through a material is described on a macroscopic level by its conductivity (σ) value. Mobility relates to the conductivity of the material according to the relation

$$\sigma = en\mu \tag{2.2}$$

where e is the electron charge and n is the density of charge carriers. Pure, intrinsic organic semiconductors theoretically have a very low density of charge carriers ($n \approx 10^6$ cm^{-3}) on account of their high band gap ($E_g \approx 2.5$ eV) , whereas an intrinsic inorganic semiconductor such as Si ($E_g \approx 1.12$ eV) has a high carrier density ($n \approx 10^{10}$ cm^{-3}). Moreover, organic semiconductors have *dielectric constant*s in the range 3-5, which is about three times lower than that of conventional semiconductors. This means that when charge carriers are generated (for example via light absorption), the corresponding electron and hole pair (known as an *exciton*) will be strongly bound via Coulombic interactions. As a result, organic semiconductors typically have low conductivity values compared to their inorganic counterparts, and hence do not perform well in devices.

2.2 Doping

Doping is a process by which the charge carrier density of electrons or holes (n_e or n_h) in a material is tuned by the controlled addition of certain “impurities” called *dopants*. In inorganic semiconductors, this is done by simply replacing some of the atoms in the lattice structure by another element which has more (n-dopant) or less (p-dopant) electrons in its valence shell compared to the host. For example, silicon, which has 4 valence electrons is commonly n-doped by introducing phosphorus (5 valence electrons), or p-doped using boron (3 valence electrons). This results in an increase in the carrier density (n_e or n_h) and subsequently, the conductivity of the material.

With the discovery of organic semiconductors, similar methods of doping were attempted on these materials in order to tune their electronic properties. It is important to note that the term “doping” when used in the context of organic semiconductors actually refers to redox reactions between the dopant and host, also known as *chemical doping*. Early studies report high conductivities in phthalocyanines doped with strongly oxidizing halogen gases such as iodine and bromine.[19-20] Low work function metals such as lithium and its complexes were also used to dope organic films.[21, 23] However, device instability due to dopant diffusion was a recurring problem in systems doped with very small molecules,[23] and hence led to the development of larger, more stable *molecular dopants*. Today, molecularly doped organic layers have been successfully used in devices such as OLEDS, OPVs, and perovskite solar cells, in order to reduce injection barriers at electrode interfaces, or to improve charge transport by reducing ohmic losses.[83] Yet, they have not been exploited to their full potential, due to the gaps in our understanding of the true doping mechanism in these systems. Extensive research on doped organic semiconductors in the last few decades has shown that since organic and inorganic semiconductors are fundamentally quite different, the mechanism of doping also differs. In the following sections, the processes involved in doping organic semiconductors will be explained.

2.2.1 Theory and Mechanism of Doping

Mobile charge carrier generation in a material via doping is typically a two-step process. In the first step, an electron is transferred from the HOMO (LUMO) of the host to the LUMO (HOMO) of the p- (n-) dopant, to form two charged species, which are Coulombically bound to each other because of the low dielectric constant (refer Figure 2.8). In the second step, the two charges dissociate by overcoming the Coulombic attraction, and contribute to conduction through the material. In doped inorganic semiconductors, charge dissociation takes place readily due to the higher dielectric constant and hence lower binding energy when compared to organics. For example, the binding energy of an e^--h^+ pair in silicon (ϵ_r ~ 11) is ~ 30 meV,[84] which is close to the thermal energy (k_BT) at room temperature (~ 25 meV[12]). Therefore, the free carrier density, and thereby conductivity is high, even at very low concentrations of doping. On the other hand, the binding energy of an e^--h^+ pair in organic semiconductors (ϵ_r ~ 3.5) is in the order of 300 meV,[12] which implies a much lower concentration of free carriers, for the same conditions. Therefore, it is common to have much higher dopant concentrations in organic semiconductors, in contrast to inorganic semiconductors.

Two important parameters used to characterize a doped system are *ionization efficiency*, which is the fraction of added dopants that are ionized to form holes or electron on the host, and *doping efficiency*, which is the fraction of added dopants that result in free charge carriers in the system. In an ideal doped system, these two values will be equal. However, in typical doped conjugated polymers, the doping efficiency is found to be far lower than the ionization efficiency, as a result of the strong Coulombic interaction between the charge on the polymer and the counter-ion on the dopant.[36]

The charge transfer mechanism in doped organic semiconductors is explained using two models – the *integer charge transfer* (ICT) model (also referred to as ion-pair formation), and the *charge transfer complex* (CTC) model (or hybrid charge transfer model). In ICT, an electron is completely transferred from the host to the dopant (or vice versa), resulting in the formation of charged species (holes or electrons). This is predominantly thought to occur in materials having suitable energetic alignment as follows,

$$\begin{aligned} \mathrm{p-doping:}\quad & IE_{host} < EA_{dopant} \\ \mathrm{n-doping:}\quad & EA_{host} < IE_{dopant} \end{aligned} \tag{2.3}$$

where IE is the ionization energy, which is the amount of energy required to remove an electron from the HOMO into vacuum, and EA is the electron affinity, which is the amount of energy gained by the addition of an electron to the LUMO of the host or the dopant.

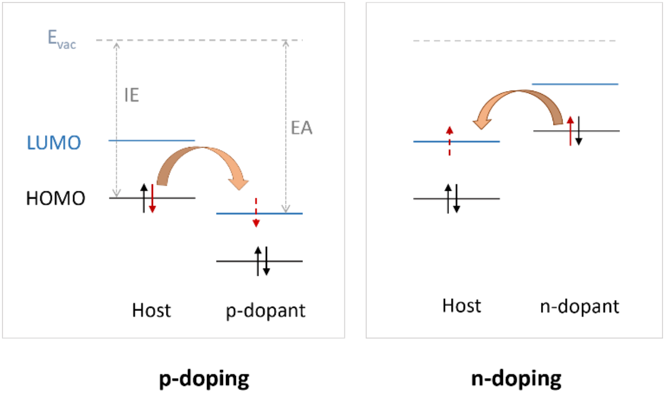

Figure 2.8. Schematic of the charge transfer process between the host and dopant in the case of p-type and n-type molecular doping, showing the ideal energy level alignment for efficient charge transfer.

In certain host – dopant systems however, it has been found that the frontier molecular orbitals of the two materials undergo hybridization to form a ground-state charge transfer complex, which has a new set of HOMO and LUMO states,[37] as shown in Figure 2.9. This implies that systems which do not have favorable energetic alignment between the host's HOMO (LUMO) level and the dopant's LUMO (HOMO) can still undergo charge transfer (doping) via the CTC mechanism. However, since the CTC is still electrically neutral, the system requires additional energy in order to form charged species. At room temperature, only a fraction of the available states are ionized, resulting in a low density of charge carriers. Therefore, for the efficient generation of mobile holes or electrons via doping, ICT is preferred over CTC.[83]

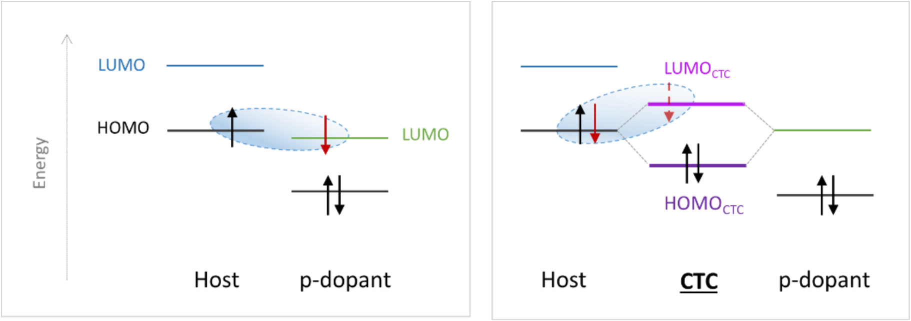

Integer Charge Transfer (ICT)

Charge-Transfer Complex (CTC) formation

Figure 2.9. Schematic of the two prevalent models that are used to explain the mechanism of (p-type) molecular doping of organic semiconductors. In one case, integer charge transfer occurs between the host and dopant. In the alternative model, a charge-transfer complex is formed due to intermixing of the frontier molecular orbitals of the dopant and host. Since the LUMO$_{CTC}$ now lies above the host's HOMO, additional energy is required for the hole to be created.

Previously, ICT was predominantly observed in doped conjugated polymers, whereas CTC was observed in the analogous conjugated small molecules. For example, doping of polythiophenes with fluorine derivatives of tetracyanoquinodimethane (TCNQ) such as FTCNQ, F_2TCNQ and F_4TCNQ typically occurs via ICT, whereas the same dopants formed CTCs with conjugated small molecules such as quaterthiophene (4T) and oligomers.[58] Moreover, it was believed that for a particular dopant-host system, doping occurs solely via ICT or CTC. Recent reports have disproved both these theories. Although doping of polythiophene with F_4TCNQ typically occurs via ICT, it has been demonstrated that CTCs can be preferentially induced either by processing films at higher temperatures,[85] or by side-chain modification in the polymer.[38] Subsequently, it was also shown that ICT and CTC phases can coexist in F_4TCNQ doped polythiophenes.[39]

These findings indicate the complexities involved in predicting the doping mechanism for a given dopant-host system and consequently, the importance of further research into this topic.

2.2.2 Dopants for Organic Semiconductors

Since the conception of doped organic semiconductors, numerous types of compounds have been studied as prospective dopants. Electronegative compounds with low-lying LUMOs typically make ideal p-dopants. As stated before, early works saw the extensive use of strongly oxidizing gases such as I_2 and Br_2 as p-dopants[19], but the small size and high volatility of these compounds, led to instability in devices. The synthesis of the electron acceptor TCNQ by Melby et al.[86] in 1962 was a significant breakthrough for molecular p-dopants. Fluorine-substituted TCNQs such as F_4TCNQ (EA=5.24 eV), F_6TCNNQ, etc. are some of the most commonly investigated p-dopants today.[25] The highly electronegative fluorine atoms and cyano (C≡N) groups in conjunction with the stabilizing quinone core make this class of molecules very effective as electron acceptors.[86] Nevertheless, some of these small, planar dopant molecules are either still vulnerable to diffusion[87], or have limited solubility in common organic solvents[88]. For example, it has been shown that F_4TCNQ starts diffusing through layers of organic semiconductors such as N,N,N′,N′-tetrakis(4-methoxyphenyl)benzidine (MeO-TPD) or P3HT already at 80°C, and is completely vaporized beyond ca. 120-150°C.[42, 89] This is problematic for its application in organic devices,[88, 90] since it can lead to device failure when processed or operated at higher temperatures. Additionally, it was proposed that the planar structure of these molecules might encourage CTC formation with the host due to dopant-host co-crystallization, which can increase electronic coupling between the frontier orbitals of the two materials.[83] Therefore, more bulky 3D molecules have been developed as alternative p-dopants over the years. The fluorinated fullerene $C_{60}F_{36}$[91] has proved to be a more stable dopant[42] and has been successfully used to dope HTLs in OLED devices[90]. But it is insoluble, and hence cannot be solution processed. In the last decade, the Marder group introduced organometallic complexes such as $Mo(tfd)_3$[50, 92] and its derivatives[93] as promising p-dopants in the field. Of these, Mo(tfd-CO_2Me)$_3$ (EA= 5.0 eV)[51] has been of particular interest due to its high solubility[51], air stability, and performance in organic and perovskite devices[35]. A few years ago, the Bazan group showed that bulky Lewis acids like BCF, which are typically used as a catalyst or co-catalyst in organic/ polymerization reactions[94-95] could also be used to modify the optoelectronic properties of conjugated oligomers and polymers.[43-44] Subsequent work by various groups has shown that p-doping by BCF leads to improved conductivity[49] and hole mobilities in conjugated polymers[45] and small molecule-polymer blends[47], as well as improved performance of organic HTLs in perovskite solar cells[96-97].

Contrary to p-dopants, the development of n-dopants has been quite slow. This is because n-doping requires the dopant materials to have a low IE (HOMO) to be able to undergo charge transfer with the LUMO of the host materials. However, this makes the dopant molecules extremely susceptible to oxidation when exposed to air. Historically, alkali metals such as lithium (Li), potassium (K), cesium (Cs), and their compounds were used as n-dopants,[98-100] but due to dopant diffusion problems, molecular dopants such as bis(ethyleneditho)-tetrathiafulvalene (BETD-TTF),[101] tetrathianaphthacene (TTN),[102] and organometallic compounds like cobaltocene (CoCp2)[103] were developed. In order to address the problem of oxygen sensitivity, Werner et al. introduced oxygen-stable precursor molecules (e.g. pyronine B chloride) as n-dopants.[104] These compounds typically require optical or thermal activation in order to undergo charge transfer with the host material, which allows for a delayed dopant activation either during or after film formation, thereby preventing degradation by oxygen during storage or handling.[104-105] Recently, solution processable dimers of organometallic sandwich compounds like $[RuCp^*(mes)]_2$ have been developed as air-stable precursor n-dopants.[106-107] Upon activation, these dimers cleave to form highly reducing monomers that proceed to dope the organic semiconductor.[108-109]

Stable, doped organic devices are not mainstream in the market despite there being a vast repertoire of materials to choose from, because the dopant-host interactions are influenced by many external factors such as solvents, microstructure, oxygen/humidity, etc. Therefore, it is vital to investigate the role of these external parameters on the doping mechanism and efficiency.

2.2.3 Doping Techniques

Since molecular (or chemical) doping involves the physical mixing of the host and dopant molecules, it follows that there are different techniques for doping a film. In the incipient stages of doping studies, films of small molecule organic semiconductors such as phthalocyanines were simply exposed to vapors of halogens.[20] When a more precise control of the doping level was required, the small molecule host and the dopant were co-evaporated at specific rates to form a uniform doped film. Although vapor deposition techniques such as co-evaporation are suitable and still widely used to fabricate doped films, their application is restricted to small molecule organic semiconductors since polymers cannot be vaporized. Also, the use of volatile dopants in co-evaporation chambers can lead to contamination of the chamber and unintentional doping of subsequent layers.[110] Moreover, this technique is not conducive for large scale, low cost manufacturing processes.

Polymeric semiconductors are typically solution processed, which is a big advantage of this class of materials over small molecule organic semiconductors, many of which are insoluble in organic solvents. Therefore, the easiest way to dope a polymer would be to simply dissolve the polymer and the dopant individually in a suitable solvent and then mix the two according to the required doping ratio to form a *doped solution*. Doped films are subsequently fabricated via spin coating, blade coating, or drop casting.[25] This technique is referred to as *mixed-solution doping,* or *solution blending*. Although this method allows for precise and pre-determined control of the doping level in the solution and film, it has a number of limitations. Firstly, it relies entirely on the solubility of the host and dopant in a particular solvent. Therefore, it not only requires a solvent that is compatible with both materials, but also restricts the application of dopants with low solubility to low concentration solutions, thereby limiting the final thickness of doped films. Secondly, many polymers undergo *doping-induced chain aggregation* upon solution admixture, which typically reduces the polymer chain's solubility in the solvent. This adversely affects the morphology in films. [111-114]

An alternative technique which mitigates these problems is *sequential doping*. Here, the dopant is introduced into a pre-fabricated undoped polymer (or small molecule) film either by vapor deposition, or solution processing using an *orthogonal solvent*, which selectively dissolves only the dopant and not the polymer.[41] As a result, the original morphology (of the undoped state) is preserved in the film even after doping. The main challenge in sequential solution processed layers is dopant density control and film homogeneity. As this technique relies mainly on the diffusion of dopants through the films, the dopant density is not predetermined, as with mixed-solution doping. Instead, the doping level in the film is controlled by parameters such as dopant exposure time and dopant solution concentration, which require optimization. At the same time, it is important to ensure that the dopants are uniformly incorporated into the bulk of the film rather than forming a bilayer. Although small molecule dopants such as F_4TCNQ are shown to form homogeneous sequentially doped films, it is not always the case for bulky dopants.[25] Therefore, subsequent characterization of the films is crucial to monitor the electronic and morphological changes, particularly for sequentially doped films.

2.2.4 Characterization of Doping Processes

As mentioned in section 2.1.3, when charges are introduced into an organic small molecule/polymeric semiconductor, the resulting electronic polarization is accompanied by lattice distortions to enable the molecule to attain its lowest energy state (see Figure 2.6). This relaxation process leads to localization of the electron or hole on a chain segment (which is then referred to as a polaron). In the *classical model* of the energy level schematics, as proposed by Brédas and Street,[115] this is typically depicted as an upward shift of the HOMO (corresponding to the reorganization energy) and a downward shift in the LUMO in the polaron compared to the neutral matrix, as shown in Figure 2.10 for the specific case of a positive polaron. Although this has been the most widely used representation for decades,[115-119] Winkler et al. and Heimel recently proposed a *revised model* of the polaron energetics (see Figure 2.10), based on new experimental and theoretical evidence.[120-121] One major shortcoming of the classical model is that it does not take into consideration the Coulombic interactions between the polaron and the neighboring neutral molecules. However, these inter-site interactions (known as Madelung interactions)[122-123] actually lead to a gradual shift of the LUMO and HOMO of the neutral molecules that are in the proximity of the polaron, as shown in Figure 2.10. Moreover, on-site Coulombic interactions (known as Hubbard interactions)[124-125] in the polaron result in a splitting of the HOMO into two levels (above and below the neutral HOMO level, which are empty and partially filled respectively).

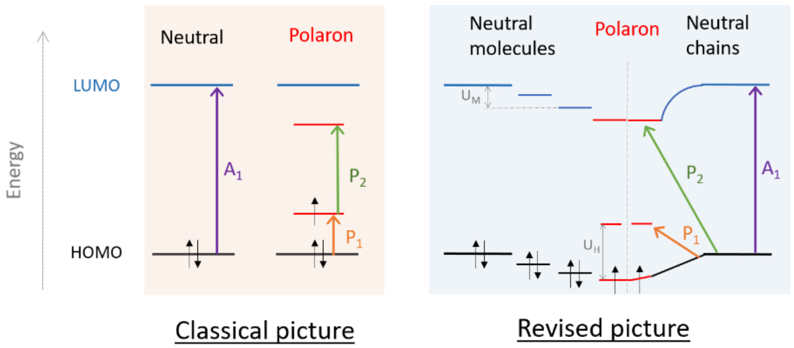

Figure 2.10. Schematic of the optical transitions involved in a neutral and charged organic small molecule/polymeric semiconductor based on the classical representation of (positive) polaron formation proposed by Brédas and Street [115] versus the revised model proposed recently by Winkler et al.[120] and Heimel [121]. The frontier orbitals of neutral organic small molecules/ polymers are shown in blue (LUMO) and black (HOMO); the frontier orbitals of the polaron are shown in red. Unlike the classical picture, the revised model takes into consideration the Coulombic interactions between the charged molecule/subunit and its neutral neighbors, which would lead to additional changes in the corresponding energy levels. [Redrawn after [84]]

A convenient way of studying doping is via UV-Vis-NIR absorption spectroscopy. Since doping involves the formation of new states within the band gap of the host material, optical transitions to/from these sub-band gap states can be used to verify the occurrence of charge transfer in a particular dopant-host system. For example, as shown in Figure 2.10, the optical spectrum of an undoped system (organic/polymeric semiconductor) is mainly characterized by a single optical transition A_1, which corresponds to the optical band gap of the material. In a doped system on the other hand, two additional transitions P_1 and P_2 can take place below the band gap (as shown in Figure 2.10 for a positive polaron), and are visible in the UV-Vis-NIR spectra of the doped solution or films. Moreover, the doping mechanism can also be identified based on the shape and position of the peaks. If the optical spectra of the doped system resemble those of the host cation and/or the dopant anion, it typically indicates ICT, whereas if new sub-band gap features that are not assigned to ionized host/dopant molecules are observed, it may be indicative of CTC. Furthermore, the ionization efficiency of a dopant in a host system can be estimated by qualitative analysis of the optical spectra (using Beer-Lambert Law) of the doped solutions or films, because the P_1 and P_2 transitions typically have large enough oscillator strengths and hence extinction coefficients.

An example of the application of optical spectroscopy for doping studies is shown in Figure 2.11, which was reported in a study by Mendez et al.[58] It depicts the UV-Vis-NIR spectra of films of either P3HT (IE = 4.60 eV)[126] or the oligomer 4T (IE = 5.30 eV)[58] with a series of F_xTCNQ dopants (where x = 0, 1, 2, 4), the latter of which differ in their electron affinities (from 4.23 eV to 5.24 eV)[127].[58] The black lines in Figure 2.11a, b are the absorption spectra of the neutral host molecules (P3HT or 4T), which show no discernible features below their band gap. When blended with dopants, characteristic new absorption bands are observed. In the case of F_xTCNQ-doped P3HT films shown in Figure 2.11a, c , the new sub-band gap peaks are consistently at the same position, and the spectral shape closely matches that of the F_4TCNQ anion and the P3HT polaron.[58] This implies that in these blends, ICT occurs between the P3HT and F_xTCNQ molecules. On the other hand, the sub-band gap absorption by the F_xTCNQ-doped 4T films (see Figure 2.11b, d) takes place at different energy values that do not correspond to that of the dopant anion or the host polaron, indicating the absence of these species in the blend. Moreover, the position of sub-band gap absorption peaks of the F_xTCNQ-doped 4T films shift depending on the electron affinity of the dopant (Figure 2.11d), suggesting that the energy level of the absorbing species changes with each dopant.[58] This is a characteristic indication of the formation of CTCs between the dopant and 4T molecules.

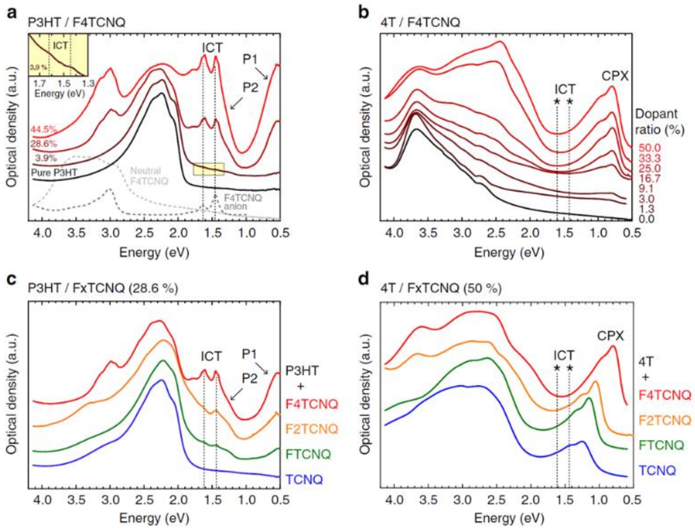

Figure 2.11. UV-Vis-NIR spectra of (a) P3HT blended with F_4TCNQ at increasing ratio with the inset showing the zoomed region around the ICT features in the film of 3.9% dopant ratio (one F_4TCNQ per 25 quaterthiophene segments), (b) 4T blended with F_4TCNQ at increasing ratio, (c) P3HT blended with the full range of differently strong dopants (TCNQ to F_4TCNQ) at a dopant ratio of 28.6% and (d) of 4T blends with the full range of differently strong dopants (TCNQ to F_4TCNQ) in 1:1 ratio (50%); P_1 and P_2 indicate the optical transitions of the positive polaron in P3HT [115, 118-119, 128]; asterisks indicate the expected transition energies related to dopant anions (ICT) that are absent in the 4T case. (Figure and caption reproduced from Méndez et al.[58] Copyright (2015), Springer Nature)

Doping and the degree of charge transfer in a particular host-dopant system can also be studied by infrared (IR) spectroscopy. The vibrational modes of an organic semiconductor are strongly coupled to its electronic and geometric structure. Since doping induces local distortions in the molecule, new infrared-active vibrational (IRAV) modes with high intensities are observed in the doped system.[110, 129] Therefore, doping-induced vibrational changes on either the host molecule [118, 130] or the dopant molecules[58, 131] can be monitored by studying different regions of the IR spectrum.

A powerful but under-utilized technique for studying doping is EPR spectroscopy. In their ground state, systems that undergo ICT to form polarons are paramagnetic and hence EPR sensitive, whereas those which predominantly form *bipolarons*[b] and CTCs are EPR silent due to their diamagnetic nature. Therefore this technique is particularly useful for studying the mechanism of doping in situations where optical spectroscopy might not yield reliable results, such as when the system is light sensitive (as discussed in Chapter-5). Moreover, quantitative evaluation of the doped solutions or films can be made by calibrating the samples to a standard reference. For example, the density of mobile/bound unpaired electron spins estimated using EPR spectroscopy provides insights about the density of charge carriers in the sample.[49, 132]

Upon doping, the electronic structure of the host material undergoes changes. While the Fermi level (E_F) lies mid-gap in an undoped semiconductor, it moves closer to the HOMO (p-doping) or LUMO (n-doping) when the material is doped. When doped films are used in conjunction with metals or other organic layers, Fermi level alignment takes place, resulting in the movement of charges at the interface of the different layers. These changes in the electronic structure can be probed using photoelectron spectroscopy (PES) techniques[133] such as ultraviolet photoelectron spectroscopy (UPS),[134] X-ray photoelectron spectroscopy (XPS) and inverse photoelectron spectroscopy (IPES).

Morphological changes in doped films are most often studied on a macroscopic level using AFM. Doping-induced chain aggregation is typically visible in AFM images of mixed solution doped films, and is generally accompanied by an increase in film roughness.[40, 135-136]Additionally, Duong et al. have shown using conductive-AFM (c-AFM) studies that these aggregates formed at higher doping ratios are conductive in nature, and that the size of the aggregates can be controlled by dopant concentration in the film, or the solution temperature during film casting.[136] For (semi)crystalline materials, X-ray diffraction/scattering techniques are widely used to study the changes in the film microstructure, as well as identify the location of the dopant counter-ion in the film.[58, 111, 114]

There are different techniques to evaluate the electrical properties of doped layers. The conductivity of doped films (in the ohmic regime) can be quite easily estimated by measuring the *current-voltage* (IV) *characteristics* using a 2-point probe (2PP) or 4-point probe (4PP) architecture.[40, 137] The trend in the evolution of a sample's conductivity with dopant loading reveals important underlying

---

[b] If a charged polymer chain (i.e. polaron) undergoes further oxidation/reduction such that the two charges (polarons) are coupled, it leads to a localized distortion on the chain. This quasiparticle is known as a *bipolaron*.

processes. For example, a *superlinear* increase in conductivity (with increasing doping ratio) typically implies an improvement in the mobility of the charge carriers.[138] On the other hand, a *sublinear* increase in the conductivity value, which has been reported in some systems for low to moderate doping ratios,[139] implies a decreasing mobility in this regime.[36] The direct estimation of the mobility (μ) of charge carriers in doped films is tricky since this parameter is sensitive to changes in the morphology of the layers as well as the carrier concentration (n) in the film, which can hinder an accurate estimation. The mobility of charge carries in films with ultralow doping levels (which serve to fill traps) can be estimated with the OFET architecture.[140] For more strongly doped layers, depending on the doping level, either the *JV* characteristics of hole-only/ electron-only devices operated in the *space-charge limited current* (SCLC) regime,[141-142] or the AC Hall effect [41, 143] is used to determine the mobility.

3. Methods and Materials

In this chapter, the setup and the basic physics behind the different experimental techniques applied in this work is explained. Subsequently, the different dopant and host materials used in this work are introduced, and the general procedure of sample preparation (solutions and films) is described.

3.1 Experimental Methods

3.1.1 Optical Spectroscopy

The interaction of matter with light is probed using optical spectroscopy. When light is incident on a sample in its electronic ground state, electrons in the ground state (HOMO) can be excited to higher states, provided the incident beam has sufficient energy.

UV-Vis-NIR spectroscopy: As the name suggests, UV-Vis-NIR absorption spectroscopy utilizes incident light in the ultraviolet (ca. 200nm - 400 nm), visible (ca. 400 nm - 750nm) and near-infrared (NIR, ca. 750 nm – 3000 nm) regions to probe the optical transitions in a material. Since this energy range (~ 0.4 eV - 6 eV) predominantly excites electrons from π- or *non-bonding* orbitals to π^* orbitals, this technique is particularly suitable for studying conjugated organic molecules and polymers, which contain π-bonds.

In an absorption spectrometer, a monochromatic light beam (produced using a diffraction grating) of intensity I_0 is allowed to pass through a sample, and the transmitted beam (with intensity I) is collected and analyzed by a detector (see Figure 3.1). Thus, the *absorbance* A, which is a measure of attenuation of the incident light, is given by the relation

$$A = -\log_{10}\left(\frac{I}{I_0}\right) \tag{3.1}$$

Absorption spectroscopy can also be used for the quantitative analysis of a sample, as per the *Beer-Lambert law*, which states that the absorbance is directly proportional to the concentration c of the absorbing species, as well as the path length l of the light beam through the absorbing medium. This is given by the equation

$$A = \varepsilon c l \tag{3.2}$$

where ε is the *molar extinction coefficient*, which is a measure of how strongly a material absorbs light at a particular wavelength.

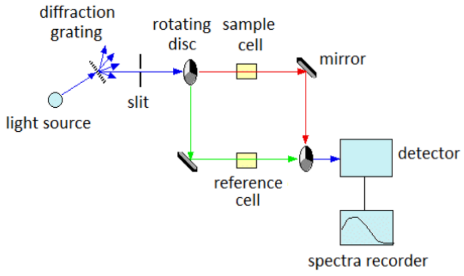

Figure 3.1. Schematic of the instrumental setup of a typical double-beam absorption spectrometer [Reproduced from [144]].

UV-Vis-NIR absorption measurements in this work were carried out on a *Varian Cary 5000* spectrophotometer. The solutions were typically transferred into 1 mm path length precision quartz cuvettes inside the glovebox, and subsequently measured outside the glovebox. The background due to solvent contribution was subtracted from the final results. The recorded spectra were analyzed using OriginPro®. Additional information about the quantitative analysis is given in Chapter-5.

For the temperature dependence studies, the instrument was fitted with a temperature controlled cuvette holder TCL 50, by *Quantum Northwest*. The solutions were maintained at each temperature for 10 minutes for equilibration and then measured. Each measurement lasted ca. 7 minutes, so the total time at each temperature was ca. 17 minutes.

Equations 3.1 and 3.2 are mostly based on the assumption that light attenuation is solely due to absorption and not due to effects such as scattering, interference etc. Although this holds true for solutions with low enough concentrations, the intensity of light transmitted through films may be affected by these processes, particularly when a layer is rough. Therefore, an *integrating sphere* accessory is often used along with the setup, to get a true value of the optical density (absorbance) of the layer. The integrating sphere measures both the *specular reflection* (symmetrical reflection such as from a smooth, mirror-like surface) as well as *diffuse reflection* (occurring in multiple directions) from a sample, as depicted in Figure 3.2. The Lambertian coating (PTFE) in the sphere ensures that the light beam undergoes multiple diffuse reflections inside the sphere, whereby the final radiance measured at the detector is independent of the scattering/ reflectance directions.

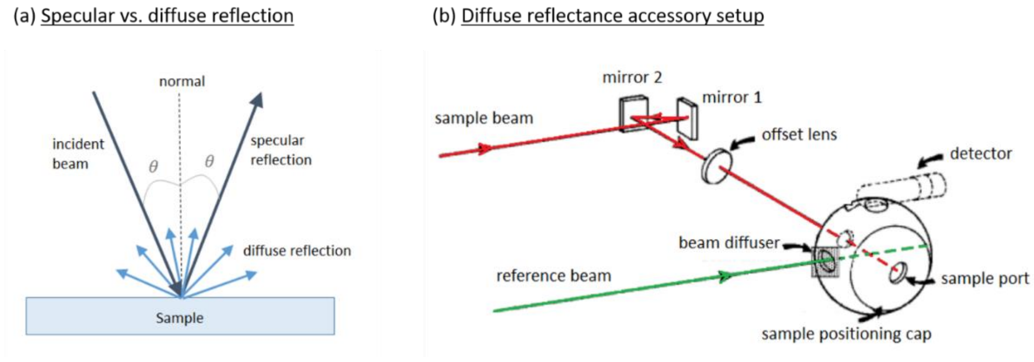

Figure 3.2. (a) Specular and diffuse components of reflection occurring from an opaque sample. (b) Schematics of a diffuse reflectance accessory with which both specular reflection and diffuse reflection from a sample can be measured [Reproduced from [145]].

The UV-Vis-NIR absorption of films was measured in air using the Varian Cary 5000 spectrophotometer with the *diffuse reflectance accessory* (an integrating sphere), in the *reflectance* (specular + diffuse) and *transmittance* mode. The optical density (absorbance) of the film was calculated according to the equation

$$OD = \log\left(\frac{100 - \%R}{\%T}\right) \tag{3.3}$$

where $\%R$ and $\%T$ are the percentage reflectance and transmittance spectra respectively. The optical density of the glass was then subtracted from that of the film (organic layer + glass) to obtain the absorbance spectrum of the layer.

<u>Photoluminescence Spectroscopy</u>: When a material absorbs *photons* and gets excited to higher energy states, the excess energy is subsequently released (either in the form of photons, or non-radiatively), as the material relaxes to its ground state. The phenomenon of light emission from a

photo-excited substance is known as *photoluminescence* (PL). The PL emission spectrum of a sample is obtained by exciting the sample with a single wavelength, and measuring the intensity of the emitted radiation as a function of wavelength.

The photoluminescence intensity of the undoped and dip-doped films on glass was measured in a *Horiba Jobin Yvon Fluorolog 3* fluorescence spectrometer, in ambient air. The samples were excited at 580 nm, and the corresponding emission was measured in the range of 610 nm – 800 nm.

3.1.2 EPR Spectroscopy

Electron Paramagnetic Resonance (EPR) uses the *Zeeman effect* to detect the presence of unpaired electrons in a system. Every electron possesses an intrinsic angular momentum (orbital + spin) in addition to its elementary charge. The *spin angular momentum* is associated with the "spin" of the electron along its own axis, and can assume two states – *parallel* or *antiparallel* to the reference. In the absence of an external magnetic field, these two states are energetically degenerate. However, in the presence of a magnetic field, the two states are split into a higher energy state (antiparallel to the magnetic field) and lower energy state (parallel to the magnetic field), and the phenomenon is known as the *Zeeman effect*. In EPR spectroscopy, a transition is induced between the two spin states by irradiating the paramagnetic sample with microwaves. The transition energy (ΔE) between the two spin states, which is also known as the Zeeman splitting energy is given by

$$\Delta E = g\mu_B B = hv \tag{3.4}$$

where g is the Landé factor (or g-factor) , μ_B is the Bohr Magneton (constant), B is the strength of the applied magnetic field, h is Planck's constant and v is the resonance frequency of the microwave radiation.

Since the splitting energy is linearly proportional to the magnetic field strength, a common way of measuring the EPR spectrum of a sample is by keeping the frequency of the electromagnetic wave constant, and scanning through the magnetic field. Thus, when the splitting energy at a specific magnetic field matches the irradiation energy, the spin of the unpaired electrons in the sample is flipped, with the absorption of the photons as shown in Figure 3.3. The strength of the absorption signal can then be used to quantify the number of unpaired electrons. Additionally, since the g-factor is characteristic of a particular paramagnetic species and its local environment, the nature of the species can also be investigated with this measurement technique.

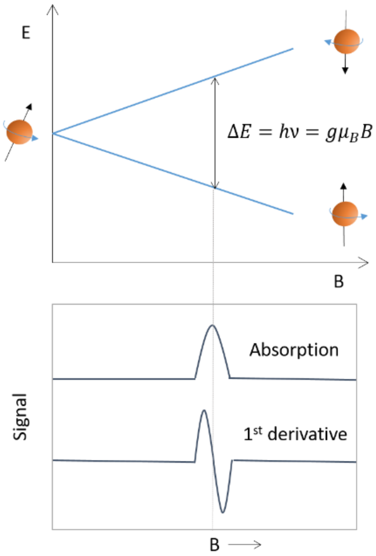

Figure 3.3. Schematic illustration of Zeeman splitting of the energy levels of an unpaired electron under an applied magnetic field. An EPR signal is generated by tuning the microwave frequency (ν) of the incident beam and the strength of the magnetic field (B) to achieve the resonance condition and induce a spin-flip with the absorption of microwaves. Typically, the first derivative of the absorption curve is acquired and reported.

EPR measurements and analysis were done by Dr. Claudia E. Tait (Berlin Joint EPR Lab, *Freie Universität Berlin*). Room temperature X-band continuous-wave EPR measurements were performed on a Magnettech MS5000 spectrometer with a liquid-nitrogen-based temperature-control unit. 25 µl of the doped/undoped solutions were transferred into a 2.9 mm OD, 2.0 mm ID quartz EPR tube inside a glovebox, and the tube was then sealed with Critoseal^{TM}. The measurements were performed at a microwave power of 63 µW, with a modulation frequency of 100 kHz and modulation amplitudes in the range from 0.005 mT to 0.05 mT, depending on the sample. The number of spins (i.e. spin concentration) was determined from the comparison of the double integral of the experimental spectrum with that of a reference sample of known spin concentration (TEMPOL, stable nitroxide radical, in toluene), taking the experimental settings and the Q-factor of the resonator into account. Further details about the measurement procedure and data evaluation are provided in our corresponding joint publication[146].

3.1.3 Atomic Force Microscopy

The topological mapping of the doped and undoped films was done using an atomic force microscope, in tapping mode. Figure 3.4 shows the basic setup of an AFM. It consists of a flexible oscillating cantilever with a microscopic tip at one end, which scans across the surface of the sample and records the height profile at a nanometer scale. The interactive forces (e.g. van der Waals) between the tip and the sample lead to deflections of the tip (and changes in oscillation amplitude), which is detected by the change in the position of the laser beam on the photo detector. A feedback loop between the photo detector and the cantilever notes the change in the oscillation amplitude, and accordingly shifts the cantilever up or down such that the initial amplitude is maintained, thus mapping the topography of the sample.

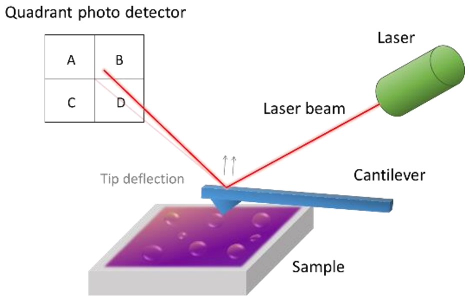

Figure 3.4. Illustration of the main components and the working principle of an atomic force microscope.

The AFM images presented in this work were recorded using a Solver SPM, NT-MDT atomic force microscopy setup, operated in tapping mode. The films were spin/dip-coated from solutions onto clean glass substrates inside the glovebox, and measured in ambient air.

3.1.4 Grazing Incidence X-ray Diffraction

If a material is crystalline enough, the packing behavior (i.e. the spacing between the repeating entities) within the crystallites can be studied by X-ray diffraction on thin film or powder samples. This is based on *Bragg's law* which states that when X-ray beams of a monochromatic wavelength

λ are impinged on a sample with atoms (or molecules) arranged in a regular pattern (with an interplanar distance d), strong reflected X-ray beams are detected at specific angles (θ) due to the *constructive interference* of the reflected beams. Importantly, this constructive interference occurs only if the product of the interplanar spacing (d) and the angle of incidence is an integer multiple (n) of the incident wavelength λ as per the Bragg equation:

$$n\lambda = 2d\ sin\theta \qquad (3.5)$$

Since rreP3HT is a semiconducting polymer that is known to self-assemble, this principle can be used to study the packing motif within the crystallites. Typically, a *grazing incident angle* is used to probe thin polymer film samples in order to 1) reduce the X-ray penetration depth (and thereby reduce the X-ray absorption/reflection from the Si substrate) and 2) reduce the beam-induced damage of the sample (by reducing the X-ray flux on a sample area). Figure 3.5 shows the schematic of a GIXRD setup for thin film characterization.

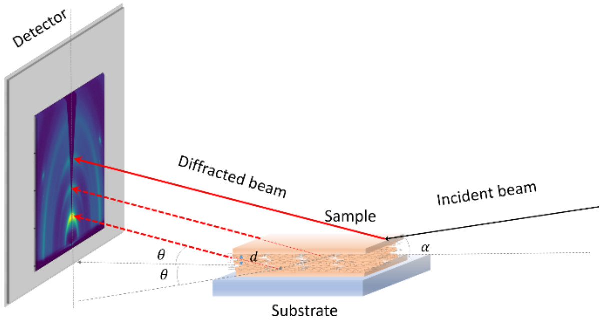

Figure 3.5. Schematic illustration of grazing incidence X-ray diffraction from a rreP3HT film, showing out-of-plane scattering from the lamellar stacks within the crystallites (not to scale).

The GIXRD measurements presented in this thesis were carried out by Dr. Ingo Salzmann at the synchrotron radiation source BESSY II of the Helmholtz-Zentrum Berlin for Materials and Energy (HZB), using the KMC-2 beamline equipped with a Vantec 2000 area detector. The primary beam wavelength was 1 Å and the angle of incidence was set to 0.2°.

3.1.5 Conductivity

The electrical conductivity of a material can be easily estimated by applying a potential difference across two points on the sample and measuring the current flow between them. This is the basic principle of current-voltage ($I - V$) measurements of a sample. From Ohm's law, the conductivity (σ) of the film can be estimated as follows:

$$\sigma = \frac{l}{A}\left(\frac{I}{V}\right) \tag{3.6}$$

where l is the film thickness, A is the cross-sectional area, V is the potential drop, and I is the current flow. One disadvantage of this basic approach is that the contact resistance between the measurement probe and the sample is also included in the total resistivity (and conductivity) measured. Therefore, the alternative 4-point probe method is commonly used to accurately determine the sheet resistance (R_s) and conductivity of doped films. The setup consists of 4 equally spaced probes that linearly contact the film as shown in Figure 3.6. A known current is passed between the outer probes, and the voltage drop between the inner probes is measured. Due to the fixed geometry, the sheet resistance (R_s) and conductivity (σ) of the material without contact resistance effects, can be estimated as per equation 3.7.

$$\begin{gathered} R_S = \frac{\pi}{\ln 2}\left(\frac{V}{I}\right) \\ \sigma = \frac{1}{lR_s} \end{gathered} \tag{3.7}$$

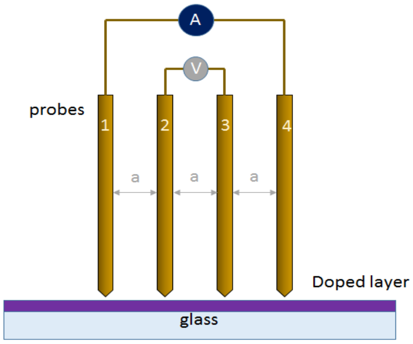

Figure 3.6. Sketch of a 4 point-probe setup used for measuring the conductivity of a film

Conductivity results shown in this work were performed in inert atmosphere using a home-built 4PP setup. The gold-coated probes purchased from INGUN were arranged with a fixed equal spacing (a) of ca. 1 mm between each other. An *Agilent Semiconductor Parameter Analyzer* was used to supply the current and measure the voltage between the probes. Doped films were prepared on clean glass substrates in the glovebox, and measured at different points on the sample to get a reliable value. The film thickness was measured using a surface profilometer (Dektak). A MatLAB script was used to calculate the sheet resistance and conductivity as per equation 3.7. The reported conductivity values are an average of 6-8 measurements on the sample.

3.2 Materials and Sample Preparation

3.2.1 Materials:

The majority of the work presented in this thesis was done using the prototypical polymer P3HT as the host material. Regioregular P3HT (rreP3HT) with > 96 % regioregularity and molecular weight (M_w) of ca. 36 kDa was purchased from Rieke Metals. Regiorandom P3HT (rraP3HT) with M_w of ca. 37 kDa and ca. 50% probability of head-to-tail couplings was obtained from Sigma Aldrich. The p-type dopants 2,3,5,6-tetrafluoro-7,7,8,8-tetracyanoquinodimethane (F_4TCNQ) and trispentafluorophenylborane (BCF), and the protic acid Bis(trifluoromethanesulfonyl)imide (HTFSI) were purchased from TCI Europe and used as received, without further purification. The p-type dopant molybdenum tris[1-(methoxycarbonyl)-2-(trifluoromethyl)-ethane-1,2-dithiolene]

($Mo(tfd-CO_2Me)_3$) was synthesized by Yadong Zhang[c] according to the procedure described in the reference[51]. The chemical structures of these polymers and dopants are shown in Figure 3.7.

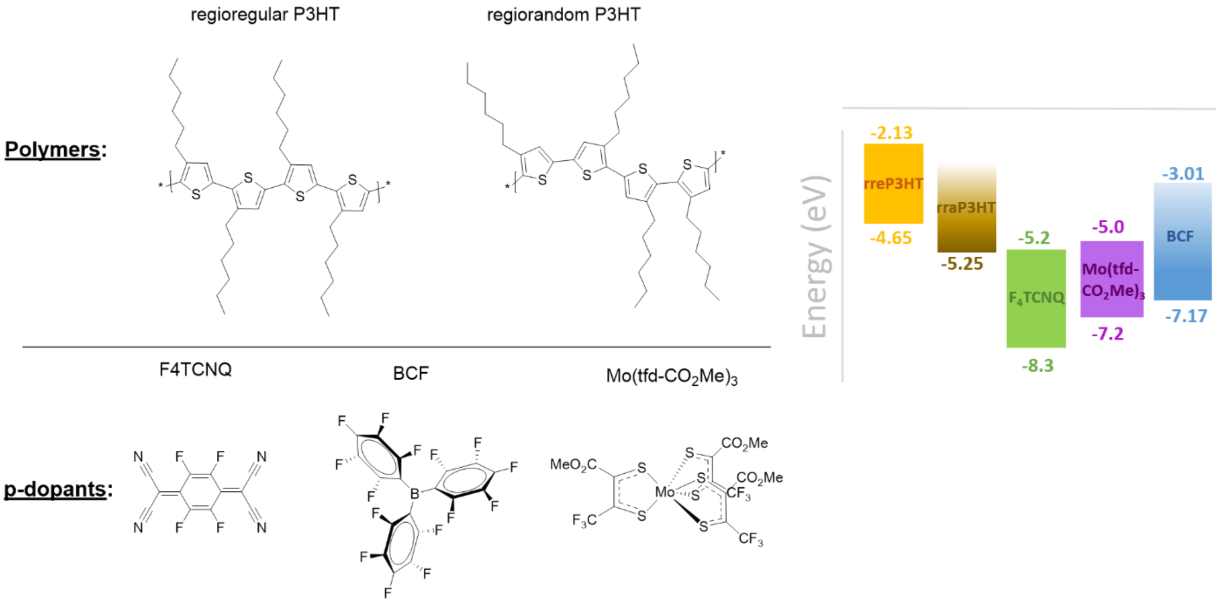

Figure 3.7. <u>Left</u>: Chemical structures of the main polymers and p-dopants used in this work. <u>Right</u>: HOMO (assumed as negative of ionization potential) and LUMO (assumed as negative of EA) energy values of the different materials in the solid state estimated by UPS and IPES (except for the BCF EA, which corresponds to solution data from cyclic voltammetry[147]), taken from the literature.[47, 51, 87, 147-149]

<u>3.2.2 General Sample Preparation:</u>

All the polymers and dopants were typically stored and handled in an inert N_2 atmosphere glovebox with oxygen and H_2O levels typically below 0.5 ppm, but were exposed to air for a short time at the time of weighing the required amounts into smaller vials (for subsequent solution preparation, except for HTFSI which was handled exclusively inside the glovebox).

The solutions used for the experiments in Chapter-4 were prepared as follows: The polymer (rreP3HT) and the dopant (F_4TCNQ or BCF) were dissolved separately in spectroscopic grade chloroform (99.9 % purity, purchased from Carl Roth) or chlorobenzene (99.9 % purity, purchased from Sigma Aldrich), in inert N_2 atmosphere. The undoped rreP3HT and F_4TCNQ solutions were

---

[c] Yadong Zhang is a member of Prof. Seth Marder's group, based in the School of Chemistry and Biochemistry and Center for Organic Photonics and Electronics at the Georgia Institute of Technology, USA

typically heated to 55-60°C for a few minutes and/or shaken with a mechanical shaker until a homogeneous solution was obtained. BCF, on the other hand, dissolved easily in these solvents and hence did not require heating. The typical concentrations of the stock solutions were 2 mg mL^{-1} for the undoped rreP3HT solution, 0.5 mg mL^{-1} for the F_4TCNQ solution and 2 mg mL^{-1} for the BCF solution. Following this, specific volumes of the dopant and polymer solutions (to obtain the required molar ratio of dopant molecules:3HT repeat units) were added either into a fresh empty vial or a quartz cuvette (for the UV-Vis-NIR experiments) to obtain the final mixture, i.e. the doped P3HT solution. For the *in-situ* absorption experiments shown in Figures 4.2 and 4.4, this step was done in *air* by directly adding the specific amount of the dopant solution (or the non-solvent ethyl acetate) into a 1 mm quartz cuvette containing the polymer solution, manually shaking it and immediately starting the UV-Vis-NIR measurement. Due to inconsistency in some of the BCF-doped rreP3HT results and additional experience gained from having handled this system[d], we took care to ensure consistent *light exposure* during and after the preparation of the BCF-doped rreP3HT solution for all subsequent experiments (this is discussed in detail in Chapter-4). Moreover, for all the subsequent UV-Vis-NIR experiments, the doped and undoped solutions were transferred into the cuvettes inside the glovebox to further minimize air exposure.

Note that we purposefully ensured that the doped P3HT solutions were prepared and handled only at room temperature (unless stated otherwise), in order to study the doping level and the aggregation behavior, both of which are influenced by temperature, [119, 136] under comparable conditions. This is discussed in greater detail in Chapter-5.

The solutions used for the experiments in Chapter-5 were prepared as follows: The polymer (rreP3HT or rraP3HT) and dopant were dissolved separately in chloroform and mixed according to the required doping ratios in inert N_2 atmosphere. The BCF and Mo(tfd-CO_2Me$)_3$ doped solutions were stirred slowly for about 24 h (doped rreP3HT), and 4 h (doped rraP3HT) in the glove box (with the light on) before being measured. The F_4TCNQ doped rreP3HT and rraP3HT solutions were measured soon after preparation since the formed species were found to change upon long duration of stirring. The final P3HT concentration in the solutions was typically 2 mg mL^{-1} (1.25

---

[d] Based on the collective experience from my UV-Vis-NIR experiments at the University of Potsdam, and the EPR experiments performed by our collaborators Dr. Robert Steyrleuthner and Kelvin Yao who were part of the Behrends group and the Berlin Joint EPR Lab in the Freie Universität Berlin at that time.

mg mL^{-1} in 1:10 F_4TCNQ – rraP3HT, due to the poor solubility of F_4TCNQ) unless mentioned otherwise. This fairly high final concentration ensured that the absorbance (and EPR signal) of the doping-induced species was above the noise level while, at the same time, allowing for a fairly small dopant to polymer ratio (eg. 1:100), the latter of which is important to avoid spin-spin interactions along the same polymer chain. The Mo(tfd-CO_2Me)$_3$ anion (for UV-Vis-NIR measurements) was generated by adding a few µL of de-ionized water to neutral Mo(tfd-CO_2Me)$_3$ solution (300 µL) in anhydrous tetrahydrofuran.

The solutions for temperature-dependent measurements were prepared in chlorobenzene instead of chloroform due to chlorobenzene's higher boiling point.

For the doped films discussed in Chapter-6, three different fabrication techniques have been used: mixed-solution doping, sequential spin-coating or dip-doping. Figures 3.8 and 3.9 schematically illustrate these methods. In the traditional *mixed-solution doping* technique, as described above for solutions studied in Chapter-4, the dopant and polymer were first dissolved separately in chloroform. The typical concentrations were 20 mg mL^{-1} for the undoped rreP3HT solution, 0.5 mg mL^{-1} for the F_4TCNQ solution and 5 mg mL^{-1} for the BCF solution. Next, specific volumes of the dopant and polymer solution were mixed to obtain the doped polymer solution with the required molar ratio of dopant:3HT. Doped films were then prepared by spin-casting the doped P3HT solution onto rotating glass, or Si substrates (depending on the application) at a spin speed of 1500 rpm (or 500-600 rpm for thick films) for 50 seconds. Prior to spin-coating, the substrates were washed with a series of solvents (acetone, Hellmanex®, de-ionized H_2O and isopropanol) in an ultrasonic bath, dried with a jet of N_2 and then plasma cleaned to remove any traces of organic matter or solvents. Note that although the kinetics of charge transfer (doping) between BCF and rreP3HT were typically slow and influenced by light exposure in the solution-state (as discussed in Chapter-4), we found that the polaron level in the *solid-state* was unaffected by either of the parameters. Therefore the films were typically spun within 1 h after solution preparation.

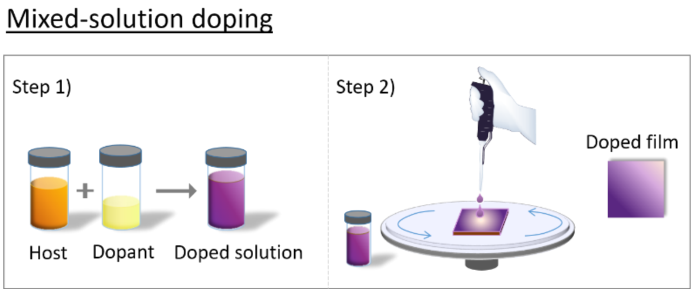

Figure 3.8. Schematic illustration of the fabrication process of mixed-solution doped films.

For the *sequentially* doped samples, the first step involved the fabrication of the undoped polymer film, so the rreP3HT solution (10-20 mg mL^{-1} in chloroform unless stated otherwise) was spin-coated at ca. 1500 rpm, 50 seconds onto cleaned, rotating substrates. In the second step, the dopant was introduced into these films through an orthogonal solvent (dichloromethane (DCM)) either by spin-coating (which we refer to as *sequential spin-coating*) or by dipping (which we refer to as *dip-doping*), as depicted in Figure 3.9. In sequential spin-coating, about 200 µL of the dopant:DCM solution (with a typical concentration of 0.125-0.5 mg mL^{-1} for F_4TCNQ and 1.25-5 mg mL^{-1} for BCF) was spread onto the undoped rreP3HT film and after waiting for ca. 30 seconds, the film was spun at 1500 rpm for 50 seconds, thereby rendering the film doped. Dip-doped films were fabricated by dipping the undoped rreP3HT films into a beaker containing dopant:DCM solution for the specified duration of time (ranging from 1 minute to 24 hours), and finally giving it a quick dip in pure DCM (contained in a different beaker) to remove any stray dopant particles adhering to the film. As a control, the undoped rreP3HT film was also typically dipped in DCM to check for any solvent-induced changes.

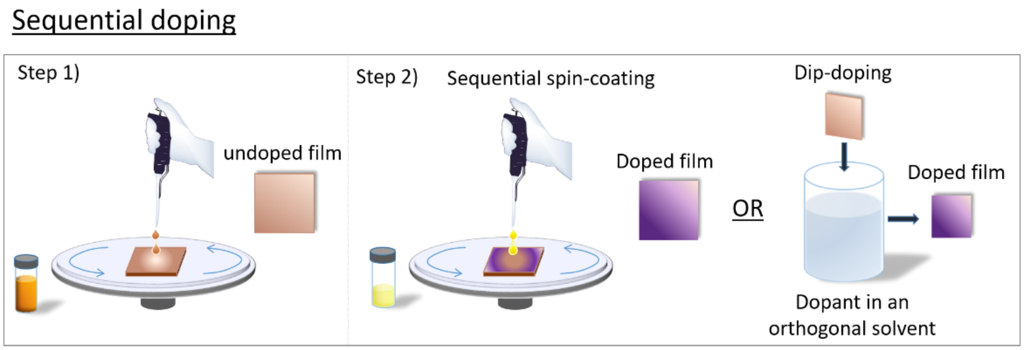

Figure 3.9. Schematic illustration of the sequential doping process, which either involves sequential spin-coating or dip-doping.

Unless mentioned otherwise, the films typically have a thickness of 45 – 180 nm, measured using a *Veeco Dektak 3T* surface profilometer.

4. Preliminary Investigation: Factors Influencing Polaron Formation in BCF Doped P3HT Solution

At the beginning of this work, although other groups had previously employed the Lewis acid BCF as a p-dopant for organic semiconductors, [44-45] the actual mechanism of doping was largely unknown. As mentioned earlier, I investigated the doping mechanism in BCF doped rreP3HT solutions and films as a part of my master thesis[48], and found that despite the dissimilarities of BCF and the traditional electron acceptor F_4TCNQ, both dopants resulted in ICT with the polymer.[49] However, the BCF doped solutions exhibited low ionization efficiencies and slow charge transfer equilibration.[49] As a result, the preliminary studies of this project were motivated by the aim of understanding the kinetics of polaron formation in BCF doped solutions, and what factors influence the doping level in this system. This was of particular importance, since we often faced problems with inconsistency and irreproducibility of the final doping (ionization) level in BCF doped P3HT solutions. Therefore the insights from this chapter were crucial for the preparation of consistent samples, which were then used for the work in Chapter-5.

4.1 Introduction

As stated in the previous chapters, doping of a conjugated polymer leads to the creation of sub-band gap levels, the presence of which can be verified using UV-Vis-NIR spectroscopy. Figure 4.1 shows the UV-Vis-NIR spectra of undoped rreP3HT, F_4TCNQ- and BCF-doped rreP3HT with a molar ratio of 1:100 (1 molecule of dopant per 100 hexylthiophene units) measured in chloroform solutions, and the scaled extinction coefficient spectra of the F_4TCNQ anion[150] and P3HT polaron[48-49] taken from the literature. The undoped rreP3HT solution has an absorption onset at ca. 2.0 eV, with a maximum around 2.5 eV which corresponds to the optical band-gap of rreP3HT (note that the strong absorption maximum is cut-off in this range due to the detector's limitations). Upon doping rreP3HT with F_4TCNQ, new features emerge in the near-infrared (NIR) region, indicating the occurrence of charge transfer in the system. The low energy feature below 1 eV and the broad absorption shoulder in the range 1.25 eV – 1.75 eV are collectively attributed to the dopant-induced positive polaron on the P3HT backbone, and correspond to the P_1 and P_2 transitions (see Figure 2.11), respectively.[118] The spectrum also exhibits the characteristic twin peaks at 1.4

eV and 1.6 eV which are assigned to the F_4TCNQ radical anion. [36, 150] Additionally, the spectrum shows new resolved peaks at 2.01 eV and 2.18 eV, which correspond to the π-π* absorption of aggregated neutral P3HT chains.[52]

Similar doping-induced sub band-gap signals are formed upon mixing BCF with rreP3HT. The spectrum shows a clear contribution from the P3HT polaron (absorption below 1 eV and a broad peak between 1.25 to 1.75 eV), and the neutral P3HT aggregates (ca. 2 eV), but no additional NIR signal from the BCF anion. According to literature, the BCF radical anion absorption is expected to occur at about 2.05 eV.[147, 151] The absence of this signal in our spectrum implies that it is either so weak that it cannot be distinguished from the overlapping neutral P3HT aggregate absorption, or that the BCF is not present in radical anion form due to chemical transformation during or after the doping process. (In subsequent sections, based on additional experiments and new literature we will show that the latter situation is more likely.) Nevertheless, the presence of the P3HT polaron (and F_4TCNQ anion in the F_4TCNQ-doped solution) signature indicates that charge transfer occurs predominantly via the ICT mechanism in the two systems. A detailed analysis of the optical signatures, the doping level (ionization efficiency) and nature of the species formed in these solutions is presented in Chapter-5.

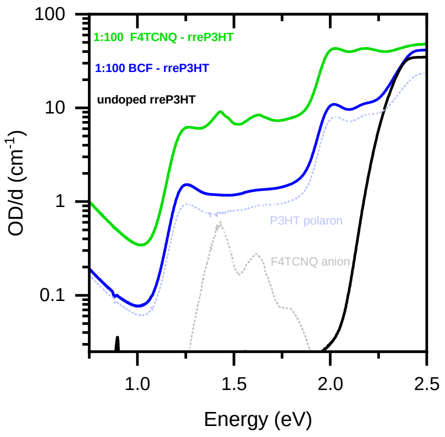

Figure 4.1. UV-Vis-NIR spectra of undoped rreP3HT, 1:100 ratio F_4TCNQ-doped rreP3HT and BCF-doped rreP3HT solution (in chloroform). The ratio 1:100 corresponds to 1 dopant molecule per 100 repeat units of 3HT. The dotted lines correspond to the scaled extinction coefficient spectra ($\varepsilon \times 1.2 \times 10^5$) of the F_4TCNQ radical anion and the P3HT radical polaron taken from the literature[49, 150].

A recurring observation during the preparation of BCF doped solutions was that the charge transfer process was quite slow compared to that in F_4TCNQ doped P3HT. Figure 4.2 shows the UV-Vis-NIR spectra of 1:10 ratio F_4TCNQ- and BCF-doped rreP3HT solutions in CF, measured soon after doping (mixing) and at specific time intervals over the next few hours. Both UV-Vis-NIR spectra show ICT features. Due to the high doping ratio, the shoulder at 1.25 eV corresponding to the P_2 transition of the P3HT polaron in the F_4TCNQ-doped solution is presumably buried under the strong F_4TCNQ anion absorption. Importantly, in this system, strong doping-induced signals are observed immediately upon doping, and remain stable with time (see Figure 4.2b). In BCF doped rreP3HT on the other hand, the P3HT polaron signal increases sublinearly by one order of magnitude from the time of preparation (first measurement) to after ca. 20 h, beyond which it remains stable. Notably, the increase is strongest in the first few minutes and hours, and saturates after 20 h. Moreover, we see that with BCF doping, the increase in the P3HT polaron signal with time, is accompanied by an increase in the aggregation signal at 2.0 eV. Therefore, our first idea was to check if pre-aggregation of the P3HT chains can improve the kinetics of BCF doping.

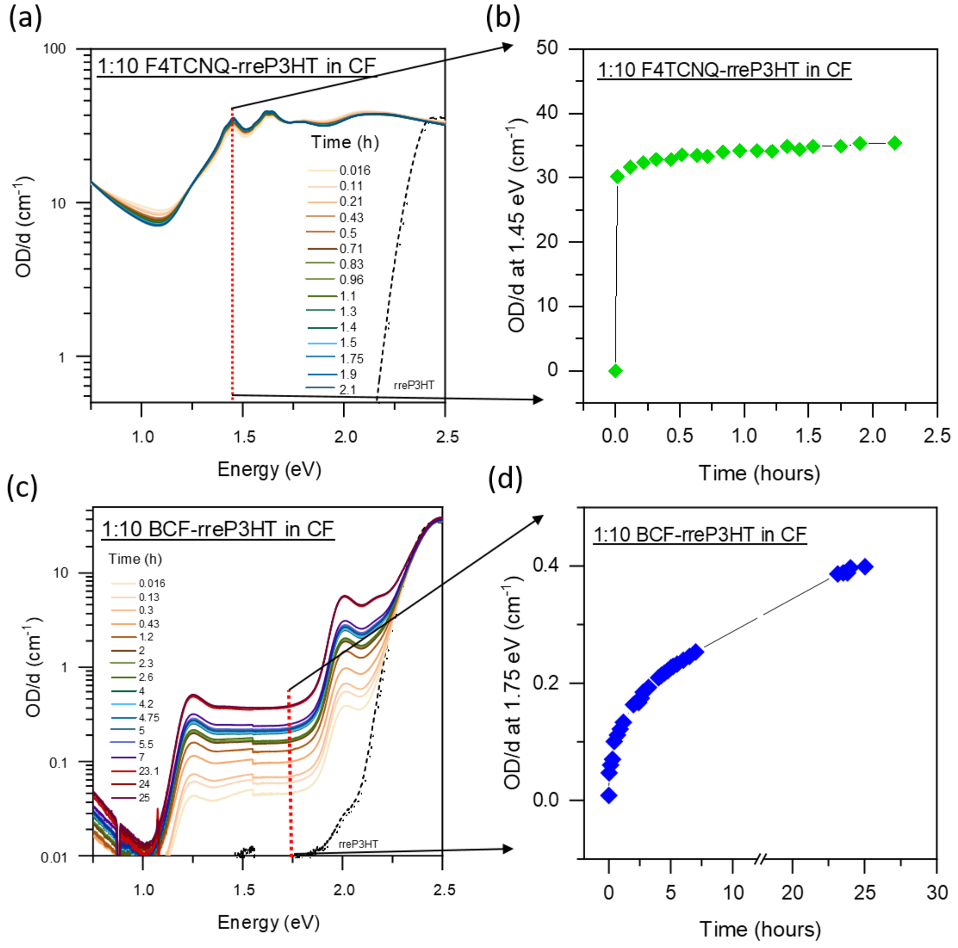

Figure 4.2. UV-Vis-NIR spectra of F_4TCNQ-doped rreP3HT (a) and BCF-doped rreP3HT (c) with the ratio 1:10 measured at different time intervals. The evolution of the F_4TCNQ anion or P3HT polaron absorption signal (OD/d at a specific energy (red dotted line)) with time is plotted in (b) and (d).

4.2 Influence of pre-aggregation

In many conjugated polymers such as poly(p-phenylene) and polythiophenes, doping is typically accompanied by polymer chain stiffening (as seen by the increase in the aggregate signal at ca. 2 eV in Figures 4.1 and 4.2a, 4.2c). This is because oxidation of the polymer chain leads to structural deformations that result in a partial quinoid conformation in some sections of the chain[8] (see Figure 4.3a). Since the quinoid form is characterized by stiff double bonds on the backbone that restrict rotation (unlike the single bonds in the aromatic form), ordered structures known as *doping-induced aggregates* are formed already in solution. McFarland et al. have demonstrated that the chain conformation in rreP3HT solutions has a significant influence on the kinetics of charge transfer doping.[152] For example, rreP3HT in its aggregated "nanowisker" form undergoes p-doping with F_4TCNQ at a much faster rate than completely solubilized rreP3HT chains.[152] This difference in charge transfer kinetics is mainly attributed to the lower oxidation potential of ordered P3HT compared to disordered P3HT chains.[153-154] Moreover, the presence of aggregates is also attributed to increased doping (ionization) efficiency, due to improved charge delocalization in the aggregated sections.[113, 152, 155]

Aggregate formation in an undoped polymer solution is typically induced by the introduction of a marginal solvent, which interferes with the polymer-(good)solvent interaction and drives the chains into self-organization (known as *solvent-induced aggregation*).[156-159] For example, when dissolved in a good solvent like CF, undoped rreP3HT chains typically adopt a random coiled conformation. This is confirmed by the featureless UV-Vis-NIR absorption at ca. 2 eV in Figure 4.3, which is assigned to the absorption from a distribution of conjugated P3HT lengths.[160] With the addition of ca. 5 vol% of the non-solvent ethyl acetate (ETA) to the undoped rreP3HT solution, some of the chains undergo planarization and aggregation,[52] as confirmed by the increase in the aggregate absorption signal at 2.03 eV in Figure 4.3. Therefore, we used this method to study the influence of pre-aggregation on the kinetics of BCF doping of rreP3HT in solution, the results of which are depicted in Figure 4.4.

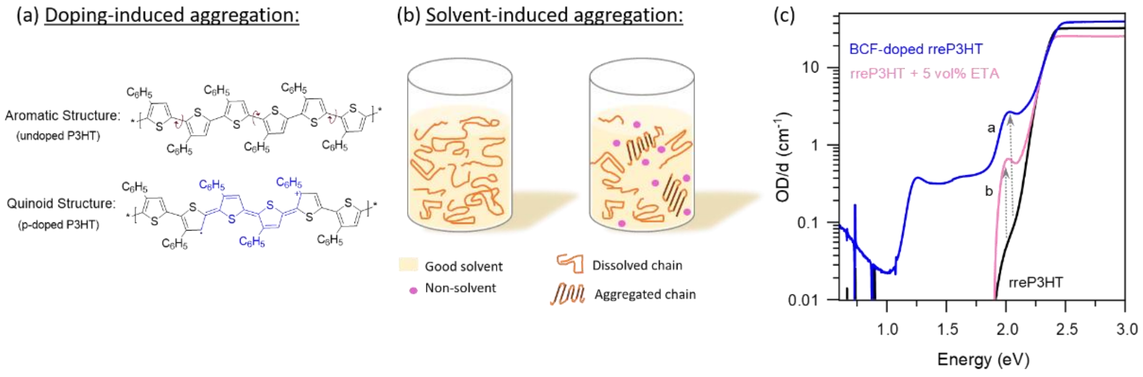

Figure 4.3. a) Change in the structure of P3HT chains from its aromatic form which has a higher rotational freedom in the undoped state to the quinoid form where rotation between repeat units is restricted by the double-bond which is created upon p-doping. b) Schematic of solvent-induced aggregation of dissolved polymer chains, which is caused due to the presence of non-solvent molecules. c) UV-Vis-NIR solution spectra (in CF) of undoped rreP3HT (black), 1:100 BCF-doped

rreP3HT (blue) and rreP3HT with 5 vol% ETA (pink), indicating dissolved/coiled chains, doping-induced aggregates and solvent-induced aggregates respectively

Figure 4.4a and 4.4b show the UV-Vis-NIR spectra of regular (non-aggregated) rreP3HT solution (cuvette-1) and pre-aggregated rreP3HT, the latter of which was prepared by adding ca. 0.5vol% of ETA to the polymer solution (cuvette-2) in air. As expected, the aggregate signal at 2.03 eV increases (pink dashed lines) with the addition of the non-solvent, thus indicating solvent-induced aggregation of the chains. The gradual increase of the signal implies that it is a slow process. Upon doping with BCF, both solutions show the characteristic P3HT polaron bands between 1.25 eV to 1.8 eV as well as the doping-induced aggregate feature at 2.03 eV, thereby indicating ICT. In order to follow the kinetics, the aggregate absorption signal at 2.03 eV and the P3HT polaron signal at 1.75 eV are plotted as a function of time, and shown in Figure 4.4c and Figure 4.4d respectively. Note that the aggregate kinetics is plotted from the time of the first measurement of the two solutions: corresponding to 1 minute after BCF addition in cuvette-1, and 1 minute after ETA addition in cuvette-2. On the other hand, the polaron kinetics is plotted from the time of BCF addition to the two cuvettes.

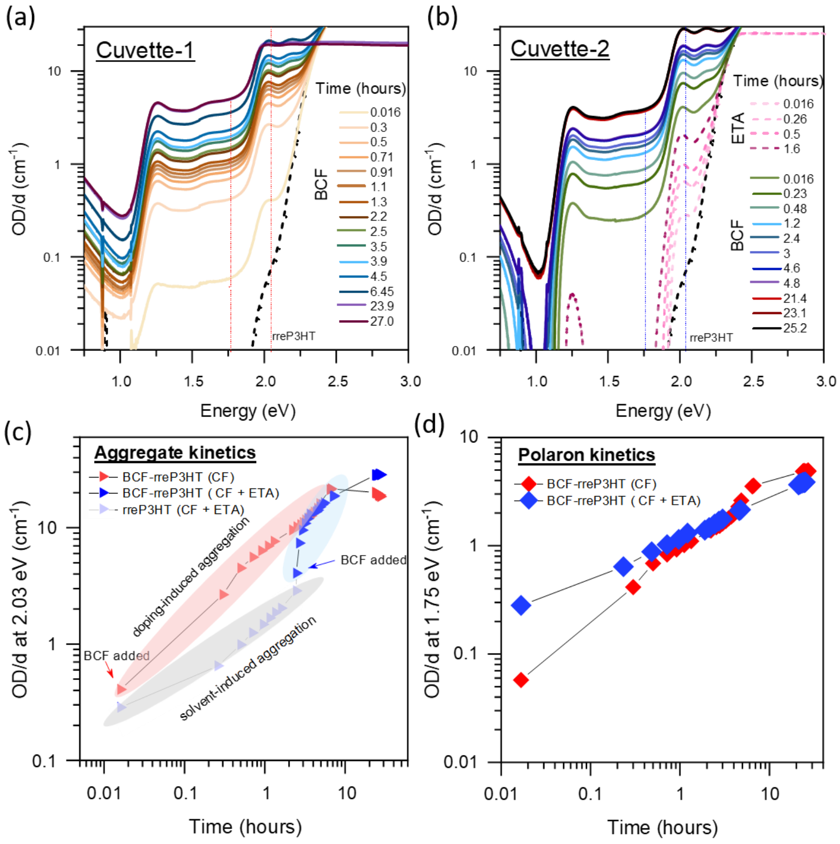

Figure 4.4. UV-Vis-NIR spectra of non-aggregated (a) and pre-aggregated rreP3HT (b) solution doped with BCF in the ratio 1:10 (BCF:3HT) in CF. The evolution of the aggregate signal (at 2.03 eV) with time in both solutions is plotted in (c) (refer footnote [e]) and the evolution of the polaron signal (at 1.75 eV) with time is plotted in (d). The solid symbols in (c) and (d) refer to the experimental OD/d value; the black lines connecting the data-points are guides to the eye. (Note that some spectra are omitted in (a) and (b) to avoid overcrowding of the lines, but the corresponding values are considered in (c) and (d)).

Let us first evaluate the *aggregate kinetics* plotted in Figure 4.4c. In cuvette-1 (red curve) which contains non-aggregated rreP3HT, upon BCF addition, the absorption signal from the doping-induced aggregates (shaded red) increases from ~0.4 to ~7.0 in the first hour, continues increasing gradually over the next few hours.[e] In cuvette-2 (blue curve), the measurements in the first ~2 hours pertain to solvent-induced aggregation (shaded grey) in undoped rreP3HT. Here, the aggregate

---

[e] Note that the aggregate signal shown in Figure 4.4c for the measurements after 20 h are most likely underestimated since the high signal was cut-off by the instrument's detector, as seen in Figure 4.4a.

signal increases at a slower rate (as indicated by the lower slope) from ~0.28 to ~2.8 in two hours. With the addition of the dopant to cuvette-2, more chains undergo aggregation, as seen from the sudden increase in the slope (shaded blue). Notably, in both cuvettes, the magnitude as well as the growth rate of the aggregate signal coincide within ca. 3-4 hours after dopant addition, which suggests that pre-aggregation of the polymer chains does not accelerate aggregate formation during BCF doping. (As mentioned previously, the difference in the magnitude of the signal measured after 20 h in the two cuvettes, is attributed to instrumental limitations.)

Turning now to the effect of pre-aggregation on the *polaron kinetics* shown in Figure 4.4d, what strikes immediately is that apart from the first data point, both the curves (polarons in aggregated and non-aggregated P3HT solutions) match closely. The difference in the polaron level measured immediately after doping, could be due to 1) a true pre-aggregation effect, wherein the aggregated chains improved charge transfer at the initial stages of doping, 2) background doping from ETA, or 3) an un-related coincidence/anomaly. Since these measurements were performed in ambient air as opposed to an inert atmosphere, the occurrence of background doping cannot be discounted[161]. Moreover, the solution is measured in a non-equilibrium state, with each measurement lasting ca. 8 minutes which means that the polaron level measured immediately (1 minute) after doping is inconsistent. Therefore, we attribute the difference to a combination of factor 2) and 3). Importantly, these results suggest that the magnitude as well as the rate of polaron formation via BCF doping is predominantly unaffected by the presence of aggregated chains prior to doping. This is further demonstrated in the next section.

4.3 Influence of light and solvent

Apart from the slow kinetics of doping, we often faced problems with inconsistency and reproducibility of the sample during experiments with BCF doped rreP3HT solutions. For example, the P3HT polaron level in Figure 4.2c and Figure 4.4b differ by nearly an order of magnitude despite the doping ratio being the same. Moreover, there were instances when the polaron signal was negligible/absent in the dopant:polymer solution. After repeated trials in which we varied different parameters such as polymer concentration, pre-aggregation, doping level, oxygen exposure etc., we realized that the polaron level in BCF doped rreP3HT solutions might be influenced by light exposure.

In order to verify this, we prepared doped solutions of three different doping ratios (1:100, 1:40, 1:10 BCF:3HT repeat unit) in a dark room equipped with only a small red LED lamp to be able to see and conduct the experiment (referred as Experiment-1). The solutions were prepared and transferred into cuvettes (for absorption measurement) inside the glovebox, so as to avoid contact with oxygen. The UV-Vis-NIR absorption spectra of the solutions were then measured after ca. 1 h, and 24 h, during which the cuvettes were stored in the dark. Following this, the cuvettes were exposed to white light (from a standard table lamp), and the absorption spectra were measured initially and every 30 minutes for ca. 3 h, and finally on the next day (≈ 48 h since solution preparation). Thereafter, this experiment was repeated, but this time such that the doped solutions were exposed to light throughout the preparation, measurement, and storage periods (we refer to this as Experiment-2). To be able to follow the kinetics, the absorption signal at 1.75 eV (pertaining to the P3HT polaron) of the spectra in both experiments is plotted as a function of time, and shown in Figure 4.5.

We see from the graph in Figure 4.5a (Experiment-1) that there is no discernible absorption signal initially in the three cuvettes that were kept in the dark. The signal remains low even after 24 h, indicating the absence or negligible concentration of P3HT polarons in the doped solutions. However, when exposed to light, the same solutions show a strong increase in absorption within minutes. The signal continues to increase in a sublinear manner over the next few hours and reaches equilibrium by the next day. This is similar to the results of Experiment-2 shown in Figure 4.5b, wherein the doped solutions were exposed to light throughout. Already from the first measurement (ca. 1 h after solution preparation), the solutions display sub-band gap absorption assigned to P3HT polarons, with the signal strength being proportional to the doping ratio. As before, the signal increases sublinearly with time, and reaches saturation by 24 h. We note that the final doping level in the 1:10 and 1:40 ratio solutions that were exposed to light is lower than expected. This is presumably an experimental error caused by a lower concentration of BCF in the dopant solution at the time of mixing.

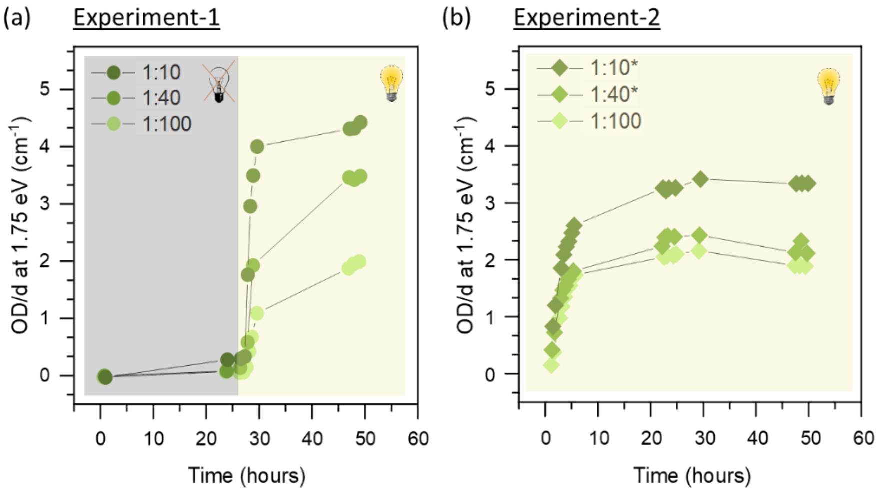

Figure 4.5. Evolution of the doping-induced P3HT polaron absorption signal (OD/d at 1.75 eV) with time, and light exposure for 1:100, 1:40 and 1:10 ratio BCF-doped rreP3HT solution in chloroform. In Experiment-1 (a) the samples were prepared and kept in the dark for the first 24 h and then exposed to light. In Experiment-2 (b) the samples were exposed to light throughout (* the actual doping level in these solutions may be lower). The final P3HT concentration in all 6 solutions was 1.78 mg mL^{-1}.

Now that it was established that BCF doped rreP3HT solutions require light activation for charge transfer to occur, we wanted to check whether this is a solvent-selective phenomenon. To that end, we repeated the above experiment with chlorobenzene (CB) which dissolves both rreP3HT and BCF well. One set of doped solutions (referred to as Experiment-1) was again kept in the dark for 24 h, and subsequently exposed to light, whereas the other set of solutions (referred to as Experiment-2) was exposed to light throughout the preparation, measurement and storage stages. In order to be able to compare the results in CF and CB, all other experimental conditions such as polymer and dopant concentration, measurement duration were kept the same. The UV-Vis-NIR absorption of the solutions was measured at different time intervals (initial, after 1 h, 24 h, etc.), and the absorption signal at 1.75 eV of each spectrum was plotted as a function of time. The results of the experiments in CB are compared to that in CF and shown in Figure 4.6.

From the polaron kinetics in CB displayed in Figure 4.6a, we see first of all that strong polaronic absorption is found already from the first measurement (ca. 1 h after preparation), even in the solutions that were kept in the dark (shaded grey). The absorption signal is found to increase further with time despite the absence of light. This is particularly evident for the higher doping concentrations of 1:40 (which saw an increase from 0.9 cm^{-1} when measured 1 h after preparation to ca. 4.0 cm^{-1} when measured after 23 h) and 1:10 (which increased from 4.6 cm^{-1} to 8.0 cm^{-1} when measured after 1 h and 23 h respectively). Although this appears to suggest that light might not play a role in polaron formation in CB, we found that when the same solution was subsequently exposed to light, the absorption increased from 4.0 cm^{-1} to 6.1 cm^{-1} in the 1:40 ratio solution and from 8.0 cm^{-1} to 9.9 cm^{-1} in the 1:10 solution, both within 7 h of light exposure (see the slope change in Figure 4.6a).

The positive influence of light on the kinetics of polaron formation is also validated by the results of Experiment-2 in Figure 4.6, in which the solutions were exposed to light from the beginning. Within the first 5 h, the signal is found to increase rapidly from 1.8 cm^{-1} to ca. 5.0 cm^{-1} in the 1:40 ratio solution and from 6.1 cm^{-1} to 9.0 cm^{-1} in the 1:10 ratio solution, and increases further with time, having reached saturation after ca. 20 h. Importantly, the polaron level in Experiment-1 as well as Experiment-2 are fairly comparable at ca. 30 h (except in the 1:100 ratio solution in which the final signal could not be measured due to technical difficulties).

Let us now compare the results in CB to that in CF shown in Figure 4.6b. The most dramatic difference lies in the maximum polaron level attained in the two solvents, particularly in the 1:40 and 1:10 ratio solutions, which is ca. 2 times higher in CB than in CF. Müller and co-workers observed a similar behavior in F_4TCNQ doped rreP3HT solutions,[59] where the ionization efficiency was higher in CB than in CF for the same doping ratio. They attributed this to the difference in the polarity of the two solvents. Since doped solutions contain charged molecules and CF ($E_T^N(CF) = 0.259$) has a higher relative polarity than CB ($E_T^N(CB) = 0.188$),[162] some charges are likely to be screened by the CF, thereby resulting in a lower doping level in the solution.[59] Another observation is that the polaron level increases almost linearly with the dopant concentration in CB, whereas in CF, the accessible polaron level appears to be limited. Apart from the polaron level, it is also evident from Figure 4.6 that <u>light exposure is more crucial for charge transfer to occur in CF than in CB</u>. Although the exact reason for this is still largely unknown, we attempt to explain this in further sections, based on newly reported evidence on the mechanism of Lewis acid doping.[163] Importantly, these results are consistent with EPR experiments on similar BCF-doped rreP3HT solutions performed by Kelvin Yao who was a master student in the Behrends group at the *Freie Universität Berlin* at the time of this work. The EPR results are presented in his master thesis.

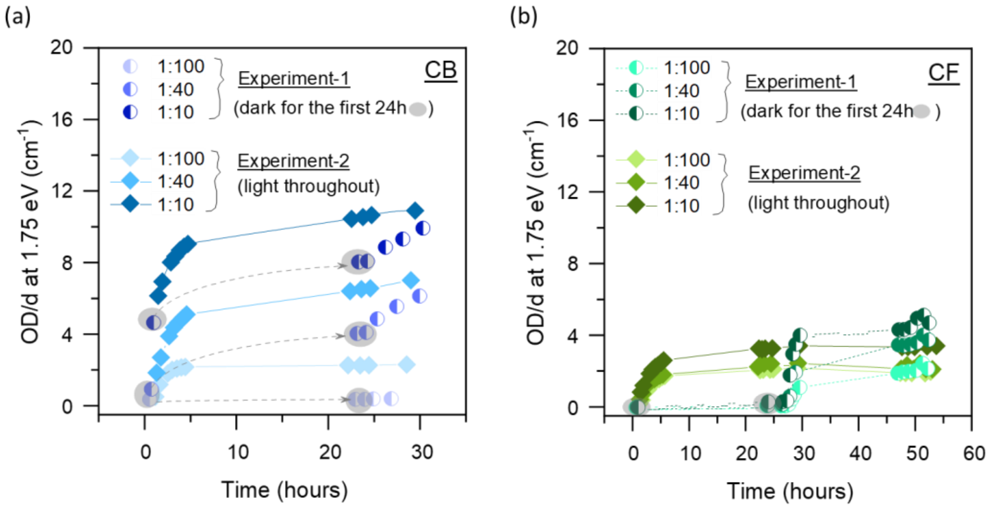

Figure 4.6. Evolution of the doping-induced P3HT polaron absorption signal (OD/d at 1.75 eV) with time, and light exposure for BCF-doped rreP3HT solution in chlorobenzene (a) and chloroform (b). The final P3HT concentration in all the solutions was 1.78 mg mL^{-1}.

Our final objective in this regard was to check if the *duration*, and *time/sequence* of light exposure affected the polaron level in the BCF-doped rreP3HT solution. The solvent of choice was CF due to the higher sensitivity of the doped solutions to light (as shown previously), which would allow for more control of the experimental parameters, and give reliable results. To that end, we performed an experiment in which we prepared a stock solution of undoped and 1:10 BCF doped rreP3HT in CF in the dark (inert atmosphere), divided them into different cuvettes, and systematically varied the conditions they were exposed to, as depicted in Figure 4.7a. For example, cuvette-3 consists of rreP3HT which was exposed to light for 1 h, after which BCF was added (in the ratio 1:10 BCF-rreP3HT) and the cuvette was kept in the dark for the remaining 23 h. In cuvette-4, the rreP3HT was pre-aggregated using ETA and kept in the dark for 1 h. To this, BCF was added (in the dark), and the solution was stored in the dark for the remaining 23 h. Cuvettes 5-7 consisted of 1:10 BCF doped rreP3HT which were either stored in the dark throughout (cuvette-5), exposed to light throughout (cuvette-7), or exposed to a short duration (1 h) of light (cuvette-6). The UV-Vis-NIR absorption spectra of all the solutions measured 24 h after preparation are shown in Figure

4.7a. In order to check for any anomalies, the absorption was also measured at other times (e.g. initially, after 1 h etc.) during the experiment, as indicated by the symbol ◊ in Figure 4.7b. Therefore, it must be noted that even the cuvettes that were kept in the dark were exposed to light from the spectrometer in the wavelength range 2500 nm – 300 nm for a short duration (ca. 6 minutes) during the measurement.

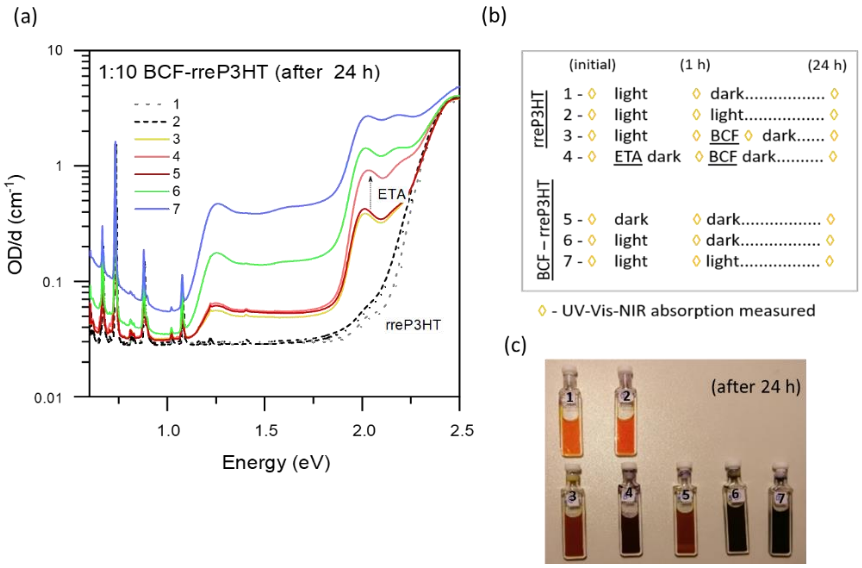

Figure 4.7. (a) UV-Vis-NIR absorption spectra of undoped and 1:10 ratio BCF-doped rreP3HT (final P3HT conc. 1.5 g L^{-1}) exposed to different conditions (mentioned in (b)), measured after 24 hours. (c) Photograph of the solutions after 24 h. We can see already by eye that the doped solutions which were exposed to light (cuvette 7) are much darker in color (thereby indicating a higher level of doping) than the ones kept in the dark for a long time (e.g. cuvette 5 which was exposed to light only from the instrument during the measurements).

From the absorption spectra in Figure 4.7a, we see firstly that the sub-band gap signals assigned to P3HT polarons are found only in the cuvettes containing BCF, which suggests the absence of unintentional light-induced doping/degradation of the rreP3HT. Although some amount of polymer degradation/doping cannot be completely ruled out[161, 164], the concentration is most likely very low, as indicated by the absence of new sub-band gap features in cuvettes-1 and 2.

The second observation is that the P3HT polaron signal (absorption below 1 eV, and between 1.25 to 1.8 eV) in cuvettes-3, 4 and 5, which were predominantly kept in the dark, is very low and at an identical level. As mentioned earlier, the solutions display some amount of doping-induced signals despite being in the dark after BCF addition due to light exposure during the measurement itself. Since cuvette-3 and 5 differ only in the exposure of P3HT to light prior to BCF addition, their comparable polaron level implies that light is crucial for the activation of BCF, rather than the polymer. Moreover, the results also demonstrate that pre-aggregation of rreP3HT chains (as seen by the increase in the aggregate absorption at 2.03 eV in cuvette-4) does not facilitate improved charge transfer between rreP3HT and BCF.

The third observation is that both cuvette-6 and cuvette-7 show strong polaron absorption, once again confirming that light activates BCF for charge transfer with rreP3HT. The optical density at 1.75 eV in cuvette-6 (which was exposed to light for one hour at the beginning) is ca. 3 times higher than that in cuvette-3 (which was in the dark throughout), whereas that in cuvette-7 (which was exposed to light throughout) is over 8 times higher than that in cuvette-3. This confirms that the duration of light exposure is also crucial for BCF doping of rreP3HT.

Deliberate light exposure, or "light soaking" is commonly employed on metal oxides (TiO_2 or ZnO) that are used as electron transporting layers (ETLs) in inverted structure organic solar cells in order to fill electron traps and facilitate easy charge extraction, thereby improving the performance of the device.[165-166] But this does not explain the mechanism at work in our doped solutions. The positive influence of light exposure in BCF doped solutions and films was also observed by Ye and co-workers who used light soaking to improve the doping efficiency and thereby, the conductivity of BCF doped poly[bis(4-phenyl)(2,4,6-trimethylphenyl)amine] (PTAA) films, which were used as hole transporting layers (HTLs) in perovskite solar cells.[97] They postulated a frustrated Lewis pair (FLP)-type of interaction[167] between the BCF and the PTAA, and attributed the improvement in performance to an increased concentration of amine (PTAA) free radicals caused by the light soaking, which then allows for easy charge transfer with BCF and consequently, more amine cations that contribute to hole transport.[97] However, a very recent study by Yurash and coworkers has shown that the mechanism of Lewis acid doping of conjugated polymers does not follow a simple electron transfer process between the polymer and dopant, but rather takes place though a multistep process involving an *endothermic* rate-limiting polymer protonation step, as suggested by DFT calculations.[163] This seems to be a more likely description of the reaction mechanism in our BCF doped P3HT solutions. Presumably, light exposure assists in overcoming the energetic barrier to protonation of the polymer. The possible doping mechanism in BCF doped P3HT in light of Yurash et al.'s findings[163] is discussed in detail in Chapter-5, along with additional results that support the protonation mechanism and its influence by light.

4.4 Conclusion

In this chapter, the important factors influencing the charge transfer process in BCF-doped rreP3HT solution was studied using UV-Vis-NIR spectroscopy. Upon BCF doping, ICT polarons are formed in rreP3HT solutions, but the charge transfer reaction typically takes place over many hours. First, the influence of pre-aggregation of the polymer chains on the doping level and kinetics was checked by adding a small amount of non-solvent to the polymer solution to induce chain aggregation prior to doping. It was found that the slow kinetics of charge transfer in the doped solution largely remained unaffected by pre-aggregation of the polymer chains. On the other hand, light was found to play a critical role on the magnitude of charge transfer as well as the reaction kinetics. This influence was more pronounced in chloroform than in chlorobenzene. It was shown that BCF doped solutions in chloroform prepared and stored in the dark showed negligible amounts of P3HT polarons even after 24 h, whereas strong polaronic absorption was detected within minutes of light exposure. In chlorobenzene, although some polarons were formed despite the absence of light, the kinetics of charge transfer was significantly improved with light exposure. Moreover, the choice of solvent (i.e. polarity) was also shown to impact the observed doping level in the BCF doped solution, due to the charge screening effect of the solvent.

Based on the recently reported Lewis acid doping mechanism[163], it was proposed that light helps in overcoming the energetic barrier to polymer protonation, which is the rate-limiting step in the BCF doping process. Although only a brief discussion was presented here, the results serve as an important basis for reliable sample preparation and evaluation in subsequent chapters.

Importantly, the influence of light exposure (and its duration) on the polaron formation in BCF doped solutions imply that results from optical spectroscopy (which can also influence the results) must be interpreted with caution, and ideally accompanied by other non-invasive measurement techniques, particularly for quantitative estimations.

In a broader context, these findings highlight the importance of understanding the various external parameters that might influence the results of an experiment. Careful control of the sample preparation conditions is critical for obtaining reliable and reproducible results.

5. Comprehensive Analysis of the Optical Signatures of p-Doped P3HT in Solution[f]

As mentioned in Chapter-2, we know that in organic semiconductors, doping occurs either via integer charge transfer (ICT) or charge transfer complex (CTC) formation.[36-37] In general, ICT is preferred over CTC formation, since the former directly leads to the presence of ions in the system, whereas in the latter, the system is still electrically neutral in the ground state. Despite extensive research over the past years, the exact factors determining the *doping mechanism* in a given dopant-host system are still unknown. There is, however, a growing body of research which demonstrates that the *degree of charge delocalization* has an influence on the prevalent *doping mechanism* in a particular dopant-host system. For example, dopant-polymer systems traditionally exhibiting ICT have been recently shown to undergo CTC formation when the degree of disorder in the system is intentionally increased.[38-39, 85] It has also been suggested that a high degree of conformational order in the host material is required for efficient charge transfer between the host and dopant.[113]

Optical absorption spectroscopy is arguably the most widespread tool for characterizing doping processes. As explained in section 2.2.4 and demonstrated in Chapter-4, doping induces new sub-band gap states in the host material, which can be probed by optical spectroscopy. Apart from revealing differences in the charge transfer mechanism [36-37, 58, 85], the optical spectrum is also sensitive to the polymer backbone conformation and intermolecular coupling.[54, 118, 168-169] For example, it has been shown that although polarons on aggregated P3HT chains (rreP3HT) typically display a P_1 transition peak below 0.35 eV and a double-peaked P_2 transition at ca. 1.3 eV and 1.7 eV, the corresponding P_1 and P_2 bands are blue-shifted in non-aggregated P3HT (rraP3HT) samples.[118] Moreover, the double-peaked P_2 transition on aggregated rreP3HT chains is found to transform into a single peak at 1.35 eV in isolated rreP3HT chains and at 1.5 eV in non-aggregated rraP3HT chains.[118] These differences in the optical transitions are mainly attributed to the ability of the charge to be delocalized along and among the polymer chains (which is easier in rreP3HT

---

[f] Results shown in this chapter have been published in ref 146. Arvind, M., et al., Quantitative Analysis of Doping-Induced Polarons and Charge-Transfer Complexes of Poly(3-Hexylthiophene) in Solution. *The Journal of Physical Chemistry B* **2020**, *124*, 7694-7708.

compared to rraP3HT). This demonstrates the close interplay between the *optical signatures* of the charged species, the *structural order* and the *degree of charge delocalization*.

Another prevailing issue is that the exact nature of the doping-induced species observed by optical spectroscopy is still under debate in the scientific community. For example, the P_2 transition near 1.65 eV in doped rreP3HT films have been assigned to polarons as well as bipolarons.[36, 119] This could be because, 1) the variations in the optical signatures (transitions) of the species are subtle as such[170], making it hard to identify and differentiate between them without reliable complementary measurement techniques, 2) the optical transitions of the counter-ion may overlap with that of the polaron/bipolaron on the host (e.g. in the case of F_4TCNQ-doped rreP3HT[36, 150]), thereby preventing a clean analysis of the individual signatures and 3) as mentioned earlier, the optical transitions observed in doped films are also sensitive to the structural order and chain conformations[113, 118, 169], which is in turn influenced by the processing conditions[85].

Therefore, in this chapter, we address some of these issues by investigating the role of structural order of the polymer backbone on the optical signature of the doping-induced species and the prevalent doping mechanism. This was done by performing a comprehensive analysis of the *nature* of the doping-induced species formed when (p-) doping the model polymer P3HT in its regioregular and regiorandom forms, using optical absorption and electron paramagnetic resonance (EPR) spectroscopy. As mentioned in section 2.2.3, EPR is sensitive to polarons but not CTCs or bipolarons, and hence serves as an ideal complement to optical techniques. Three different molecular dopants were considered for this study: the prototypical planar molecule F_4TCNQ, the bulky Lewis acid dopant BCF, and the bulky organometallic complex Mo(tfd-CO_2Me)$_3$.[44-45, 51, 59, 93] Since both the BCF and the Mo(tfd-CO_2Me)$_3$ anions are found to not absorb strongly in the sub-band gap region of P3HT (*vide infra*), the problem of spectral overlap of the P3HT polaron and the dopant counter-ion is avoided. Complications in the interpretation of the optical spectra arising from the multiphase morphology in solid films is prevented by selectively studying the processes occurring in *doped polymeric solutions*.

The discussion in this chapter is divided into two parts. In the first section we discuss our approach towards identifying the *optical signature* and the *nature of the different doping-induced species* in doped P3HT solutions. In the second part we present insights into the role of structural order on the observed optical signals and thereby, the doping mechanism.

5.1 Identifying the nature of the doping-induced species in p-doped P3HT

5.1.1 Insights from UV-Vis-NIR spectroscopy

Doped rreP3HT

Figure 5.1 shows the UV-Vis-NIR spectra of rreP3HT solutions doped with F_4TCNQ, Mo(tfd-$CO_2Me)_3$ and BCF in the ratio 1:100 (one dopant molecule per 100 repeat units of 3-hexylthiophene (3HT)). This particular doping ratio was chosen as it provides a high enough sub-band gap signal without compromising the homogeneity of the doped solution. This is especially relevant since both F_4TCNQ and doped P3HT chains suffer from low solubility at high concentrations. The final P3HT concentration in the sample after doping was 2 mg mL^{-1} for all three solutions. Additional details about the sample preparation and measurement are provided in Chapter-3.

While differing in intensity, all three systems exhibit the same NIR features, namely, a low energy feature extending below 0.5 eV, and a broad shoulder (possibly comprising two peaks) in the 1.25 eV – 1.75 eV range. We assign this to the dopant-induced ICT polaron on the P3HT backbone, based on previous studies [36, 118, 169]. As discussed in section 4.1, the F_4TCNQ-doped rreP3HT solution additionally shows the characteristic twin peaks of the F_4TCNQ radical anion at 1.4 eV and 1.6 eV. [36, 150] In the case of Mo(tfd-$CO_2Me)_3$-doped rreP3HT, although a weak absorption signal from the Mo(tfd-$CO_2Me)_3$ radical anion is expected around 1.25 eV and 2.0 eV (see [93] and Appendix Figure A.1), it is overshadowed here by the signal of the P3HT polaron. Similarly, the BCF-doped rreP3HT spectrum is dominated by the signal from the P3HT polaron. As discussed in Chapter-4, the apparent absence of the BCF radical anion signal could either be due to 1) a weak oscillator strength of the species, hence causing it to be buried under the P3HT polaron signal or 2) due to the chemical transformation into other species [147, 163], which do not absorb in the spectral region of concern. Lastly, unlike the undoped rreP3HT spectrum, all three doped rreP3HT spectra display strong π-π aggregate absorption at 2.02 eV, indicating doping-induced aggregation.[40]

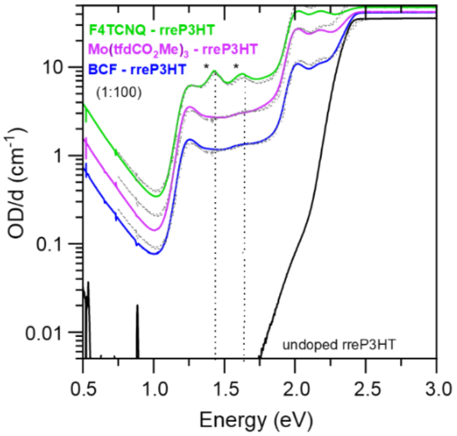

Figure 5.1. UV-Vis-NIR absorption spectra of solutions (in chloroform) of rreP3HT doped with F_4TCNQ, Mo(tfd-CO_2Me)$_3$ and BCF in the ratio 1:100 (dopant : repeat unit).The dashed grey lines correspond to the spectra reconstructed using the Beer-Lambert law. The characteristic F_4TCNQ radical anion double peaks (*) are highlighted for reference.

Since all three doped solutions exhibit ICT with rreP3HT, we were able to analyze the spectra to estimate the *ionization efficiency*, i.e. the fraction of P3HT polarons formed per added amount of neutral dopants. This was done using the Beer-Lambert Law:

$$(OD/d) = \ \varepsilon_{(dopant\ anion\ +\ P3HT\ polaron)} \times c \times X \tag{5.1}$$

where OD/d is the absorbance normalized to the path length (d) of the cuvette, ε is the molar extinction coefficient of the absorbing species, c is the molar concentration of the applied dopant and X denotes the fraction of applied dopants that undergoes ionization to form charged polymer (and dopant anion). The $\varepsilon_{F4TCNQ\ anion}$ spectrum was taken from literature [150]. The $\varepsilon_{P3HT\ polaron}$ spectrum was estimated as a part of my master thesis[48], with the procedure described also in ref[49]. Since the BCF and Mo(tfd-CO_2Me)$_3$ anion signals are absent or buried in our measured spectra, only the $\varepsilon_{P3HT\ polaron}$ term has been considered, and the $\varepsilon_{dopant\ anion}$ term has been neglected for the corresponding calculations. The spectra were fitted to the experimental curves by determining the X values that yield the closest fit at 1.25 eV (for the F_4TCNQ doped solution) or 1.5 eV (for the BCF and Mo(tfd-CO_2Me)$_3$ doped solutions). The reconstructed spectra are shown as dashed lines in Figure 5.1. The reference and fitted molar extinction coefficient spectra are shown in the Appendix (Figure A.2).

These calculations indicate that nearly 66% of the added F_4TCNQ molecules underwent ionization to form P3HT polarons and F_4TCNQ anions, consistent with previous reports.[36] On the other hand, only ca. 35% of the added Mo(tfd-CO_2Me)$_3$ and 15% of the BCF underwent ionization to form P3HT polarons in the corresponding solutions. Moreover, we found that Mo(tfd-CO_2Me)$_3$ undergoes slow charge transfer with rreP3HT (see Figure A.1), as in the case of BCF-doped rreP3HT. The differing kinetics of charge transfer could be due to steric hindrance between the dopants and the polymer chains[44, 49], but could also be caused by the energy level offsets. For example, Mo(tfd-CO_2Me)$_3$ has a lower EA (~ 5.0 eV) compared to F_4TCNQ (EA ~ 5.24 eV), which would imply a smaller driving force for electron transfer from the P3HT HOMO. In the case of BCF doping, as discussed in Chapter-4, the additional endothermic protonation step which is believed to occur[163] presumably poses additional kinetic barriers to the charge transfer reaction. As demonstrated in section 4.3 and below, light exposure appears to improve the ionization efficiency.

Importantly, despite the very different chemical nature and shape of the three dopants, and possibly a different pathway for polaron formation, the shape of the dopant-induced NIR absorption is identical for all three dopant molecules (see also Figure A5.2). Since the P3HT polaron spectrum is sensitive to the degree of charge localization and interchain interaction,[54] the *insensitivity* of the doping-induced NIR spectra to the choice of the dopant provides first evidence of a very similar nature and environment of the doping-induced species in rreP3HT solution.

Doped rraP3HT

On the other hand, the optical spectra of doped rraP3HT solutions reveal several differences compared to the results obtained with rreP3HT.

Let us first consider the situation in F_4TCNQ-doped rraP3HT. The UV-Vis-NIR spectra of 1:100 and 1:10 ratio F_4TCNQ-doped rraP3HT solutions are shown in Figure 5.2a. Similar to the doped rreP3HT samples, the 1:100 ratio doped rraP3HT solution has a final P3HT concentration of 2 mg mL^{-1}, but the 1:10 ratio solution has a lower concentration (1.25 mg mL^{-1}) due to the low solubility of F_4TCNQ. From Figure 5.2a we see that although the doped rraP3HT solutions display pronounced sub-band gap absorption indicating charge transfer (doping), the *shape* as well as the *spectral position* differ substantially from those in F_4TCNQ-doped rreP3HT. The characteristic F_4TCNQ anion peaks are almost absent (a faint peak at ca. 1.4 eV is visible in 1:100 F_4TCNQ-doped rraP3HT). Instead, the sub-band gap absorption of F_4TCNQ-doped rraP3HT consists of a broad feature between 0.8 and 1.2 eV (probably composed of two peaks), and an additional broad peak at ca. 2.0 eV. Also, the characteristic peak of P3HT chain aggregation is missing.

Notably, the spectra are very similar to the film spectra of F_4TCNQ-doped quaterthiophene (4T), which was attributed to CTC formation.[58] Similar UV-Vis-NIR features (broad absorption bands at around 1.1 and 2.1 eV) were also observed in F4TCNQ-doped rraP3HT films[39] and P3EHT films (a polythiophene-derivative with branched side chains) [38], and were assigned to a CTC. Moreover, recent simulations of the optical spectra of CTCs formed in F_4TCNQ-doped oligothiophenes display a similar three-peak structure as in Figure 5.2a, though blue-shifted compared to our spectra.[171] This is reasonable considering that the simulations were conducted *in vacuo*, whereas the experimental data shown here are strongly influenced by interactions with the solvent medium.

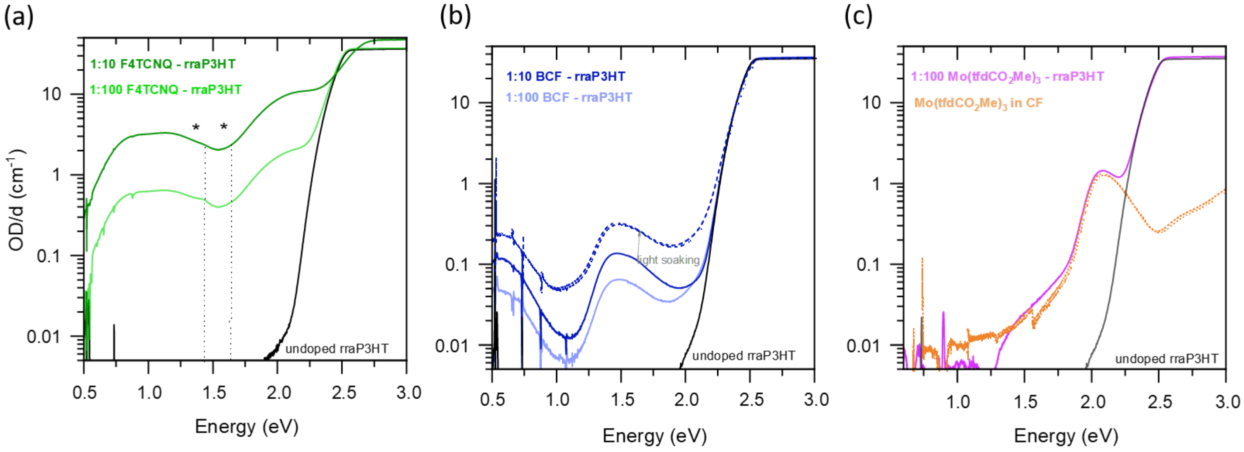

Figure 5.2. UV-Vis-NIR absorption spectra of rraP3HT solution (in chloroform) doped with a) F_4TCNQ (1:100 and 1:10), b) BCF (1:100, 1:10, light-soaked 1:10), and c) Mo(tfd-CO$_2$Me)$_3$ The spectrum of the doped solution in (c) consists of the superimposed spectra of the neutral dopant and the undoped polymer, with no new absorption features, thereby indicating that Mo(tfd-CO$_2$Me)$_3$ does not dope rraP3HT. (Note: the kink near 1.5 eV in the neutral Mo(tfd-CO$_2$Me)$_3$ spectrum is an artifact due to the detector change in the instrument.)

Let us now consider the UV-Vis-NIR spectra of BCF-doped rraP3HT solutions shown in Figure 5.2b, in comparison to that of BCF-doped rreP3HT (shown in Figure 5.1). The low energy absorption in the BCF-doped rraP3HT sample blue-shifts to ca. 0.65 eV (from <0.5 eV in rreP3HT) and the broad absorption between 1.25 – 1.75 eV is replaced by a single peak at 1.5 eV. Again, there is no evidence for backbone planarization/aggregation at ca. 2 eV. Moreover, the doping-induced signal is rather weak for both the 1:100 and the 1:10 solution, indicative of either a low concentration of doped polymer segments, or the formation of a species with very low oscillator strength. We were however, able to increase the signal by a factor of two by light soaking/ illumination as with BCF-doped rreP3HT solutions. Once again, no additional peaks which can be assigned to the BCF anion were observed (in the spectral range considered here).

Similar absorption features as shown in Figure 5.2b have been reported in literature and assigned to *polarons located in amorphous P3HT domains* or on individual chains.[118, 169, 172] Moreover, during my master thesis studies, I had observed that upon heating BCF-doped rreP3HT solutions (in chlorobenzene) beyond 70 °C, the characteristic P3HT polaron absorption in the NIR region of the spectrum transforms into a broad peak centered around 1.5 eV.[48-49] This was accompanied by the suppression of the P3HT aggregate peak at 2 eV, which suggested that the characteristic NIR absorption we see in BCF-doped rraP3HT might originate from a more *localized P3HT polaron* that is present on individual non-aggregated chains. [49] This assignment was recently confirmed by Mansour et al. who showed that the same absorption features are observed in *filtered solutions* of BCF-doped rreP3HT wherein the aggregated P3HT chains have been physically removed.[173]

Lastly, the UV-Vis-NIR spectra of Mo(tfd-CO_2Me)$_3$-doped rraP3HT shown in Figure 5.2c display no features in addition to the absorption of neutral rraP3HT and the neutral dopant. Therefore, we concluded that Mo(tfd-CO_2Me)$_3$ does not dope rraP3HT, presumably due to the energetic barrier ($IE_{rraP3HT} \approx 5.25$ eV, $EA_{Mo(tfd\text{-}CO2Me)3} \approx 5.0$ eV)[51, 149] for charge transfer to occur.

To briefly summarize this section, the UV-Vis-NIR experiments on doped P3HT solutions suggest that the three different dopants form essentially the same type of doping-induced charge carrier on *regioregular* P3HT chains, whereas each dopant interacts differently with *regiorandom* P3HT chains. Based on peak assignments reported in literature, the spectral features are assigned to *P3HT polarons* (in doped rreP3HT), *charge transfer complexes* (in F4TCNQ-doped rraP3HT), and *"localized" P3HT polarons* (in BCF-doped rraP3HT). In order to verify our assignment of the spectral features to the doping-induced species and to gain additional information about the nature and environment of the species, we turn to EPR spectroscopy.

5.1.2 Insights from EPR spectroscopy

As mentioned earlier, doping-induced *polarons* formed via ICT have unpaired electrons in their ground state whereas bipolarons as well as CTCs are diamagnetic in their ground state. As a result, samples containing ICT polarons will be EPR-active whereas bipolarons and CTCs will be EPR-silent. Therefore, if the experimental conditions are kept identical, the qualitative and quantitative information from EPR and UV-Vis-NIR combined will provide insight into the nature of the species, and their optical signatures can be confirmed.

Figure 5.3 shows the X-band room temperature continuous wave EPR (cwEPR) spectra of doped rre- and rraP3HT solutions. These EPR measurements were made in parallel to the UV-Vis-NIR experiments (shown in Figure 5.1 and Figure 5.2), from the same batch of solutions to enable a direct comparison between the two sets of data. Since the EPR measurement and data analysis was not performed by me,[g] only a brief discussion which is relevant for this thesis is presented here. The corresponding joint publication[146] contains a detailed description of the EPR measurement technique and analysis.

Let us first consider the EPR spectra of doped rreP3HT shown in Figure 5.3a. The top half of the graph compares the signal intensities from the three doped solutions. All three samples show an EPR signal, thereby confirming the presence of unpaired electrons in the respective solutions. Notably, the EPR spectrum of the F_4TCNQ doped solution has a much higher signal intensity, indicating a higher concentration of unpaired electrons in comparison to the other two systems. As mentioned in earlier sections, the shape and position (g-factor) of an EPR spectrum is unique to a particular paramagnetic species and reveals important information about the local environment of the unpaired electron. In our case, the Mo(tfd-CO_2Me)$_3$ and BCF-doped rreP3HT solutions show an EPR signal at $g = 2.0022$. Unlike the BCF-doped sample, the Mo(tfd-CO_2Me)$_3$-doped rreP3HT shows an additional signal at $g = 2.0085$, of equal integrated intensity as the other signal (at $g = 2.0022$). On the other hand, the F_4TCNQ-doped rreP3HT solution shows an EPR signal at $g = 2.0025$, superimposed by a partially resolved hyperfine structure[h].

---

[g] The EPR measurements and data analysis were done by Dr. Claudia E. Tait (Berlin Joint EPR Lab, *Freie Universität Berlin*)

[h] Hyperfine structure typically arises from interactions between the e^- cloud and the magnetic nuclei (in this case ^{14}N and ^{19}F) that result in additional splitting of the electron spin energy levels and therefore splitting of the EPR line.

Based on literature,[174] the EPR signal at $g = 2.0022$ can be assigned to the radical cation on the P3HT backbone, thereby confirming the presence of ICT *polarons* in both Mo(tfd-CO_2Me)$_3$- and BCF-doped rreP3HT solutions. The additional signal in the Mo(tfd-CO_2Me)$_3$-doped sample most likely stems from the Mo(tfd-CO_2Me)$_3$ *radical anion*, as others report similar *g*-values for related monoanionic molybdenum complexes[175-176]. Based on additional EPR experiments on the F_4TCNQ radical anion generated in tetrahydrofuran (see Appendix Figure A.3), we assign the contribution with resolved hyperfine structure in the F_4TCNQ-doped rreP3HT solution to a small fraction of free F_4TCNQ *radical anions* in the system (ca. 1% of the observed unpaired electrons). The EPR signal of free F_4TCNQ radical anions was found to be centered at $g = 2.0030$. Since our F_4TCNQ-doped rreP3HT solution shows an EPR signal at $g = 2.0025$, which is intermediate between that of the P3HT radical cation ($g = 2.0022$) and the free F_4TCNQ radical anion ($g = 2.0030$), based on similar observations reported in literature,[177-179] we infer that the P3HT aggregates in the F4TCNQ-doped solution consist of *exchange-coupled*[i] F_4TCNQ radical anions and P3HT radical cations.

The lack of an additional EPR signal assigned to a BCF *radical anion* in the BCF-doped rreP3HT solution reinforces the notion of a further reaction of this species [147, 163]. However, the absence of *any* other EPR signals apart from that of the P3HT radical cation is inconsistent with the Lewis acid doping mechanism as proposed by Yurash et al.,[163] according to which we would expect an EPR signal from a *neutral radical* on a *protonated* P3HT chain. This will be addressed in detail in subsequent sections.

---

[i] Exchange interaction is the interaction between two magnetic species (atoms or molecules) that stems from the spin configuration in the species and arises in the presence of overlap of their electronic wavefunctions.

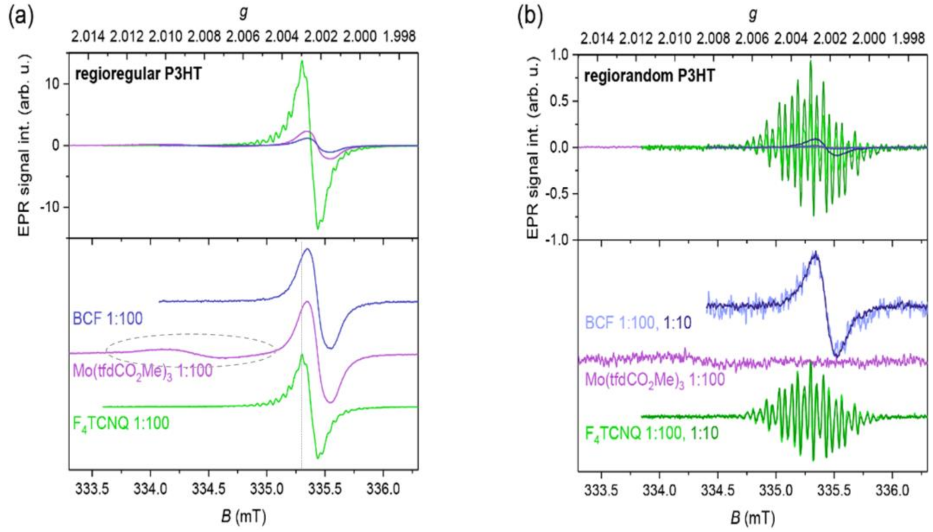

Figure 5.3. X-band room temperature cw EPR spectra recorded on solutions of rreP3HT (a) and rraP3HT (b) doped with F_4TCNQ, BCF or Mo(tfd-CO_2Me$)_3$ in chloroform at doping ratios of 1:100 (and 1:10 for rraP3HT). The signal intensities normalized by Q-factor and modulation amplitude are compared in the top part of the graphs and the normalized spectra are shown in the bottom part for comparison of the spectral shapes. The signal from the Mo(tfd-CO_2Me$)_3$ anion is highlighted by the dashed grey line. The spectra are shown for a microwave frequency of 9.4 GHz, additional details are described in the corresponding publication[146]

Next, we turn to the EPR spectra of doped rraP3HT solutions shown in Figure 5.3b. Notably, the signal in all three systems are significantly weaker compared to that in rreP3HT for the same doping ratio (1:100) and P3HT concentration, thereby implying a lower concentration of unpaired electrons in the solutions. In case of the Mo(tfd-CO_2Me$)_3$-doped rraP3HT, the signal appears to consist almost exclusively of a weak signal from the monoanionic dopant (g =2.0085), presumably formed due to adventitious reduction by water. The BCF-doped rraP3HT solutions show a weak signal at g = 2.0022 assigned to the P3HT *radical cation*, and no other signal arising from the BCF radical anion or other paramagnetic species in the system. The EPR signal of the F_4TCNQ-doped rraP3HT solution comprises the signal from the free F_4TCNQ radical anion, and the P3HT radical cation, but the concentration of spins is significantly lower in rraP3HT, as shown below.

Table 5.1 compares the fraction of P3HT polarons generated per dopant molecule via ICT (i.e. the *ionization efficiency*) estimated from the analysis of the UV-Vis-NIR absorption spectra and the spin concentration obtained by EPR. For the F_4TCNQ and Mo(tfd-CO_2Me$)_3$-doped rreP3HT samples we find good agreement between the NIR absorption and EPR data when considering that each ICT yields two radicals (the radical anion of the dopant and the P3HT radical cation), whereas for the BCF doped rreP3HT sample, the NIR absorption and EPR data match only when assuming that BCF creates one spin per ICT. This is once again in line with previously reported statements that the BCF anion undergoes further reaction and is absent in the system.[147, 163] More importantly, the excellent agreement between the ionization efficiency values from optical spectroscopy and EPR rules out a significant contribution from *bipolarons* in these systems.

Table 5.1. Fraction of doped P3HT per added dopant molecule estimated from UV-Vis-NIR and cw EPR spectroscopy

Dopant	Doped rreP3HT per dopant molecule		Doped rraP3HT per dopant molecule	
	UV-Vis-NIR, 1:100[#]	EPR, 1:100[§]	EPR, 1:100[§]	EPR, 1:10[§]
F_4TCNQ	0.66	0.54 ± 0.05	0.0044 ± 0.0022	0.0012 ± 0.0003
BCF	0.15	0.12 ± 0.01	0.0023 ± 0.0005	0.0008 ± 0.0001
Mo(tfd-CO_2Me)$_3$	0.35	0.27 ± 0.03	0.0002 ± 0.0002	

[#] Estimated from the UV-Vis-NIR absorption spectra in Figure 5.1

[§] Estimated from the quantitative analysis of the EPR spectra in Figure 5.3 by considering two spins generated per dopant for F_4TCNQ and Mo(tfd-CO_2Me)$_3$, and one spin per dopant for BCF-doped solutions. The reported error estimate corresponds to the standard deviation from individual measurements.

In contrast to the situation in rreP3HT, the corresponding ionization efficiencies of the dopants are orders of magnitude lower in rraP3HT[j], indicating a low concentration of P3HT *polarons* formed by ICT in the latter. This is expected in the case of Mo(tfd-CO_2Me)$_3$-doped rraP3HT as no additional doping-induced features were found, also in the UV-Vis-NIR spectrum. In the case of the F_4TCNQ-doped rraP3HT solutions, the observation of a rather strong NIR absorption (see Figure 5.2a) despite the low ionization efficiency measured by EPR, is consistent with the assignment of the corresponding dominant NIR absorption features to a CTC, which would be

---

[j] In this case we report only ionization efficiency values corresponding to EPR data and not UV-Vis-NIR measurements, due to the lack of extinction coefficient spectra of the doping-induced species observed in rraP3HT. We instead use this opportunity to estimate the extinction coefficient spectra of the species, as discussed in subsequent sections.

EPR-silent. In BCF-doped rraP3HT on the other hand, the low EPR signal strength and ionization efficiency is consistent with the low absorption strength of the NIR feature (see Figure 5.2b) and indicates a low concentration of doping-induced P3HT polarons.

To briefly summarize the important findings up to now, the EPR results in combination with the UV-Vis-NIR results confirm that all three dopants undergo *integer charge transfer* with *regioregular* P3HT in solution, resulting predominantly in P3HT *polarons* and not *bipolarons* (for the doping concentrations considered). In F_4TCNQ-doped *regiorandom* P3HT solutions, we find a very low concentration of unpaired electrons despite the strong NIR absorption, indicating *charge transfer complex* formation in this system. On the other hand, the consistently low NIR absorption as well as spin concentration in BCF-doped rraP3HT suggests *inefficient* charge transfer (doping) in this system. The absence of any additional EPR signals apart from that of the P3HT *polaron* in the BCF-doped rre- and rraP3HT confirms that the BCF anion undergoes further chemical transformation, but at the same time, raises further questions about the reaction mechanism in play.

5.1.3 Additional evidence from FTIR spectroscopy, protonation experiments and ENDOR

FTIR Spectroscopy on F_4TCNQ-doped P3HT solutions

To further validate our assignment of the features in the F_4TCNQ-doped P3HT solutions to ICT polarons and CTCs, we turned to FTIR spectroscopy.

When F_4TCNQ is ionized, the IR bands in the C≡N stretching region undergo a red shift with a magnitude proportional to the degree of charge transfer.[131] The degree of charge transfer(δ) can then be estimated from the equation

$$\delta = \frac{2\Delta v}{v_0}\left[1 - \frac{{v_1}^2}{{v_0}^2}\right]^{-1} \tag{5.2}$$

where v_0 and v_1 denote the vibrational frequency of the neutral molecule and the radical anion respectively, and Δv is the frequency shift from the neutral band to the new position.[180]

Figure 5.4 shows the FTIR spectra[k] of F_4TCNQ-doped rre and rraP3HT in solution (CF). The spectra were recorded (in ambient air) in transmission mode with a Bruker Vertex 70V FTIR spectrometer, at a resolution of 4 cm^{-1} using 256 scans and an aperture size of 1 mm. A liquid transmission cell (*Omni-Cell* system from Specac) with two silicon windows and a 110 µm thick PTFE spacer was used to contain the doped P3HT solutions. A background spectrum of the solvent (*chloroform*), measured under the same conditions was subtracted from all data. The sample preparation procedure (solvent, polymer concentration, doping ratio etc.) was identical to that used for UV-Vis-NIR and EPR spectroscopy, the details of which are given in section 3.2.2.

Neutral F_4TCNQ has a characteristic C≡N stretching band centered at 2227 cm^{-1}.[58, 131] Upon doping with rreP3HT, new peaks emerge, the strongest of which is at ca. 2195 cm^{-1}, as shown in Figure 5.4. This peak is widely assigned to F4TCNQ radical anions and thereby ICT with the polymer.[58, 181] In F_4TCNQ-doped rraP3HT on the other hand, the primary peak is centered at ca. 2210 cm^{-1}. As per equation 5.2, for the doped rraP3HT solutions, δ amounts to 0.53.

This supports the assignment of the UV-Vis-NIR features in Figure 5.2a to CTCs formed via partial charge transfer between F_4TCNQ and rraP3HT.[58, 85] We note that there is also a contribution near 2195 cm^{-1} attributed to an ICT fraction in the F_4TCNQ-rraP3HT solution (particularly for the 1:100 ratio), and a CTC peak in the F_4TCNQ-rreP3HT solution. This implies a coexistence of ICT and CTC states in the doped samples, as reported in the recent work by Neelamraju et al.[39] This finding was interpreted in terms of the broad density of state (DOS) distribution of the highly disordered rraP3HT layer, where only a small fraction of the conjugated neutral segments have a sufficiently low ionization potential (IP) to enable electron transfer to the LUMO of F_4TCNQ.[39] Our rraP3HT has a 50% probability for head-to-tail couplings, which would still allow for a small fraction of sufficiently long head-to-tail coupled segments to undergo ICT. However, since the FTIR spectrum is dominated by the peak centered at 2210 cm^{-1} we believe that the CTC is the dominant species in F4TCNQ-doped rraP3HT. This validates the assignment of the spectral features in the UV-Vis-NIR spectra of F_4TCNQ-rraP3HT shown in Figure 5.2a to CTCs.

---

[k] The FTIR measurements were performed by Dr. Ahmed E. Mansour (Institut für Physik & IRIS Adlershof, *Humboldt-Universität zu Berlin*, Germany).

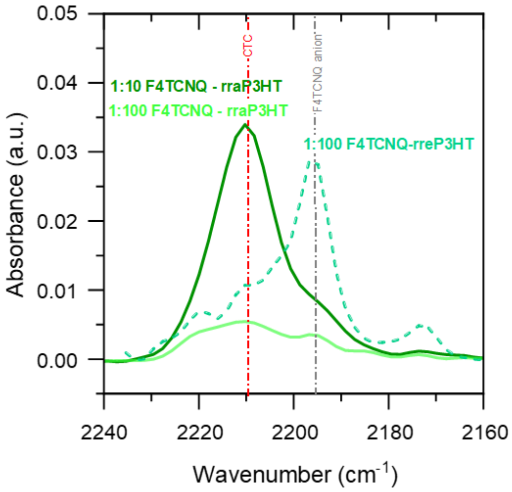

Figure 5.4. FT-IR spectra of F_4TCNQ-doped rreP3HT (1:100 ratio) and rraP3HT (1:10, 1:100 ratio) in chloroform solution, in the C≡N stretching region of F_4TCNQ. The position of ICT (grey) and CTC (red) bands are indicated for reference.

Protonation of P3HT:

As mentioned earlier, Yurash et al. recently proposed a multi-step process for BCF doping of the conjugated polymer PCPDTBT.[163] Initially, BCF reacts with traces of water present in the environment to form BCF·H_2O, which is known to be a strong Brønsted acid that is capable of oxidizing molecules such as ferrocene (which has a similar ionization potential as rreP3HT).[182] This highly acidic BCF·H_2O complex was suggested to oxidize the PCPDTBT polymer via an *endothermic* proton-transfer reaction, resulting in a *positively charged protonated polymer* and a BCF-OH *anion*. [163] Following this, the protonated polymer undergoes an *exothermic* electron-transfer reaction with a nearby *neutral* polymer chain (or segment) to form a *radical cation* (polaron) and a *neutral protonated radical* species.[163] Since the doping reaction was said to involve protonation of the thiophene ring of the polymer subunit, [163] a similar mechanism can be envisioned for BCF doping of P3HT. However, our EPR results of BCF-doped rre- and rraP3HT shown above indicate the presence of only the P3HT radical cation and no other species. This is inconsistent with the proposed BCF doping mechanism as described by Yurash et al.,[163] according to which we should expect a second signal from the neutral protonated P3HT radical.

In order to further investigate the validity of this mechanism for P3HT, we carried out UV-Vis-NIR and EPR experiments on rre- and rraP3HT solutions doped with the Brønsted (protonic) acid dopant bis(trifluoromethanesulfonyl)-imide (HTFSI). HTFSI is typically used as a catalyst in various chemical reactions[183] but has also been used to dope polythiophene derivatives[38, 184], which presumably occurs via pathways involving backbone protonation[38, 185].

Figure 5.5a shows the UV-Vis-NIR spectra of HTFSI-doped (rre- and rra-) P3HT solutions[1] in comparison to those of BCF-doped P3HT solutions. Both HTFSI- and BCF-doped rreP3HT solution spectra are nearly identical with regard to spectral shape, suggesting the formation of a similar species. As per earlier discussions, we assign this to the signature of *delocalized* P3HT *polarons*. The higher absorbance of the HTFSI-doped rreP3HT sample is most likely due to the higher doping concentration in the solution (see footnote). Likewise, the optical spectra of rraP3HT solutions doped with HTFSI or BCF are identical, with features assigned to *localized* P3HT *polarons*. The NIR signal in HTFSI-doped rraP3HT was also influenced by time and illumination (see Appendix Figure A.4). Notably, despite adding similar amounts of HTFSI to both rreP3HT and rraP3HT, the strength of the corresponding NIR signal is more than an order of magnitude higher in rreP3HT than rraP3HT.

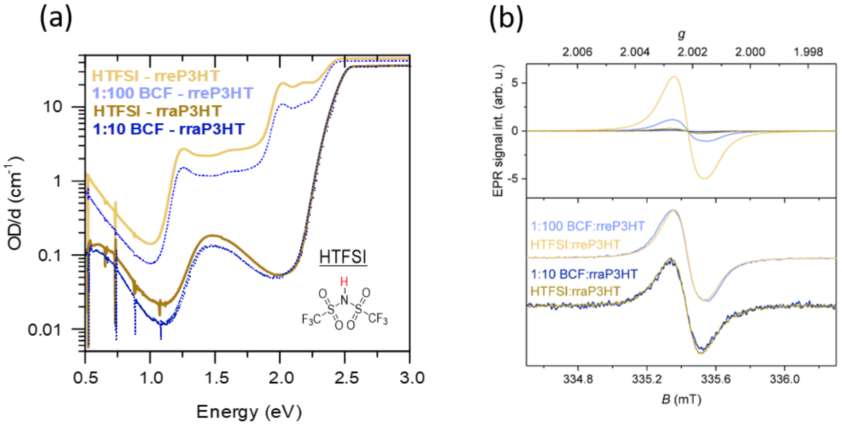

Figure 5.5. (a) Comparison of UV-Vis-NIR absorption spectra of rre- and rraP3HT solutions (in chloroform) doped with BCF and HTFSI (Inset: chemical structure of HTFSI) (b) Comparison of

---

[1] Unlike the BCF-doped P3HT solutions which were prepared according to specific doping ratios (1:100 and 1:10 dopant:host), the HTFSI-doped samples were prepared by directly adding 1-2 crystals of HTFSI to ca. 500 µL P3HT solution in CF to avoid exposure of HTFSI to ambient air for weighing. Therefore, they most likely have a higher, but unknown doping concentration.

X-band room temperature cw EPR spectra recorded on solutions of rreP3HT and rraP3HT doped with BCF or HTFSI. The signal intensities normalized by the Q-factor and modulation amplitude are compared in the top part of the graphs and the normalized spectra are shown in the bottom part for comparison of the spectral shapes.

The EPR results[m] of the HTFSI-doped P3HT solutions are in full agreement with those of optical spectroscopy. We see in Figure 5.5b that HTFSI-doped P3HT solutions (rre- and rra-) show identical EPR spectra to BCF-doped P3HT, with a single signal at $g = 2.0022$ assigned to the P3HT *radical cation*. No additional EPR signals arising from other paramagnetic species such as the neutral radical on the protonated chain are detected. Notably, if a neutral protonated P3HT radical was indeed present, we would expect it to have a different g-value compared to the P3HT radical cation, due to the differences in spin density distribution on the P3HT backbone.

Nevertheless, these findings are consistent with an overall reaction:

$$\text{P3HT} + \text{HA} \rightarrow \text{P3HT}^{\bullet +} + \text{A}^{-} + 0.5\text{H}_2$$

where HA = $BCF \cdot H_2O$ or HTFSI, and A^- is the corresponding anion, similar to what has been suggested for the reaction of ferrocene and $BCF \cdot OH_2$.[182] The reaction might proceed in a similar fashion to that suggested for PCPDTBT,[163] as shown in Figure 5.6, but the absence of additional EPR signals suggests that the neutral protonated radical species most likely undergo further reactions to form spin-less products. This could occur via different channels. For instance, two neutral protonated radicals could react together to eliminate hydrogen and regenerate a neutral closed-shell P3HT. Alternatively, two protonated P3HT cations could react to give two polarons and H_2.

---

[m] Measured and analyzed by Dr. Claudia E. Tait

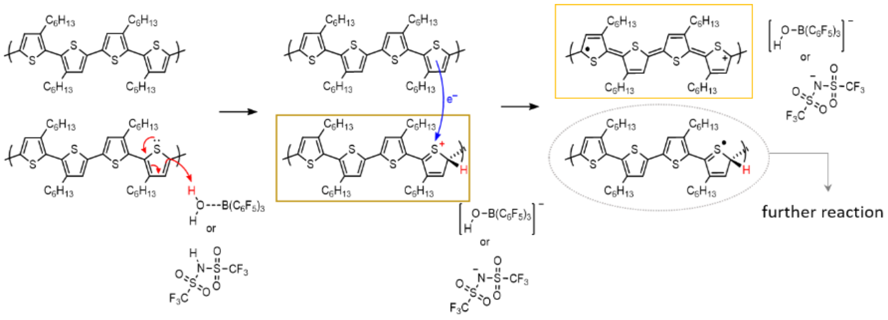

Figure 5.6. Possible reaction mechanism between P3HT units and BCF or HTFSI following references [163, 186], in which the chain is first protonated (brown), leading to the creation of a spin-less protonated polymer cation and a negatively charged BCF:OH^{-} complex. The subsequent electron transfer from a neutral chain or segment results in a P3HT radical cation (orange) and a neutral protonated radical (grey).

In agreement with the UV-Vis-NIR results, the spin count in HTFSI-doped rreP3HT was found to be nearly two orders of magnitude higher[n] than that in HTFSI-doped rraP3HT, suggesting *inefficient charge transfer* of the dopant with rraP3HT. Importantly, these results suggest that both BCF as well as HTFSI dope P3HT via similar pathways.

Degree of charge delocalization from ENDOR spectroscopy

A recurring observation in the experiments discussed till now is that all the dopants undergo *efficient* ICT with rreP3HT to form P3HT polarons, whereas the ionization efficiency in rraP3HT is very poor. The optical spectra of the doped rreP3HT solutions in chloroform (with the red-shifted P_1 transition and the strong aggregate absorption at 2 eV, as shown in Figure 5.1), are reminiscent of the spectra of highly *delocalized P3HT polarons*.[118] It has been previously suggested that the doping mechanism as well as the charge transfer efficiency in a dopant:host system is determined by the ability of the host to form ordered aggregates and thereby delocalize the charge.[113, 155] Currently, however, there is only limited direct experimental evidence pertaining to the role of charge delocalization on the mechanism of doping. [25, 187] To address this open question, we

---

[n] Spin concentration in 25 µL of HTFSI-doped rreP3HT was $8.7 \pm 0.1 \times 10^{14}$ whereas $1.6 \pm 0.5 \times 10^{13}$ in doped rraP3HT

employed electron nuclear double resonance (ENDOR) spectroscopy on our doped P3HT solutions.

In a paramagnetic sample held in a magnetic field, in addition to the *electron Zeeman splitting* and *nuclear Zeeman splitting* of energy levels[o], a further shift of the energy levels is caused by the interaction of the electron spin with the nuclear spin. In the case of an electron spin coupled to a hydrogen ^{1}H (I=1/2) nucleus and placed in an external magnetic field, a splitting into four energy levels results, which can be selectively probed by initiating EPR or NMR transitions (see Figure 5.7). Importantly, the energy differences (ν_{EPR} and ν_{NMR}) depend on the *strength of the coupling* between the magnetic nuclei and the electron. The ENDOR experiment probes the NMR transitions through changes in the intensity of the EPR transitions. For a coupled S=1/2, I=1/2 system, this results in two spectral lines at frequencies ν_{NMR1} and ν_{NMR2}, which are centered at the nuclear Larmor frequency (ν_n), resulting from the nuclear Zeeman interaction and split by the hyperfine coupling (a), as shown in Figure 5.7. Therefore, the stronger the interaction between the electron and nucleus, the larger the hyperfine splitting between the lines and the broader the ENDOR spectrum. Hence, a narrow ENDOR spectrum will imply a more delocalized charge, whereas a broad ENDOR spectrum will indicate a more localized charge in the system. ENDOR spectroscopy has been successfully used in the past to study the extent of polaron delocalization on the conjugated polymer backbone.[174, 188-189]

---

[o] Electron Zeeman splitting is caused by the interaction of the electron with the magnetic field and the *nuclear Zeeman splitting* is caused by the interaction of the *nuclear spin* with the magnetic field

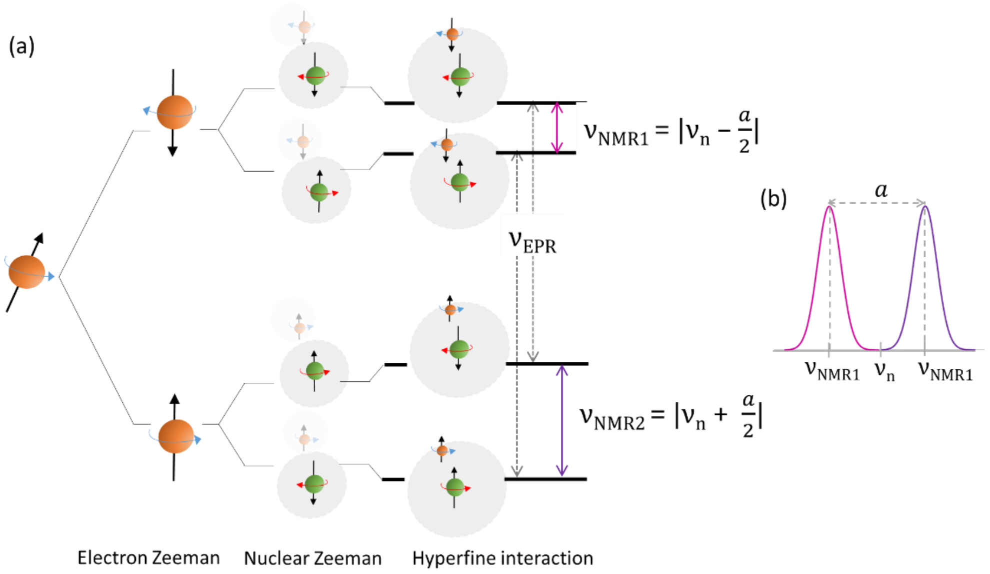

Figure 5.7. Schematic illustrations of a) the energy levels for a coupled electron (S = ½) and nucleus (I = ½) under an externally applied magnetic field resulting from electron Zeeman, nuclear Zeeman and hyperfine interactions b) an ENDOR spectrum with the hyperfine coupling constant (a) and the nuclear Larmor frequency (ν_n).

Figure 5.8 shows the spectra of Q-band ^{1}H Davies ENDOR measurements[p] performed on flash-frozen[q] solutions of doped rre- and rraP3HT in chloroform. We used identical sample preparation conditions as before, to enable a direct comparison of the optical and ENDOR results. Detailed information about the measurement parameters and ENDOR analysis can be found in our publication.[146]

The ENDOR spectrum in the doped P3HT samples arises mainly from the interaction between the α-protons on the thiophene rings and the electron spin density on the adjacent carbon atom. Since the spin density is distributed over multiple thiophene rings, several protons with different hyperfine coupling strengths contribute to the ENDOR spectrum without clear features that could be assigned to individual protons. Regardless, the width of the spectrum is still determined by the largest proton hyperfine coupling and scales with the number of thiophene rings over which the electron is delocalized.[174, 188-189]

---

[p] The ENDOR measurements and data analysis was done by Dr. Claudia E. Tait

[q] Low measurement temperatures are required to 1) obtain reduced relaxation times enabling the ENDOR experiment with higher signal intensity and 2) prevent averaging of anisotropic interactions due to tumbling in a liquid medium.

In frozen rreP3HT solution, the overall width of the ENDOR spectrum was found to be identical irrespective of the size or type of dopant used, as seen in Figure 5.8a. This not only implies a similar extent of charge delocalization and environment in all four doped rreP3HT systems, but also supports our postulation that the neutral protonated radical species in BCF/HTFSI-doped P3HT solutions most likely undergoes further reaction as it would otherwise also contribute to the ENDOR spectrum. We would expect such a species to be characterized by a reduced extent of spin delocalization and therefore by a broader ENDOR spectrum. The differences in the central region of the ENDOR spectrum of each system most likely stem from weak interactions to distant protons as well as contributions from the dopant anion.

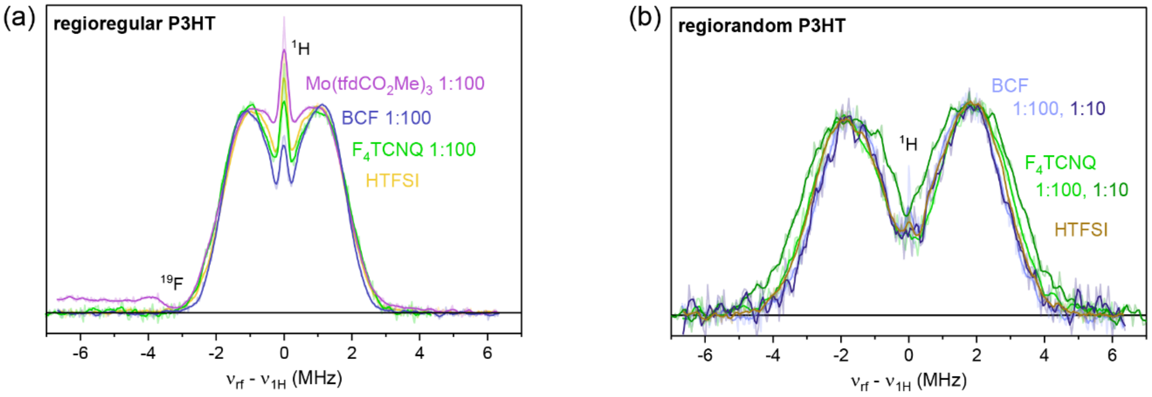

Figure 5.8. Q-band ^{1}H Davies ENDOR spectra recorded on frozen chloroform solutions of rreP3HT (a) and rraP3HT (b) doped with F$_4$TCNQ, BCF, HTFSI or Mo(tfd-CO$_2$Me)$_3$ at doping ratios of 1:100 (and 1:10 for rraP3HT) at a temperature of 10 K. The ENDOR spectra were recorded at the maximum of the EPR signal of the P3HT radical cation, at a magnetic field around 1213.5 mT (see our publication[146] for additional experimental details). The lower signal-to-noise ratio for the spectra in b) is due to the significantly smaller number of spin-carrying moieties in doped rraP3HT solutions.

In contrast, Figure 5.8b shows the noticeably broader ENDOR spectra of frozen solutions of doped rraP3HT, indicating that the polaron is more localized in these samples. Moreover, the signal intensity is considerably weaker in these samples. It is, however, important to keep in mind that the signals measured via ENDOR only correspond to the fraction of the sample that have undergone ICT (and are therefore paramagnetic in nature), and even amongst that, only the species whose spins do not decay very fast[r]. Nevertheless, these results suggest that the concentration of ICT polarons in these systems is significantly lower compared to rreP3HT, in accordance with our previous cwEPR and optical spectroscopy experiments. Further analysis of the ENDOR spectra as per the procedure described by Aguirre et al. [174] revealed that in our doped rreP3HT solutions, the polaron is delocalized over ca. 12 thiophene rings, in accordance to what they observed for I_2-doped rreP3HT. On the other hand, analysis of the spectra of the doped rraP3HT solutions indicates that the polaron is restricted to ca. 6 thiophene rings in this case. A detailed discussion of the ENDOR results and analysis procedure is outside the scope of this thesis, but can be found in our joint publication[146].

In general, the results from ENDOR spectroscopy are in close agreement with our findings from optical spectroscopy. Mainly, these results justify the assignment of the spectral features observed in doped rreP3HT solutions to *delocalized polarons*, and the ICT features observed in BCF- or HTFSI-doped rraP3HT to *localized polarons*. This once again supports the hypothesis that the ICT mechanism prevails in systems which are able to form ordered structures and hence delocalize the charge, whereas inefficient charge transfer processes occur in more disordered systems such as oligomers and amorphous conjugated polymers.

In summary, the results presented in this section have corroborated several findings from the previous two sections. FTIR spectroscopy showed that F_4TCNQ-doped rraP3HT solutions predominantly consist of CTCs, thereby confirming the assignment of the UV-Vis-NIR features in the corresponding solutions to a CTC. The protonic acid dopant HTFSI was found to dope P3HT in a similar fashion as BCF, forming delocalized polarons in rreP3HT and localized polarons in rraP3HT. ENDOR results showed that the polaron is indeed more *delocalized* in doped rreP3HT than rraP3HT.

With these additional insights, we sought to (re)calculate the molar extinction coefficient spectra of the doping-induced species observed in our P3HT solutions, as shown in the next section.

---

[r] The ENDOR measurements were carried out in pulse-mode and not continuous-wave mode. Paramagnetic species that relax within the duration of the pulse sequence (ca. 25 µs for Davies ENDOR) do not contribute to the observed ENDOR spectrum.

5.1.4 Estimating the molar extinction coefficient of the doping-induced species

Previously reported values of the molar extinction coefficient spectrum of the P3HT polaron are likely prone to some degree of error, since they were estimated indirectly, by fitting optical spectra to a reference based on the molar extinction coefficient of F_4TCNQ [36, 49] (see Appendix A section 2). Recalling that by quantitative analysis of EPR data we obtain the actual concentration of charged P3HT in the doped solutions, we recalculated the molar extinction coefficient of the doping-induced P3HT polarons by now considering the concentration of P3HT spins measured in the doped solutions. In the process, we also sought to distinguish the different species that contribute to the optical spectra of doped P3HT solutions. From previous discussions, we know that they can be one or more of the following: localized polaron, delocalized polaron, bipolaron or CTC.

Regioregular P3HT

Figure 5.9a shows the estimated molar extinction spectrum of P3HT polarons on aggregated chains, which was obtained by dividing the optical spectra of doped rreP3HT solutions by the molar concentration of P3HT spins in the solutions. The close agreement of the three spectra in Figure 5.9a and the EPR results in Table 5.1 suggests that all three dopants (F_4TCNQ, BCF and Mo(tfd-CO_2Me$)_3$) induce the very same *polaronic* species. In particular, the fact that the shape, peak position, as well as the oscillator strengths in the optical spectra align closely, rules out to a large degree the contribution of other doping-induced species to the NIR absorption of the doped rreP3HT herein.

Since a contribution from CTCs to the spectra in Figure 5.9a can be neglected, we turn to the case of *localized* polarons. Mansour et al. have recently shown that solutions of BCF-doped rreP3HT contain some amount of polarons on non-aggregated chains (i.e. *localized* polarons), depending on the doping ratio as well as the absolute polymer concentration of the sample.[173] Drawing from their discussion, our 1:100 ratio BCF-doped rreP3HT solution with an absolute P3HT concentration of 2 mg mL^{-1} most likely contains only a small fraction of localized polarons. Besides, in our experiments we do not find Mo(tfd-CO_2Me$)_3$ to induce any such localized polarons, as seen from the lack of charge transfer with rraP3HT (see Figure A.1) and in temperature-dependent experiments (*vide infra*). Therefore, the overall contribution of localized polarons to the molar extinction spectra of doped rreP3HT shown in Figure 5.9a must be very small.

Next we consider the case for *bipolarons* contributing to the optical spectra. As per spectroelectrochemistry results reported in the literature, bipolarons on P3HT are expected to exhibit a very different shape i.e. a broad spectrum with strong absorption even at lower energies (no "dip" around 1 eV as seen below), and a peak at ca. 0.7 eV.[190-191] Such a contribution is inconsistent with the distinct shape of the optical absorption spectra in Figure 5.9a. Therefore, we assign the NIR optical absorption of our doped rreP3HT samples in CF entirely to *delocalized polarons* on P3HT aggregates.

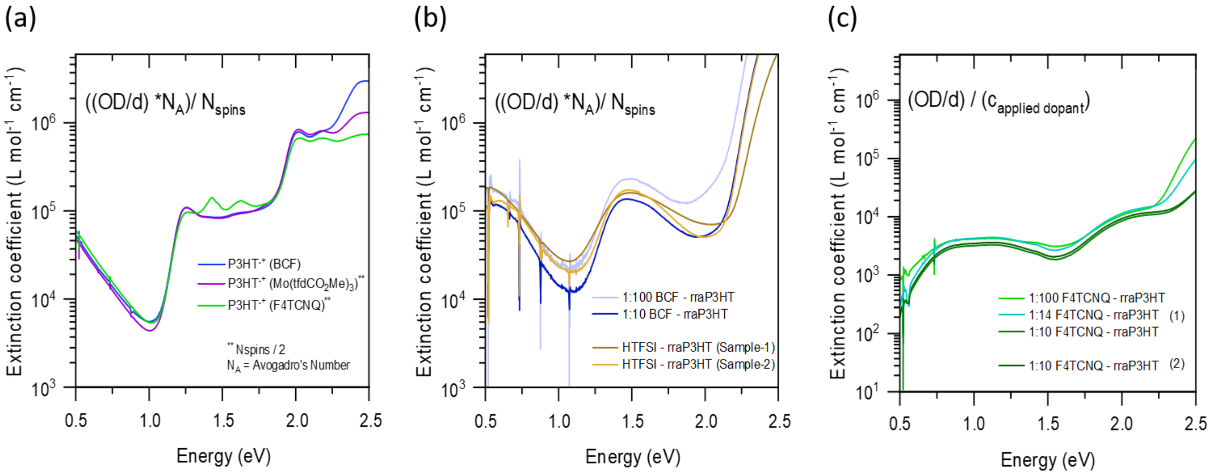

Figure 5.9. The molar extinction coefficient of a polaron on a) rreP3HT and b) rraP3HT, determined using the concentration of spins of charged P3HT (see Appendix Table A.1 for values) obtained from EPR spectroscopy. Shown in c) is the molar extinction spectrum of the CTC formed between F_4TCNQ and rraP3HT, estimated from the optical absorption spectra of different sets of data with the assumption that every added dopant molecule forms a complex (Note the different y-scale in (c)). In all three graphs, the absorption beyond 1.7 eV becomes dominated by neutral, aggregated and non-aggregated P3HT chains, which will contribute differently to the spectra depending on the polymer concentration and the degree of aggregation.

Regiorandom P3HT

Similarly, to estimate the molar extinction spectrum of the doping-induced species in BCF- and HTFSI-doped rraP3HT solutions shown in Figure 5.9b, we divided the optical spectra by the corresponding molar concentration of P3HT spins[s] in the doped solutions. Notably, the calculated molar extinction coefficient spectrum of the spin-carrying moiety exhibits a reasonably high absorption strength, comparable to that of the doped rreP3HT samples (see Figure 6b), further supporting the assignment of the feature to that of a *localized polaron* on rraP3HT. The differences in the strength and shape of the spectra of the different samples may on the one hand be due to the low absolute absorbance of the doped rraP3HT solutions (especially the 1:100 BCF-rreP3HT) which causes an uncertainty in the background correction. Alternatively, they could also stem from differences in chain conformation/interactions depending on the doping concentration and nature of the doping-induced species. Importantly, our experiments showed some evidence for the coexistence of spin-less doping-induced species in BCF/HTFSI-doped rraP3HT solutions. For example, although the doping-induced NIR signal of these solutions increased upon *light soaking*, we did not see an equivalent increase in the EPR signal (see Appendix Figure A.5). In order to ascertain that the (also spin-less) protonated P3HT cation which is an intermediate product in the doping reaction (see Figure 5.6) does not contribute significantly to the molar extinction spectrum in Figure 5.9b, we turned to DFT.

Time-dependent DFT (TDDFT) calculations[t] on (protonated) 4T doped by BCF in solution show that the main effect of protonation is to either distort the molecular backbone of the host or to break the conjugation, depending on the protonation site (see Appendix A section 7). This typically results in the segregation of the frontier orbitals and consequently, to a splitting of the first absorption peak into two excitations at (slightly) lower and higher energies with respect to the absorption onset of the neutral species. Importantly, we found no evidence of strong sub-band gap absorption (comparable to that in Figure 5.9b) in any of the considered scenarios (in protonated 4T or 10T) from the TDDFT calculations (see Table A.2). Therefore, we can be quite certain that the protonated chains do not contribute strongly to the sub-bandgap feature observed in Figure 5.9b.

Finally, we estimated the molar extinction coefficient of CTCs in F_4TCNQ-doped rraP3HT, shown in Figure 5.9c. Since EPR does not provide any information about this spin-less species, we

---

[s] On the assumption that each polymer polaron leads to the formation of one spin, based on the EPR, UV-Vis results in sections 5.1.2, 5.1.3 and DFT results (vide infra)

[t] The TDDFT calculations and data interpretation was done by Dr. Michele Guerrini (Humboldt-Universität zu Berlin)

proceeded by assuming that all the applied dopants form CTCs, based on the FTIR results. The spectra coincide well, indicating that this is a fairly reasonable assumption.

5.2 Revealing the underlying mechanism of doping: the role of structural order

The molar extinction spectrum of the polaron on rreP3HT shown above highlights an unexpected result. As seen in Figure 5.9a, the NIR absorption is identical for all three solutions, despite our results hinting at the presence/occurrence of different interactions between the dopants and the polymer/solvent. For example, the EPR measurements indicate an *exchange interaction* between the rreP3HT polaron and the F_4TCNQ anion, but not for the other two dopants. Aside from that, the lack of a second spin-carrying species in our BCF-doped solution suggests that the formed radical anion product undergoes further reaction in accordance with previous work.[147] Still, the NIR region of the solution spectra appears to be unaffected by these processes.

This is in contrast to the typical situation in *solid-state* doped rreP3HT films, which often reveal differences not only in the exact shape of the P_2 double peak feature, but also in the position of the P_1 transition, depending on the doping concentration and conditions.[192] Given the absence of these effects in our solution studies, our data suggests that the *exact nature and the optical absorption of the doping-induced polarons on rreP3HT in the solid state is influenced by mechanical strain and the unavoidable heterogeneity of the solid films*. The presence of a solvent on the other hand, will allow the doping-induced aggregates to relieve any mechanical stress and adopt a thermodynamically stable conformation, which then enables the formed polarons to delocalize along, and possibly among, the neighboring polymer backbones.

In rraP3HT solutions on the other hand, the choice of the dopant is found to greatly influence the type of species formed (and consequently, the optical spectrum). For instance, the planar F_4TCNQ molecule predominantly forms a CTC with the polymer, whereas BCF and HFTSI-doping of rraP3HT results in the formation of a low concentration of P3HT polarons which are more localized compared to those in aggregated rreP3HT. The bulky $Mo(tfd\text{-}CO_2Me)_3$, is consistently found to not dope rraP3HT, presumably due to the energetic mismatch ($IE_{rraP3HT} \approx 5.25$ eV, $EA_{Mo(tfd\text{-}CO2Me)3} \approx 5.0$ eV)[51, 149]. Notably, the absence of a peak at 2 eV (assigned to doping-induced chain aggregation[40, 173]) in all of the doped rraP3HT solutions shows that the rraP3HT chains are unable to planarize and form aggregates.

From the discussion above, it is evident that rreP3HT and rraP3HT represent extreme cases. This raises the following questions:

1) Can the type of doping-induced species formed be changed by changing the environment of the polymer?
2) Will the species (localized polaron, delocalized polaron, CTC) transform from one to another when the degree of chain aggregation is deliberately modified in the system?
3) Are the species formed in rraP3HT a necessary precursor to those observed/formed in rreP3HT? (Since prior to doping, rreP3HT chains in solution are also in the twisted (non-aggregated) conformation like the chains in rraP3HT.)
4) The low doping efficiency in rraP3HT is often attributed to the inability of the rraP3HT chain to planarize/aggregate and thereby delocalize the polaron.[113] This suggests that *a high concentration of polarons cannot be efficiently formed on individual, non-aggregated chains*. Can we further verify/justify this hypothesis?

One simple way to investigate the theories stated above would be with temperature-dependent measurements on doped solutions. On the one hand, increasing the temperature can improve the solubility of the compounds due to entropic effects; on the other hand, the additional thermal energy can induce a larger twist of the backbone, thereby reducing the effective conjugation length of the polymer chain. Duong et al. and Wang et al. have successfully demonstrated the use of temperature to control the dopant-polymer interaction in solution as well as films.[119, 136]

5.2.1 Insights from heating and cooling BCF-doped rreP3HT

Figure 5.10 shows the temperature dependent UV-Vis-NIR spectra of a 1:100 BCF-doped rreP3HT solution. For this study, chlorobenzene was used as the solvent since it has a higher boiling point (~ 130 °C) compared to chloroform (~ 62 °C), which allows for a larger measurement range. The cuvette was maintained at the specific temperature for ca. 10 minutes (in order for the solution to equilibrate) before each measurement.

As expected, the spectrum at room temperature (25 °C) in Figure 5.10a is dominated by the characteristic optical signature of *delocalized polarons* on aggregated P3HT chains, as in Figure 5.9a. However, with a gradual increase in the solution temperature, the neutral P3HT aggregate signal at ca. 2 eV decreases, and the broad double peak (P_2) signal between 1.25 eV and 1.75 eV transforms into a single broad peak at ca. 1.5 eV. Finally, the spectrum at 100°C (seen clearly in Figure 5.10b) is characterized by a blue-shifted absorption minimum at ca. 1.1 eV, and a broad peak at 1.5 eV, which is identical to the optical signature of the *localized polaron* shown in Figure 5.9b.

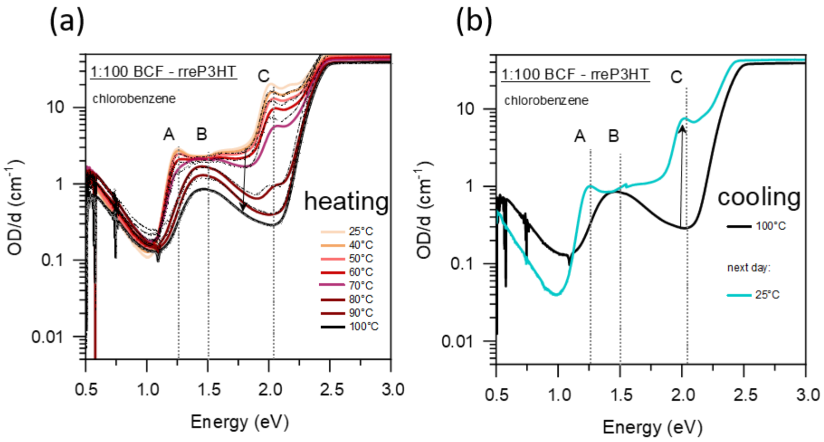

Figure 5.10. Temperature-dependent UV-Vis-NIR solution spectra of 1:100 BCF-doped rreP3HT (in chlorobenzene), showing the heating cycle (a) and the final spectrum after cooling back to room temperature (b). The vertical dotted lines indicate the characteristic peak positions of the delocalized polaron (A), the localized polaron (B) and the P3HT aggregate (C). The dashed-grey spectra in (a) correspond to the spectra reconstructed by the weighted summation of the delocalized P3HT polaron spectrum and the localized P3HT polaron spectrum (see the main text for details). Select individual graphs are shown in Appendix Figure A.7.

Based on previous studies,[119, 136] the characteristic changes in the optical spectra of doped P3HT upon heating have been interpreted in terms of a temperature-induced de-aggregation of the P3HT chains. The optical spectra of the BCF-doped rreP3HT solution at 25 °C and 100 °C are reminiscent of the two extreme cases of delocalized P3HT polarons and localized P3HT polarons, respectively. This raises the question as to whether the optical spectra at the *intermediate temperatures* can be reconstructed as linear combinations of the respective molar extinction coefficient spectra shown in Figure 5.9.

Indeed, the dotted lines in Figure 5.10 are the weighted summation of the delocalized P3HT polaron spectrum and the localized P3HT polaron spectrum (see Appendix Figure A.7 for select individual graphs). The fit parameters are given in Table 5.2. As expected, an increase in temperature leads to an increase in the contribution from the *localized polarons* on isolated chains at the expense of the *delocalized polarons* on aggregated chains. This implies a coexistence of polarons on aggregated and individual chains (depending on the temperature of the solution), with no evidence of any other species.

Table 5.2. The fit parameters for the reconstructed temperature dependent BCF-rreP3HT spectra (shown in Figure 5.10 (dotted lines)), relative to the polaron concentration of the solution at 25 °C (which is ca. 22 % of the initial BCF concentration)

Solution Temperature	Aggregated fraction (%)	Isolated fraction (%)
25°C	100	0
40°C	88	5
50°C	80	10
60°C	60	14
70°C	35	25
80°C	2	35
90°C	0	26
100°C	0	18

Upon cooling the solution from 100 °C, the original absorption peaks (corresponding to polarons on aggregated chains) are regained slowly, but the process is not entirely reversible. This is consistent with the notion of an irreversible reaction of the formed dopant species.

Next, we consider the situation in F_4TCNQ-doped rreP3HT solutions.

5.2.2 Insights from heating and cooling F_4TCNQ-doped rreP3HT

Figure 5.11 shows the temperature dependent optical spectra of a 1:100 F_4TCNQ-doped rreP3HT solution, in *chloroform*. Similar to the observation in BCF-doped rreP3HT solutions, the F_4TCNQ doped solution undergoes a rapid de-doping upon heating, as evident from the loss in the combined signal of the P3HT polaron on aggregated chains and the F_4TCNQ anion signal. Cooling the solution back to room temperature restores the original spectrum, showing that doping and de-doping of P3HT with F_4TCNQ is reversible to a large extent,[25] in contrast to the case of BCF-doping as discussed above. On the other hand, the same system (F_4TCNQ-doped rreP3HT) behaves quite differently in *chlorobenzene*, as discussed below.

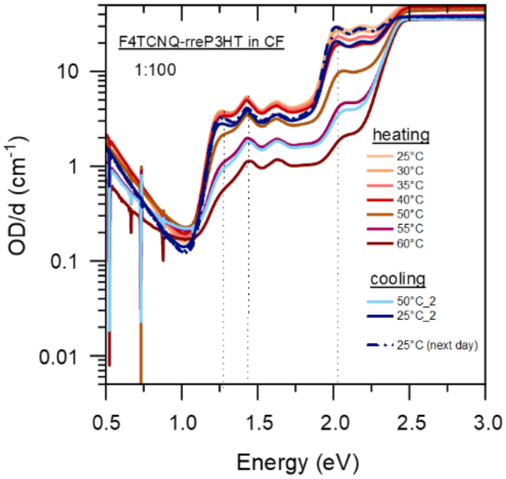

Figure 5.11. Temperature dependent UV-Vis-NIR solution spectra of 1:100 F_4TCNQ doped rreP3HT, in chloroform.

Before we proceed with discussion of the temperature dependent data, let us first compare the room temperature absorption spectra of F_4TCNQ-doped rreP3HT in the two solvents, shown in Figure 5.12. Note that both solutions are identical with respect to the doping level (1:100 dopant:3HT) and the final P3HT concentration (= 2 mg mL^{-1}). Compared to chloroform, the solution in *chlorobenzene* exhibits no features attributed to P3HT aggregates (e.g. peak at ca. 2 eV), but instead shows only a single broad P_2 peak at ca. 1.6 eV (superimposed on the F_4TCNQ anion peaks), and a blue-shifted P_1 transition (at ca. 0.6 eV). Wang et al. report similar absorption spectra for F_4TCNQ-doped rreP3HT solutions in chlorobenzene, [119] and assign the corresponding NIR features to that of a *bipolaron* on P3HT chains, based on older studies[193-194]. However, the assignments were made for samples with much higher doping levels (ca. 1:10 in [119]), in which case the presence of *bipolarons* cannot be entirely excluded. On the other hand, we do not expect our 1:100 dopant-polymer ratio solution to contain a significant amount of bipolarons, if at all.

In fact, the NIR region of the room temperature optical spectrum in *chlorobenzene* can be reconstructed by considering that ca. 3 % of the added F_4TCNQ dopants form *delocalized P3HT polarons* and ca. 23 % of the added dopants lead to *localized P3HT polarons*. This agrees very well with quantitative EPR measurements which indicate that in *chlorobenzene*, ca. 20±1 % of the employed F_4TCNQ induce polarons on P3HT chains (see Appendix Figure A.9). Therefore, the F_4TCNQ-doped rreP3HT solution appears to be dominated by *localized polarons* on isolated chains in *chlorobenzene*, whereas the same system in *chloroform* consists primarily of *delocalized polarons* on aggregated P3HT chains.

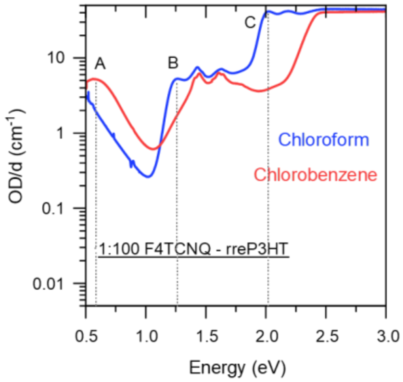

Figure 5.12. Comparison of the UV-Vis-NIR absorption spectra of 1:100 F_4TCNQ-doped rreP3HT solution in chloroform (blue) vs. chlorobenzene (red).

Müller et al. have previously investigated the difference in the optoelectronic properties of F_4TCNQ-doped rreP3HT solutions in chloroform and chlorobenzene.[59] Notably, they report a higher degree of aggregation (and hence stronger doping) in a *chlorobenzene*-based solution than in a *chloroform*-based solution, as per UV-Vis-NIR measurements.[59]As mentioned in section 4.3, they attributed this to the difference in the polarity of the two solvents. However, their results are in direct contradiction to our observation for this system, since our UV-Vis-NIR spectra shown in Figure 5.12 clearly demonstrate a stronger peak at 2 eV (attributed to P3HT aggregates) in *chloroform* than in *chlorobenzene*. A closer look at the experimental conditions of the other work,[59] offers a possible explanation for this discrepancy. Apart from the difference in the final polymer concentration (2 mg mL^{-1} in our case vs. 0.012 mg mL^{-1} in ref [59]) which is also deemed to affect dopant-polymer interactions and the degree of aggregation,[173] the UV-Vis-NIR measurements by

Müller et al. were performed on doped solutions maintained at 50 °C. Previous studies [85, 119, 136] as well as the results presented herein demonstrate that the temperature of the solution significantly influences the degree of aggregation, the type, and concentration of dopant-induced species. Hence, we believe that at room temperature and intermediate polymer concentrations of 2 mg mL^{-1}, F_4TCNQ-doped rreP3HT chains are more solvated in *chlorobenzene* than in *chloroform*. (We note, however, that the *solvent polarity* also plays a role on the degree of dopant-host interaction,[59] as discussed in section 4.3 for BCF-doped rreP3HT solutions.)

Returning now to the influence of temperature on the doped solutions, Figure 5.13 shows the results of the temperature dependent measurements on 1:100 ratio F_4TCNQ-doped rreP3HT solution in *chlorobenzene*. The optical spectra are plotted in Figure 5.13a whereas the evolution in spin count determined by EPR spectroscopy (normalized to the value at room temperature) is shown in Figure 5.13b. Care was taken to maintain similar experimental conditions (polymer concentrations, duration of heating, etc.) during both the measurements. Figure 5.13a reveals several differences compared to the behavior in chloroform. First, we see that upon heating, the shape of the absorption signal remains unchanged until ca. 60 °C. Besides, the signal strength does not decrease substantially until ca. 60 °C. However, a further increase in the temperature to 70 °C causes a sudden decrease in the signal strength (while still not drastically affecting the shape of the spectrum). Heating beyond 70 °C to 80 °C and above is, however, clearly detrimental for the dopant-host interaction, as we are left with a broad and nearly featureless sub-band gap signal.

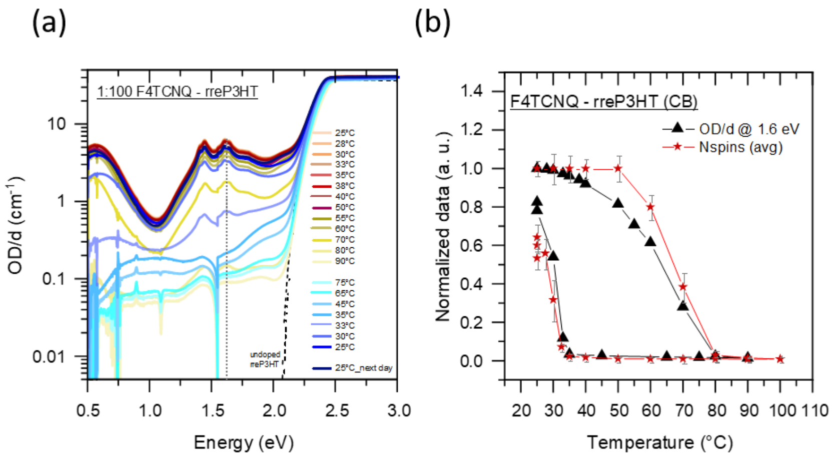

Figure 5.13. Temperature dependent UV-Vis-NIR solution spectra (a) of 1:100 F_4TCNQ-doped rreP3HT, in chlorobenzene (b) Evolution of the F_4TCNQ anion absorption peak at 1.6 eV and the

average spin count in the solution (from EPR experiments) with temperature. The data have been normalized to the corresponding value at 25°C before the heating cycle.

Cooling the solution back to room temperature restores the initial spectrum, indicating that the doping and de-doping process in this system is reversible. Remarkably, the characteristic CTC absorption signature is discerned in the 35 °C - 45 °C range, but only in the cooling cycle. Analysis of the NIR region of these spectra (see Appendix A section 10) reveals that, in this temperature range, the doped solution predominantly consists of CTCs, with up to ~ 40 % of the added dopants forming CTCs. At even lower temperatures (< 35°C), this signal is superimposed by the absorption signal from *localized polarons* and is accompanied by a progressive reduction in the CTC contribution. This is seen nicely in Table A.3.

A closer look at the evolution of the absorption peak (e.g. at 1.6 eV) with temperature, shown in Figure 5.13b indicates that the 1:100 F_4TCNQ-doped rreP3HT system exhibits a pronounced *hysteresis* in chlorobenzene. From Figure 5.13a we see that although the absorption signal from the *localized polaron* is stable up to ca. 60°C in the heating cycle, the corresponding features are regained only at ca. 30 °C in the cooling cycle. This correlates well with the EPR measurements which shows that the spin concentration in the doped solution follows a similar *hysteresis* behavior with temperature, as seen in Figure 5.13b. Considering that the recovery of the localized polaron signal follows the appearance of the CTC, we speculate that the CTC is indeed the precursor to localized polarons in F_4TCNQ doped rreP3HT.

5.2.3 Insights from heating and cooling Mo(tfd-CO_2Me)$_3$-doped rreP3HT

Finally, we consider the situation in Mo(tfd-CO_2Me)$_3$-doped rreP3HT. Figure 5.14 shows the temperature dependent UV-Vis-NIR spectra of 1:100 ratio Mo(tfd-CO_2Me)$_3$-doped rreP3HT solution in chloroform. Similar to the other experiments, the final polymer concentration is 2 mg mL^{-1} and the doped solution was heated for ca. 10 minutes at each temperature before the measurement.

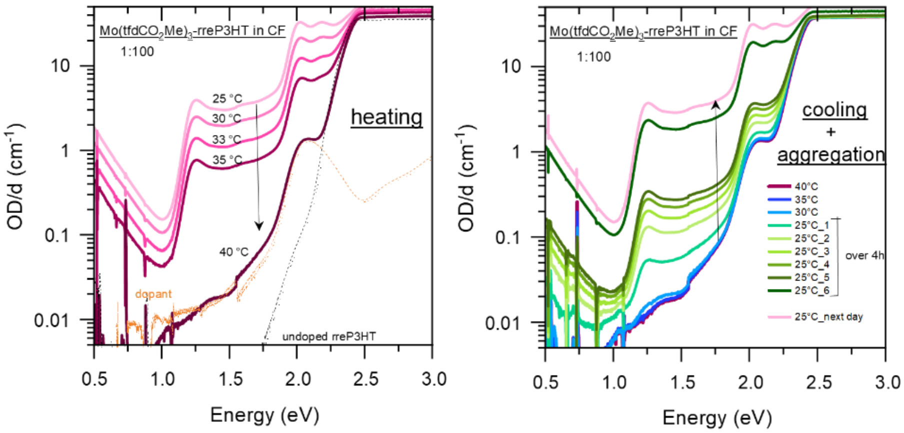

Figure 5.14. Temperature dependent UV-Vis-NIR solution spectra of 1:100 Mo(tfd-$CO_2Me)_3$-doped rreP3HT, in chloroform. Note that Mo(tfd-$CO_2Me)_3$ barely dopes rreP3HT in CB.

As per previous discussions, the NIR absorption signal is attributed to that of the *delocalized polaron* on aggregated P3HT chains. Upon heating, the strength of this signal reduces rapidly, with no apparent change in the *shape* of the features to indicate a change in the nature of the species. Already at 40 °C, the spectrum displays only the absorption features of the neutral dopant superimposed on the undoped rreP3HT spectrum, implying complete de-doping. Notably, although the de-doping process is rapid (within 10 minutes of heating at each temperature), in the cooling cycle, the polaron signal recovers slowly over a few hours despite cooling to 25 °C. This is in agreement with the slow initial charge transfer (doping) process that we typically observe in this system, as mentioned in section 5.1. Nevertheless, the original signal is recovered completely by the next day, indicating that the doping and de-doping process is reversible for this system.

The slow recovery of the polaron signal is in line with the hypothesis of an energetic/kinetic barrier to polaron formation in Mo(tfd-$CO_2Me)_3$-doped rreP3HT solutions. This is further supported by the fact that we did not observe significant NIR absorption signal to indicate doping in Mo(tfd-$CO_2Me)_3$-doped rreP3HT solution in *chlorobenzene*.

5.3 Conclusion

In this chapter, the optical signatures and doping mechanism in p-doped P3HT in solution were comprehensively studied with the aim of elucidating 1) the actual nature of the doping-induced species observed via optical spectroscopy and 2) the factors influencing the doping mechanism and ionization efficiency in a dopant:host system. This was accomplished by employing high resolution UV-Vis-NIR, FTIR and EPR spectroscopy on rreP3HT and rraP3HT solutions doped with three different dopants: F_4TCNQ, BCF and Mo(tfd-CO_2Me)$_3$ that vary in shape/size and doping mechanism. This allowed us to unambiguously identify three distinct optical signatures of P3HT, assigned to delocalized polarons (formed via ICT), localized/isolated P3HT polarons (via ICT), and charge-transfer complexes, and estimate their molar extinction coefficient values. Notably, we found that all three dopants consistently form the same predominant species (i.e. delocalized polarons) in rreP3HT solution at room temperature, where the polymer chains are free to aggregate. However, when the ability of the polymer chains to aggregate is suppressed, either due to steric effects (as in rraP3HT), or by heating of the polymer solution, the polymer-dopant interactions become more critical, leading to reduced doping (ionization) efficiency, and/or CTC formation. Using ENDOR spectroscopy, we were able to provide direct experimental evidence of higher charge delocalization in doped rreP3HT compared to doped rraP3HT, thereby demonstrating that the local morphology in the polymer chain has a stronger influence on the doping mechanism than the shape or size of the dopant molecule.

6. Doped Polymer Films: Correlating the Morphology and Charge Transport

In the previous two chapters we looked at the various parameters influencing the charge transfer mechanism and efficiency in doped polymeric solutions. This was important in order to isolate the interactions between the dopant molecules and the polymer chains, and exclude the influence of the morphological changes (e.g. aggregation or crystallization) occurring between the polymer chains during film formation. However, the ultimate goal in this field is to realize controlled, efficient doping of polymeric films that can then be implemented in devices. This requires a thorough understanding of not only the fundamental dopant-host interactions [83], but also the influence of crystallinity and morphology[25] on the optoelectronic properties of the doped film.

As stated previously, I first investigated the BCF:rreP3HT system during my master thesis work[48], wherein we conducted preliminary optical, morphological and electrical studies on BCF-doped rreP3HT films in comparison to the prototypical F_4TCNQ-doped rreP3HT system, and found BCF to be a promising candidate for p-doping P3HT. Importantly, despite the low ionization efficiency of BCF (~ 13%) when compared to F_4TCNQ (~ 66%) in rreP3HT solutions (as shown also in chapter 5), both systems exhibited *integer charge transfer* and similar high ionization efficiency (ca. 40-50%) in solid-state films.[48] This is shown in Figure 6.1, in which similar levels of sub-band gap absorption are observed at a particular doping level, for both dopants. This was markedly different from the observation in doped solutions (see Figure 5.1). Preliminary morphology studies showed improved film quality in BCF-doped rreP3HT samples compared to F_4TCNQ-doped films. However, other aspects such as the packing behavior of this bulky dopant in the polymer matrix, were not yet investigated. Aside from that, there was growing interest in alternate processing techniques, such as *sequential doping*, which enable the fabrication of doped films with significantly improved film quality and consequently, high charge conductivity compared to the traditional *mixed solution doped* films.[40-41]This raised the question as to whether bulky dopants such as BCF could also be incorporated into films via sequential processing, particularly from solutions.

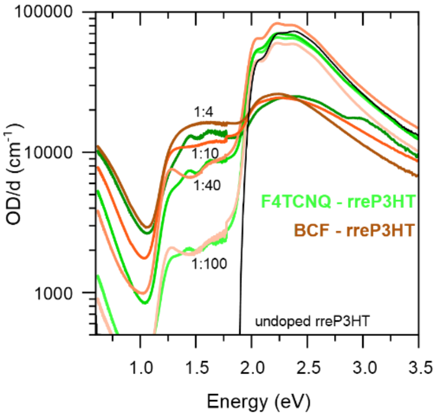

Figure 6.1. UV-Vis-NIR spectra of F_4TCNQ- and BCF-doped films (prepared by the conventional mixed-solution doping technique), showing similar absorption intensities for a particular doping level. The spectra have been normalized to the film thickness.[Replotted from my master thesis[48]]

In this chapter, we present our findings pertaining to BCF doped P3HT *films*, with a focus on the interdependence between the *film processing technique*, *charge transport* and *polymer morphology*. In the first part, we follow up on the previous work done during my master thesis, by presenting additional insight into the crystal microstructure and morphological changes that occur upon mixed solution BCF doping of rreP3HT films in comparison to F_4TCNQ doped films. Subsequently, we evaluate the suitability of two sequential processing techniques – a) sequential spin coating and b) dip doping for doping rreP3HT films with BCF, and find the latter to be more effective. We show that *dip doping* can lead to a $10X$ improvement in the electrical conductivity compared to mixed solution doping, and explain this gain by comparing and evaluating the morphology of the respective films.

The main characterization techniques used to investigate the doped films in this chapter are optical (UV-Vis-NIR and photoluminescence) spectroscopy, GIXRD for the studying the packing behavior within the P3HT crystallites, AFM for the film morphology and 4PP for conductivity measurements.

6.1 Morphology and charge transport in BCF doped rreP3HT films

The first step at the beginning of this work was to investigate the crystal microstructure of the undoped and BCF-doped rreP3HT films. Due to the high percentage of head-to-tail couplings, which enables backbone planarization and efficient packing, rreP3HT is able to form ordered crystallites in the solid state. The resulting packing motif can be nicely observed with X-ray diffraction experiments.

Figure 6.2 shows the GIXRD images[u] of undoped rreP3HT films, F4TCNQ- and BCF-doped rreP3HT films, cast on Si substrates from chloroform solutions. The undoped rreP3HT film shows characteristic diffraction peaks in the out-of-plane (h00), and in-plane (0h0) directions. The (h00) peaks derive from the vertical lamellar stacking[195] (also known as alkyl-stacking) of planarized P3HT chain segments whereas the (0h0) peak originates from the strong π-π interaction between the conjugated backbone (i.e. π-stacking) of a folded chain [56, 196] or between neighboring chains. The exact position of the diffraction peaks indicate that, within the crystallites in our undoped rreP3HT film, the conjugated subunits are stacked at a periodic distance of ca. 1.65 nm vertically (i.e. alkyl-stacking distance) and ca. 0.38 nm horizontally (i.e. π-π stacking distance), as depicted in Figure 6.2. This agrees well with the data reported in literature for rreP3HT [54, 56, 58, 111, 195], and implies a preferential *edge-on* orientation of the P3HT chains within the crystallites.

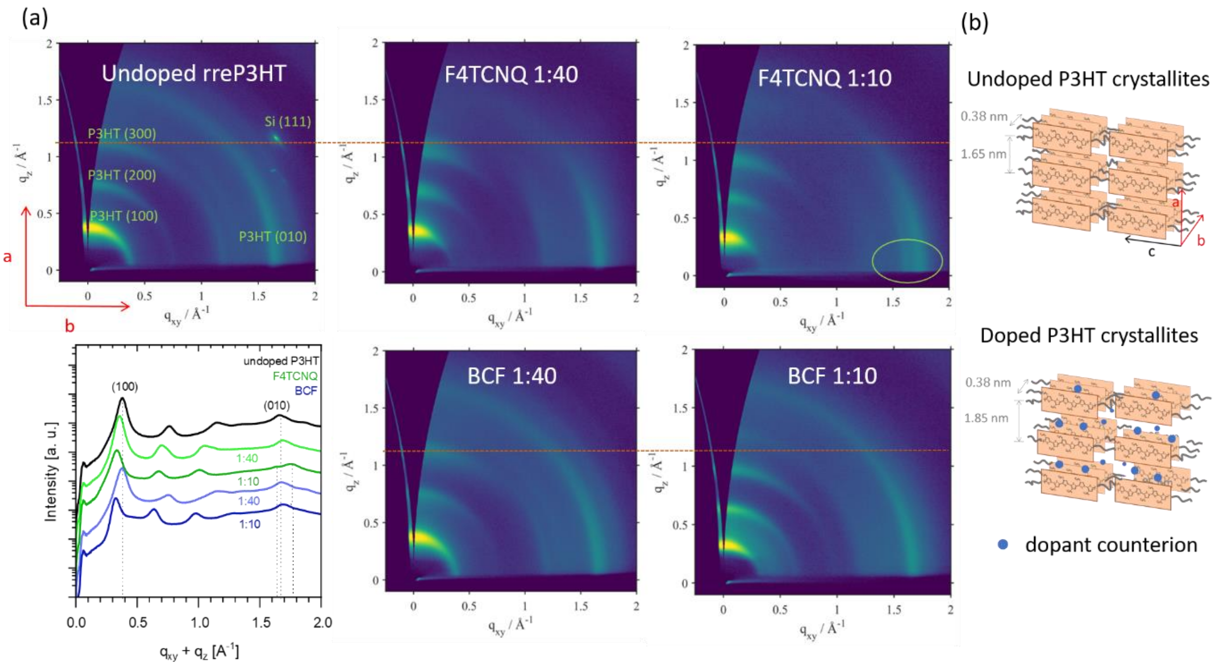

Figure 6.2. a) Grazing incidence X-ray diffraction (GIXRD) images of undoped rreP3HT, mixed-solution doped 1:40 and 1:10 ratio F$_4$TCNQ-doped rreP3HT and BCF-doped P3HT films. The

---

[u] GIXRD measurements were carried out by Dr. Ingo Salzmann (*Humboldt-Universität zu Berlin*)

dashed-red line is a visual guide assigned to the out-of-plane (300) peak of the undoped film. The integrated in-plane and out-of-plane intensities of the 2D images are shown in the graph (bottom left). b) Schematic illustration of the packing motif within the undoped and doped crystallites.

As anticipated, doping leads to changes in the polymer microstructure. Upon doping rreP3HT with F_4TCNQ, the out-of-plane (h00) peaks gradually shift to lower q_z values with increasing dopant loading, indicating an increase in the lamellar-stacking distance from ca. 1.65 nm in the undoped state to ca. 1.85 nm in the 1:10 ratio doped film. Moreover, in the 1:10 ratio film, the in-plane (010) peak at ca. 1.7 $Å^{-1}$ splits into two peaks. On the other hand, no such additional features are observed in the BCF-doped rreP3HT films. In fact, the 1:40 ratio BCF-doped rreP3HT film remains essentially identical to the undoped rreP3HT film, except for a slight broadening of the peaks, which could be due to a reduction in the fraction of crystallites. With further increase in the dopant loading (to 1:10 ratio), the out-of-plane (h00) peaks shift to lower q_z values, indicating that the lamellar-stacking distance increases to ca. 1.85 nm upon BCF doping, but the position and shape of the in-plane (010) peak remains predominantly unchanged.

The doping-induced changes in the XRD measurements are typically interpreted as changes in the periodicity within the crystallites due to the incorporation of the dopant molecules into the host matrix.[40, 58, 111, 114]. The increase in the lamellar stacking distance is widely attributed to the presence of the dopant counterions between the alkyl chains. In the case of our BCF-doped samples, based on the insights from Chapter-5, in which we demonstrated that the BCF in anion form is most likely absent in the samples, we instead attribute the increase in the lamellar stacking region in these films to the presence of BCF-*derived byproducts* of the doping reaction.

For small dopant molecules like F_4TCNQ, the dopant is believed to also intercalate into the π-π stacks of the host, resulting in the new peak at higher q values (at ca. 0.358 nm in real space).[58, 111, 114] This hypothesis is predominantly based on the optimized conformation of the F_4TCNQ-4T complex estimated using DFT,[197] and is further supported by inelastic neutron scattering experiments on F_4TCNQ-doped P3HT films.[198]

Recent studies, however, have challenged the idea of dopant-polymer co-crystallization. Hamidi-Sakr et al. investigated preferentially aligned sequentially doped F_4TCNQ-rreP3HT films using polarized UV – Vis – NIR spectroscopy and found that the transition dipole of F_4TCNQ lies perpendicular to the polymer chain, which would imply the absence of π-π stacked F_4TCNQ – P3HT.[199] In another study, Scholes et al. concluded that the F_4TCNQ anions reside in the crystalline lamellar region and the amorphous regions of the polymer instead of intercalating into the π-π stacks, based on optical and GIWAXS measurements on sequentially doped F_4TCNQ-doped rreP3HT films. [192] The new peak at higher q (i.e. smaller distance in real space) is instead suggested to originate from the *doped* P3HT crystallites which are packed closer as a result of *polaron delocalization*.[192] According to this theory, we would expect an additional peak in the (0h0) direction in our BCF-doped rreP3HT films, which is, however, absent.

One possible argument for the absence of these features could be that the bulky structure of BCF hinders efficient π-π stacking and polaron delocalization. A close comparison of the (010) peak positions in the GIXRD data of our undoped and 1:10 BCF-doped P3HT films (see Appendix Figure B.1) shows that there is indeed a small reduction of $\Delta \sim 0.06$ Å in the π-π stacking distance upon BCF doping. This agrees well with the findings of Liu et al., who conducted electron diffraction (ED) studies on P3HT films doped with the bulky Mo(tfd-CO_2)Me_3 dopant, and found a similar decrease ($\Delta \sim 0.08$ Å) in the π-π stacking distance after doping.[200] Notably, the Mo(tfd-CO_2)Me_3-doped films also exhibit only a single in-plane scattering peak.[200] Their DFT calculations revealed that the shift to lower π-π stacking distances is consistent with the presence of a charge on a 5-unit thiophene *dimer* (equivalent to a 1:10 doping ratio), irrespective of the size or type of the dopant, [200] which fits well to other experimental reports.[201-202] Additionally, the magnitude of the deviation of the π-π stacking distance in a *neutral dimer* to that in a *charged dimer* is shown to depend inversely on the length of the dimer. [200] This suggests that the F_4TCNQ-doped rreP3HT films display two well resolved in-plane peaks due to the localization of the charge on a shorter chain segment. On the other hand, the charge on the BCF-doped film shown here, and on the other systems reported in the literature,[200-202] which display only a single peak, may be more *delocalized*, whereby both the neutral crystallites as well as the doped crystallites have similar π-π stacking distances, which are mutually indistinguishable in the scattering experiments.

Notably, our preliminary ENDOR experiments on doped rreP3HT films hint at an identical proton hyperfine coupling strength in BCF and Mo(tfd-CO_2)Me_3-doped films, implying a similar degree of delocalization and environment around the charge (i.e. the P3HT polaron) in these two systems also in the solid-state (see Appendix Figure B.2). On the other hand, the polarons in the F_4TCNQ-

doped P3HT film seem to be more localized. Although these ENDOR studies were done on films with a 1:100 dopant:host ratio[v], the results appear to support the above hypothesis. Nevertheless, as these are only preliminary experiments, a concrete assignment cannot be made at this point.

Since only the *crystallites* within a sample can be probed using X-ray diffraction, we turn to atomic force microscopy (AFM) to obtain information about the nature and distribution of the amorphous and crystalline domains within the film. Figure 6.3 shows AFM topography images of undoped rreP3HT, F_4TCNQ-doped rreP3HT and BCF-doped rreP3HT films spin cast from mixed solutions in chloroform, measured in tapping mode. The *root mean square (RMS) roughness* value is displayed below each image. A common height scale is used (except for the undoped and 1:10 F_4TCNQ-doped rreP3HT image) to allow for better comparison. The undoped rreP3HT film is predominantly featureless and quite smooth. Upon doping, the picture changes dramatically. The 1:40 F_4TCNQ-doped P3HT film shows strong contrast, with a wide distribution of domain heights. With further increase of the dopant loading to 1:10, the film quality is severely compromised, as seen by the large isolated agglomerates and the high RMS roughness value of 50 nm. On the other hand, no such detrimental changes are observed in the BCF-doped films. At 1:40 ratio, the BCF-doped rreP3HT film shows characteristic doping-induced nanoscale *fibrillar structures*, which appear to be well dispersed in the amorphous P3HT matrix. Doping further to 1:10 ratio leads to a significant increase in the number of fibrils, while surprisingly still maintaining the film homogeneity, as indicated by the low contrast and RMS roughness value. These features are clearly observed in the high resolution topography and phase[w] images of the respective films shown in Figure 6.4.

---

[v] Highly doped samples typically undergo fast spin relaxation, which reduces signal intensity and in many cases even prevents pulse EPR measurements. Therefore, a lower doping concentration is chosen to obtain the optimal signal intensity.

[w] The AFM phase image is derived from changes in the signal amplitude due to the attractive/repulsive forces between the sample and the cantilever tip. Therefore, the phase image reveals important information about the rigidity of the sample. In a doped sample, doping-induced polymer aggregates as well as dopant-rich domains may manifest as "rigid" moieties.

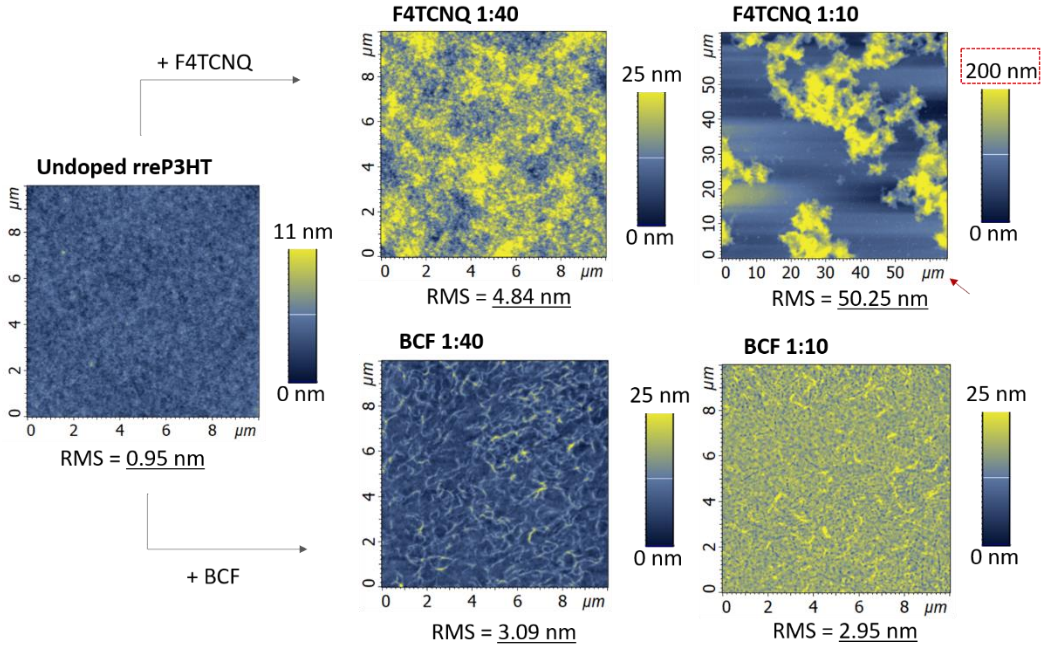

Figure 6.3. AFM topography images of undoped rreP3HT, and mixed solution F_4TCNQ and BCF-doped rreP3HT films, cast from chloroform solutions. The reported root mean square roughness values of the topography images were obtained from the ND-MDT image acquisition and analysis software (see Chapter-3 for details). The AFM image of the 1:10 F_4TCNQ-doped rreP3HT film was recorded during my master thesis,[48] and has a different length scale.

The close-up topography and phase images shown in Figure 6.4 reveal several differences in the aggregation mechanism in F_4TCNQ versus BCF doped films. In line with previous studies,[40] we see that in the presence of F_4TCNQ, the rreP3HT chains appear to form aggregates of small globular nanoparticles, which are clearly distinguished in the phase image. Moreover, the doped chains appear to have a higher tendency to stack vertically, as seen by the large fraction of domains with height > 18 nm in Figure 6.3 and 6.4.

In comparison, the BCF-doped rreP3HT chains tend towards forming long fibrillar aggregates. These nanoscale fibers are nicely discerned in the phase image, and can be reconciled with the strong π-π stacking signal observed via GIXRD (see Figure 6.2). Similar features have been previously observed in undoped and doped rreP3HT *nanowires* [203] and P3HT:PCBM films[204]. Importantly, most of these cases typically involve special processing methods (e.g. self assembly using poor solvents and slow cooling)[204] for obtaining the highly ordered structures. That BCF readily initiates nanofiber formation at room temperature in this system is, however, interesting and also puzzling. Notably, our preliminary AFM measurements on BCF-doped regiorandom P3HT films did not reveal such fibrillar structures (see Appendix Figure B.3). This suggests that steric factors might play a role, and could be a potential topic for further studies.

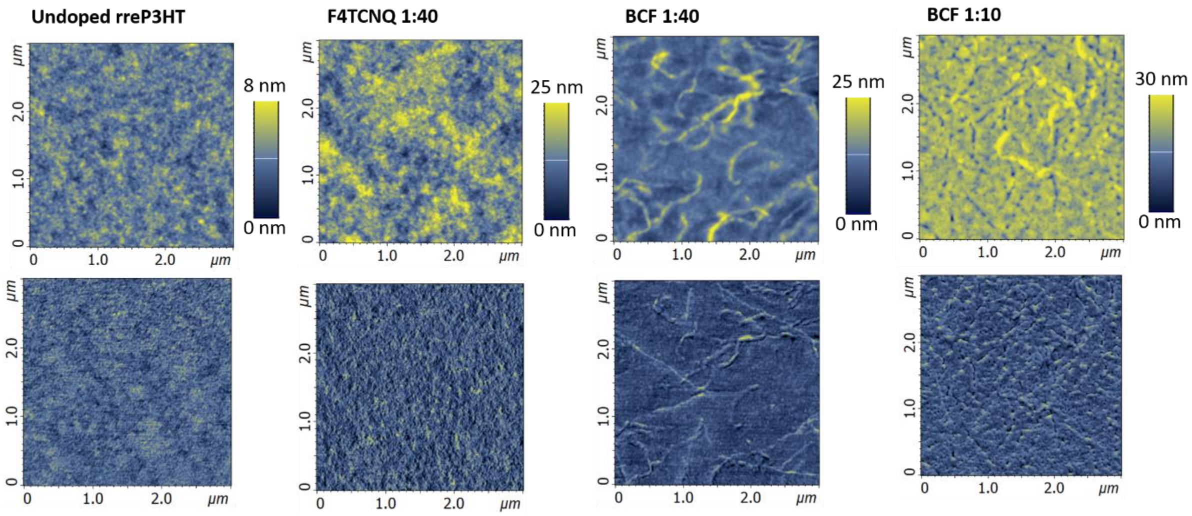

Figure 6.4. Close-up AFM topography images (top) and the corresponding phase images (bottom) of the undoped and doped rreP3HT films shown in Figure 6.3. The height scale of each sample has been optimized to obtain the best visualization of the features.

Having investigated the morphology of the doped films, we turn to study its impact on charge transport. Figure 6.5 compares the conductivity of F_4TCNQ-doped rreP3HT and BCF-doped rreP3HT films, measured using a home-built 4-point-probe setup. Despite the stark difference in the film morphology at 1:40 ratio, both films show equal conductivity of ca. 1 S m^{-1}. Upon doubling the dopant loading to a 1:20 ratio, the conductivity of the F_4TCNQ-doped film drops sharply to just 0.25 S m^{-1}, whereas that of the BCF-doped film doubles to 2.5 S m^{-1}. A further increase in the dopant concentration leads to a progressive improvement in the conductivity up to ca. 10 S m^{-1} (for the 1:4 ratio) of the BCF-doped film. On the other hand, the quality of the 1:10 ratio F_4TCNQ-doped film was so severely compromised by dopant-induced aggregation (see Figure 6.3), that it did not yield a measurable conductivity value.

It is well known that beyond a certain doping ratio, the conductivity of F$_4$TCNQ-doped rreP3HT films deteriorates dramatically, as a result of dopant oversaturation and phase segregation.[41, 111] It is worth noting that although higher conductivity values have been reported previously for similar (or even higher) doping ratios in *mixed-solution doped* F$_4$TCNQ-rreP3HT films,[59, 111] these measurements were typically taken from samples that were cast from solutions at elevated temperatures[59, 111]. Since subsequent reports[119, 136] as well as the discussion in Chapter-5 have shown that temperature influences the ionization efficiency and the extent of aggregation in the doped solution, and consequently, the film,[136] we believe the values shown here are reasonable.

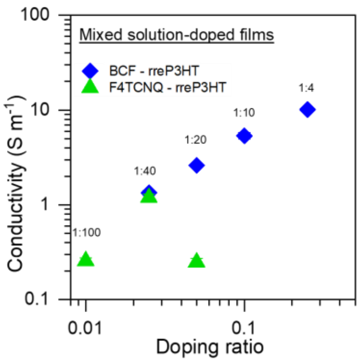

Figure 6.5. Conductivity of BCF and F$_4$TCNQ-doped rreP3HT films measured using the 4-point-probe technique.

Meanwhile, our results show that BCF-doped films do not suffer from these issues. One reason for this could be the high solubility of BCF compared to F$_4$TCNQ. However, a more important hint may lie in the *ionization efficiency*. We know from the discussion in Chapter-5 that the ionization efficiency of BCF is about 5 times lower than of F$_4$TCNQ in rreP3HT *solution*, whereas both dopants ionize quite efficiently in the solid-state (see Figure 6.1 and ref[49]). This low ionization efficiency of BCF in solution could be an advantage as it avoids the issue of excessive doping-induced aggregation in solution, while still retaining the ability to undergo efficient charge transfer with the P3HT chains during film formation. Therefore, a design strategy for dopant molecules in the future could be to suppresses ionization in the *solution* and selectively activate it in the *solid-state*.

The next step was to see if the conductivity of BCF-doped films could be improved further, using alternative film fabrication techniques such as sequential spin-coating.

6.2. Sequential dip-doping to improve the charge transport

As mentioned previously, several groups have investigated alternative solution processing techniques such as *sequential spin-coating* and *dip-doping* from orthogonal solvents, to improve the performance of doped films. [40-41, 205-208] As the orthogonal solvent merely swells the polymer chains rather than dissolve them, the original polymer morphology is essentially preserved even after doping.

To that end, we attempted to dope rreP3HT films with BCF via *sequential spin-coating*, with dichloromethane (DCM) as the orthogonal solvent. Unfortunately, this technique proved to be unsuitable for doping with BCF. Control of doping level in sequentially spin-coated films is typically achieved by varying the dopant concentration in the orthogonal solvent; more polarons are created in the film by applying a more concentrated dopant solution while spin-coating.[40-41] Although this works very well for doping rreP3HT films with F_4TCNQ (see Appendix Figure B.4 and refs [40-41]), the UV-Vis-NIR spectra of sequentially spin-coated BCF-rreP3HT films showed inconsistent and low levels of doping (see Figure B.4). This was presumably due to the bulky nature of BCF, which prevented quick diffusion through the swollen polymer onto favorable sites for charge transfer. Therefore, we subsequently pursued dip-doping, in which the undoped polymer film is dipped into a dopant:orthogonal solvent mixture for a specific duration of time, allowing for sufficient dopant incorporation into the film. We note that although various groups have reported on using a series of orthogonal solvents or solvent blends to tune the *extent* and *region* of polymer swelling, and thereby, the doping levels in films,[41] [40] we have used only DCM for our studies so as to minimize complications arising from unwanted solvent interactions. Similarly, although P3HT films cast from other solvents such as o-dichlorobenzene and p-xylene have been shown to have higher crystallinity than that cast from CF,[192, 209] in order maintain consistency and enable a reasonable comparison with the findings in Chapter-4 and 5, all the films were cast from CF (unless mentioned otherwise).

Optical spectra of dip-doped BCF-rreP3HT films

Let us first consider the optical absorption of the dip-doped BCF-rreP3HT films. Figure 6.6 shows the UV-Vis-NIR spectra of a series of BCF-doped rreP3HT films that were submerged in the BCF:DCM solution for different durations. Strong sub-band gap absorption, which is assigned to that of the *delocalized P3HT polaron* is observed even after a "quick" dip of the rreP3HT film into the dopant solution. This is accompanied by *bleaching* of the neutral rreP3HT absorption signal at ca. 2.5 eV. With increasing dipping time, the polaron absorption signal grows further, but to a much smaller extent, and saturates within 1 hour. This is quite reasonable because already within 1 minute (dipping), the polaron level nearly matches that of a 1:10 ratio mixed-solution BCF-doped rreP3HT film. Presumably, all the available sites in the polymer layer are already occupied by the dopant within 1h of dipping. This is consistent with the evolution of the film thickness, which increases upon dip-doping by ca. 11% in the "quick dip" film, ca. 13% in the 1 h doped film, and then remains constant despite further increase in dipping time.

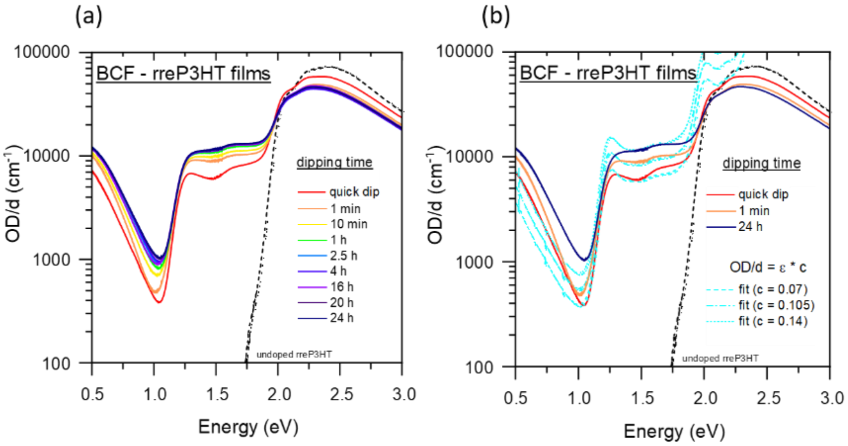

Figure 6.6. a) UV-Vis-NIR spectra of BCF-doped rreP3HT films prepared by dip doping. The pristine rreP3HT films were cast from chloroform, and the films were dipped for a specific duration in DCM solutions of BCF. b) Reconstructed optical absorption spectra (dashed blue lines) of select dip-doped BCF-rreP3HT films (see main text for details).

Using the *Beer-Lambert law* and the *molar extinction coefficient spectrum* of the delocalized P3HT polaron shown in Figure 5.9a, we analyzed the optical spectra of selected dip-doped films to determine the approximate polaron concentration. The fitted curves shown in Figure 6.6b coincide only to a certain degree with the experimental data. This is because the molar extinction coefficient was estimated from *solution* spectra, which already differ slightly from the optical spectra of the corresponding solid-state films.[36, 49] Recalling the discussion in Chapter-5, the Vis-NIR region of the absorption spectrum is highly sensitive to the backbone conformation and crystallinity,[192] which presumably causes the mismatch in the fit below ca. 1 eV, at ca. 1.3 eV, and beyond 2 eV. Therefore, for our estimation, we have considered the best fit at 1.5 eV. Secondly, although bipolaron formation at high doping levels has been suggested,[115, 193] our optical spectra do not exhibit the characteristic NIR features assigned to P3HT bipolarons that have been reported in the literature.[190-191] Therefore, we have assumed that the Vis-NIR features in our optical spectra are derived entirely from delocalized P3HT polarons.

A rough estimation based on the assumptions mentioned above tells us that the polaron concentration in the "quick dip" sample is ca. 0.07 mol L^{-1}, and increases to ca. 0.11 mol L^{-1} within a minute of dipping. The 24 h sample has a polaron concentration of ca. 0.14 mol L^{-1}. In comparison, the concentration of charged P3HT in the 1:10 mixed-solution doped BCF-rreP3HT film was found to be ca. 0.16 mol L^{-1} [49]. With this in mind, we turn to evaluate the efficiency of charge transport through the dip-doped films.

Charge transport in dip-doped films

Figure 6.7 shows the 4PP conductivity of 5 batches of dip-doped BCF-rreP3HT films, plotted as a function of dipping time. Already for 1 minute of dip-doping, we see a higher conductivity than that of a 1:4 mixed-solution BCF doped film (shown in Figure 6.5), confirming that a higher conductivity range can be accessed by employing this technique. More importantly, we see that despite the negligible difference in the sub-band gap absorption of the films beyond 1 h of dip-doping (see Figure 6.6a), the conductivity of the films continues to increase with dipping time. In fact, the conductivity of the 24 h dip-doped film is ca. 4 times higher than the conductivity of a 1 h dip-doped film.

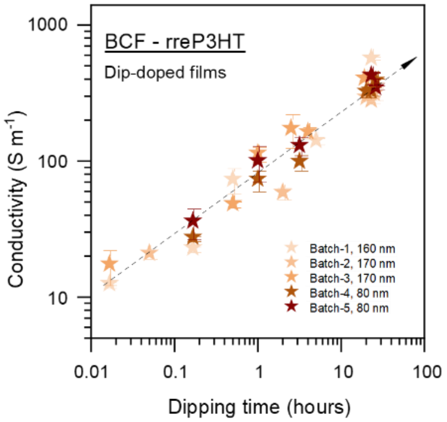

Figure 6.7. 4-point-probe conductivity values of 5 batches of dip doped BCF-rreP3HT films, plotted as a function of dipping time. The error bars correspond to the standard deviation from the arithmetic mean (solid symbol) of 6-8 measurements at different positions on the film. The dashed arrow is a visual guide.

Since the conductivity (σ) of a sample is determined by the number of charge carriers (n), as well as the mobility of the carriers (μ) according to the relation $\sigma = en\mu$, the increase observed (in Figure 6.7) implies that with longer dipping time, either more polarons are being created (increase in n), or that the mobility improves, or a combination of both factors. The unchanging UV-Vis-NIR signal for samples beyond 1 h of doping (Figure 6.6a) suggests that the number of charge carriers (n) does not increase significantly beyond this duration. However, the bulky size of BCF might initially restrict it to the surface or top layers of the P3HT film, which may then be overcome with increased dipping time and consequently, additional swelling.

To verify whether dopant distribution (i.e. inhomogeneity) is responsible for the dipping-time-dependent increase in conductivity, we compared the *photoluminescence* (PL) *emission* measured from the *front* (film side) and the *back* (glass side) of 280 nm thick 1 h and 24 h dip-doped films (shown in Appendix Figure B.5). Since the PL emission from an undoped sample is typically *quenched* upon doping, if the doped domains were indeed concentrated only at the surface/ top layers of the film, we would expect a stronger PL emission from the "glass-side" of the 1 h dip-doped film compared to the 24 h dip-doped film. However, since the PL signal of both samples were consistent for all measurements (Figure B.5), we can be fairly certain that the dopant is homogeneously distributed throughout the film, even in the 1 h dip-doped sample. This implies that the conductivity increase most likely stems from an increase in the mobility of the charges through the film.

As mentioned in section 2.2.4, the direct and accurate measurement of charge carrier mobility in doped films is quite challenging, and is outside the scope of this work. A rough calculation based on the polaron concentration obtained from the optical spectra, and the conductivity data indicates that the "apparent" mobility (of bound and mobile charges combined) increases from 0.026 ± 0.007 $cm^2\ V^{-1}\ s^{-1}$ in the quick-dip film to 0.10 ± 0.009 $cm^2\ V^{-1}\ s^{-1}$ after 1 h of dipping, and ultimately reaches ca. 0.31± 0.108 $cm^2\ V^{-1}\ s^{-1}$ in the 24 h dip-doped film. This data is summarized in Table 6.1. In comparison, the apparent mobility of the 1:10 ratio mixed-solution BCF-rreP3HT film amounts to ca. 0.003 ± 0.0003 $cm^2\ V^{-1}\ s^{-1}$. Note that these values are most likely overestimated, because 1) the estimation is based on the assumption that all the doping-induced polarons are free to move (i.e. no traps are present in the system, which is unlikely[36, 210]) and over that, 2) there is some ambiguity in the polaron concentration, as the fit (in Figure 6.6b) is not perfect. In the literature, AC Hall effect measurements on sequentially spin-coated F_4TCNQ-doped rreP3HT films indicate μ to be between 0.003 $cm^2\ V^{-1}\ s^{-1}$ and 0.02 $cm^2\ V^{-1}\ s^{-1}$, with conductivity ranging from ca. 0.02 $S\ m^{-1}$ to 157 $S\ m^{-1}$ in the corresponding samples.[41] In another study, the AC Hall effect-derived μ of vapor doped F_4TCNQ-PBTTT films is reported to be 1.8 $cm^2\ V^{-1}\ s^{-1}$ (with σ = 24800 $S\ m^{-1}$).[143] However, we cannot draw a direct correlation between this information and our samples, as the system and preparation conditions are vastly different. Therefore, to make a general comment about the efficiency of charge transport in our samples, it is useful to first study the morphology and the microstructure of the dip-doped films.

Table 6.1. Summary of the electrical properties of selected mixed-solution and dip-doped BCF-rreP3HT films

Sample	Polaron density		Conductivity	Apparent mobility
(BCF-rreP3HT film)	$mol\ L^{-1}$	m^{-3}	$S\ m^{-1}$	$cm^2\ V^{-1}\ s^{-1}$
1:4 mixed soln	0.16	9.63×10^{25}	5.35 ± 0.45	0.0034 ± 0.0003
"quick" dip	0.07	4.21×10^{25}	17.56 ± 4.99	0.0260 ± 0.0074

1 h dip	0.105	6.32×10^{25}	107.90 ± 9.69	0.1065 ± 0.0096
24 h dip	0.14	9.63×10^{25}	428.40 ± 145.95	0.3172 ± 0.1080

Total density of sites (3HT) = 4×10^{27}, assuming a P3HT mass density[195] of 1.1 g cm^{-3}

Figure 6.8 shows the AFM images of undoped and dip-doped BCF-rreP3HT films, plotted with a constant height scale. Unlike the mixed-solution BCF-doped rreP3HT films which showed characteristic nanoscale fibrillar structures (Figures 6.3 and 6.4), the dip-doped samples predominantly retain the morphology of the undoped film. Nevertheless, the contrast increases upon doping and with dipping time (particularly in the 24 h sample), indicating an increase in the height of certain domains. This is also reflected in the RMS roughness, which increases slightly with doping.

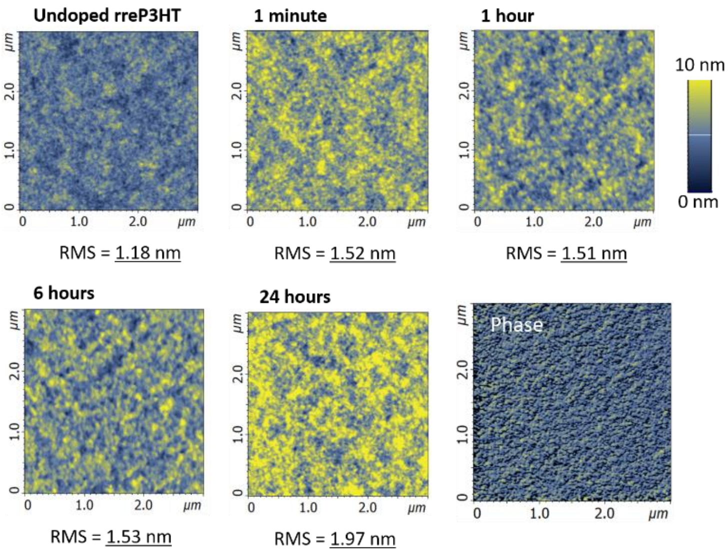

Figure 6.8. AFM topography images of undoped rreP3HT and dip-doped BCF-rreP3HT films plotted by keeping a constant height scale. The dipping time is mentioned above the image and the RMS roughness values are given below each image. A representative phase image of a dip-doped sample (6h) is shown at the bottom right.

Moving on to the GIXRD results, a comparison of the peak positions and intensities of the undoped, 1:10 ratio mixed-solution doped, and (10 minute) dip-doped BCF-rreP3HT films shown in Figure 6.9 indicates that the dopant-derived byproducts are predominantly located in the alkyl chains, as in the case of mixed-solution doped films. This is consistent with the observation of increased film thickness in the dip-doped films, as mentioned earlier. The peak positions of the dip-doped film closely mirror those of the 1:10 mixed-solution doped film, indicating a similar packing behavior within the doped crystallites, and a preferential edge-on orientation of the chains. However, the overall intensity of the in-plane and out-of-plane peaks is lower in the dip-doped samples. This suggests a gain in isotropy. The XRD data of a 24 h dip doped film would have provided valuable insight into the impact of dipping time on the packing motif, particularly to see changes if any, in the isotropy of the film. However, we were unsuccessful in preparing a suitable sample due to delamination of the polymer layer from the Si substrate. A small modification in the experimental setup[x] should be able to fix that issue, and could be a potential experiment for the future.

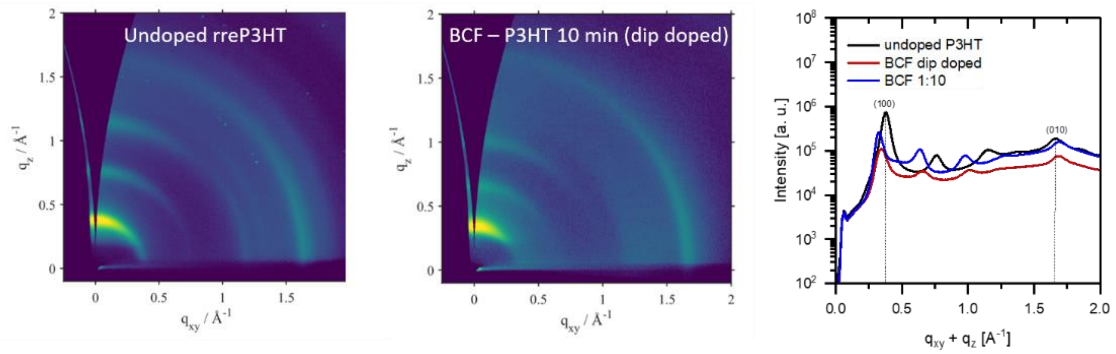

Figure 6.9. GIXRD images of undoped rreP3HT (left) and 10 minute dip-doped BCF-rreP3HT film (middle); and the corresponding integrated in-plane and out-of-plane intensity as a function of *q* (left).

Based on the above AFM and GIXRD data, the marked improvement in the charge transport in dip-doped BCF-rreP3HT films compared to the mixed-solution doped films can be explained by the presence of a higher fraction of *tie chains*[40, 211] in the dip-doped films. It has been suggested that although charge transport within highly ordered individual nanofibers/nanowires is very efficient, the charges typically get trapped at the grain boundaries, resulting in a reduced overall

---

[x] For example, by placing the undoped film in a shallow container with just enough volume of the dopant:orthogonal solvent to cover the film. Importantly, the setup should be left undisturbed, and after the stipulated time, the sample must be picked up very carefully such that the potentially floating film is “collected” by the substrate.

transport in the bulk.[68] We can envision a similar situation in our mixed-solution BCF-doped films, which appear to contain numerous nanofibers that are, however, quite disconnected (see Figure 6.4). On the other hand, in the dip-doped films, prior to doping, the undoped P3HT film has a more homogeneous morphology, with a strong interconnected network between the aggregated and amorphous domains. Upon dipping in the dopant:DCM mixture, initially, a few of the chains in the amorphous domains get doped, and due to the interconnected network, the film already exhibits better charge transport than the mixed-solution doped film. The additional increase in conductivity with increasing dipping time could be due to two factors, 1) the existing aggregated domains are able to grow further as a result of the neighboring amorphous chains swelling in the orthogonal solvent medium, and 2) reduction or passivation of *voids* in the polymer matrix, by the orthogonal solvent. It is entirely possible for both of these processes to occur simultaneously in our system. The increase in AFM contrast in the 24 h dip-doped film (shown in Figure 6.8) is consistent with an increase in the size of the aggregated domains.

6.3 Thermal stability of doped films

Finally, it is worth investigating how stable the doped films are towards post-processing treatments such as thermal annealing, which is commonly employed during the fabrication of devices to improve the film morphology. Figure 6.10 shows the room temperature 4PP conductivity values of doped P3HT films that have been progressively annealed for ca. 15 minutes at different temperatures[y].

The conductivity of the 1:40 F_4TCNQ-doped rreP3HT sample remains constant till about 120 °C, after which it starts deteriorating. The mixed-solution BCF-doped rreP3HT films exhibit a curious behavior. Upon annealing the samples to 60 °C, the conductivity increases in these film. On the other hand, no such observation is made in the dip-doped samples, whose conductivity remain unchanged at this temperature. However, when both mixed-solution or dip-doped BCF-rreP3HT samples are heated to 80 °C, the conductivity reduces slightly. Upon heating the samples further to 100 °C and beyond, the conductivity falls rather sharply.

---

[y] i.e. after the initial σ measurement at room temperature (RT), the films were heated for 15 minutes at the specific annealing temperature, then cooled back to room temperature, and measured (after waiting for ca. 10 minutes).

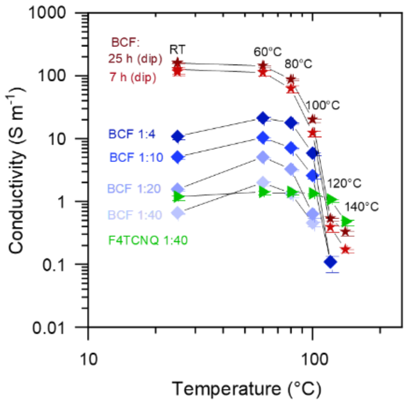

Figure 6.10. Change in the conductivity of doped rreP3HT samples as a function of annealing temperature.[z] The solid symbol indicates the mean conductivity value of measurements at six different regions on the film (and the error bar is the standard deviation from the mean value). The black lines are a visual guide. The films were ca. 120 nm thick. Note that these values have been measured at room temperature.

The increase in the conductivity of the mixed-solution BCF-doped films upon annealing to 60 °C could on the one hand be due to the removal of residual solvent molecules or voids, whose presence may lead to trapped charges, but could also be due to an improvement in the crystallinity, as a result of a rearrangement of chain segments. For example, chains that are "frozen-in" during film formation could be relieved upon annealing.[212] Such a change is presumably not observed in the case of the dip-doped films because, in the process of swelling the polymer, the orthogonal solvent already provides a pathway for the chains to attain the energetically favored conformation.[213]

In the F_4TCNQ-doped rreP3HT film on the other hand, σ remains quite stable until 100 °C, beyond which it decreases due to the evaporation of F_4TCNQ. This is in line with the findings of Kroon et al., who observed a similar decrease in σ of F_4TCNQ-doped P3HT films upon thermal annealing.[214] In another study, Hase and co-workers studied the F_4TCNQ de-doping process (in rreP3HT films) at different temperatures and found using conductivity and GIXRD measurements that de-doping starts already at 80 °C, and the P3HT layer gets completely de-doped upon annealing at

---

[z] Some of this data has been published in ref 173. Mansour, A. E.; Lungwitz, D.; Schultz, T.; Arvind, M.; Valencia, A. M.; Cocchi, C.; Opitz, A.; Neher, D.; Koch, N., The Optical Signatures of Molecular-Doping Induced Polarons in Poly(3-Hexylthiophene-2,5-Diyl): Individual Polymer Chains Versus Aggregates. *J. Mater. Chem. C* **2020**, *8*, 2870-2879.

120 °C.[89] However, the authors also show that the duration of annealing impacts the results, which might explain the difference between our observations (as their samples were annealed for 1 h whereas ours were annealed for 15 minutes).

In general, the low thermal stability of doped organic semiconductors can be attributed to one or more of the following reasons[215]: 1) the diffusion or sublimation of the dopant molecules from the host matrix,[42, 89, 214] 2) chemical transformation or degradation of the dopant and/or host material, or 3) modification in the nature of interaction between the dopant and host brought about by thermal energy[85]. In the case of F_4TCNQ-doped P3HT, the thermal instability in films is most commonly attributed to the *sublimation* of F_4TCNQ from the P3HT matrix.[214, 216] For example, Kroon et al. demonstrated that F_4TCNQ undergoes sublimation at a higher rate and from a lower temperature (110 °C) from the P3HT matrix than from the p($g_4$2T-T) matrix (120 °C), the latter of which is a *polar* tetraethylene glycol-functionalized polythiophene.[214] It has been suggested that polar side-chains on the polymer backbone may help stabilize the dopant anion against diffusion.[214, 216]

However, in a very recent study, Watts and coworkers argue that the thermal instability in this particular system is instead due to the thermally-induced *chemical transformation* of the F_4TCNQ radical anion ($F_4TCNQ^{\cdot -}$) to the protonated F_4TCNQ dianion (HF_4TCNQ^{-}).[215] Based on UV-Vis-NIR, XPS, and FTIR studies of thermally annealed F_4TCNQ-doped rreP3HT films, they suggest that the H-atom on the α-carbon of the hexyl group of P3HT provides the proton to the F_4TCNQ^{2-}. This is further corroborated by the fact that a similar study on p($g_4$2T-T) (which does not contain any methylene groups at that particular reactive position) indicates no presence of the characteristic HF_4TCNQ^{-} bands in any of the measurements.[215]

Let us now turn to the case of BCF-doped rreP3HT films, which show a de-doping onset at ca. 80 °C. We saw already in section 5.2 that a significant fraction of BCF-doped rreP3HT undergoes irreversible de-doping upon heating upto 80 °C, even in solution state. This strongly suggests that dopant and/or polymer undergo chemical degradation/ transformation, particularly considering the proposed BCF doping mechanism in the literature[163], section 5.1 of this thesis, and the recent reports on doped-P3HT's thermal instability[215]. A more concrete description of the BCF de-doping mechanism requires additional multidisciplinary investigations which are, unfortunately, out of the scope of this work. However, it is important to keep in mind that molecularly doped organic semiconductors are, by nature, quite susceptible to de-doping under thermal and/or chemical stress (eg. solvent) because they are based on redox reactions between the dopant and host rather than covalent bonding.[25] Therefore, this reinforces the notion that one must carefully consider any changes made to the environment that might disturb the equilibrium of the charge transfer reaction.

6.4 Summary

In this chapter, the morphology and optoelectronic properties of BCF-doped rreP3HT films prepared by the conventional mixed-solution (solution blending) technique was compared to that of sequentially processed (i.e. dip-doped) films, using GIXRD, AFM, optical spectroscopy and conductivity measurements. It was found that the crystallites within the mixed-solution BCF-doped rreP3HT films still retain their edge-on orientation, with the dopant-derived byproducts (e.g. the passivated counterion) dispersed among the alkyl chains, and/or in the amorphous domains. Unlike with F_4TCNQ, the rreP3HT chains in the mixed-solution BCF-doped films attain a more homogeneous, nanofibrillar morphology, which resulted in improved conductivity, even at higher doping ratios for the BCF-doped films. Sequential spin-coating was found to be sub-optimal for BCF-doping. Instead, dip-doping worked very well for this system, resulting in doped films with over 5 S cm^{-1} conductivity (10X improvement compared to that of mixed-solution doped films) after 24 h of dipping in the dopant:orthogonal solvent mixture. Based on AFM results, this gain in conductivity was mainly attributed to the presence of a larger number of tie chains in the dip-doped film, which reduces traps, thereby improving the charge transport through the layers. Finally, it was shown that BCF-doped rreP3HT films are only stable to heating up to ca. 80 °C. Beyond this temperature, the conductivity of both mixed-solution and dip-doped films starts deteriorating, presumably due to dopant degradation, implying that these films are not very suitable for applications requiring post-processing thermal annealing.

7. Summary and Outlook

This thesis set out to improve our understanding of the underlying mechanisms involved in molecular doping of semiconducting polymers. This was done by studying the doping-induced changes in solutions and films of the prototypical polymer P3HT, primarily using UV-Vis-NIR spectroscopy, EPR spectroscopy, grazing incidence X-ray diffraction, atomic force microscopy and electrical conductivity measurements.

The Lewis acid BCF was the main (p-) dopant of choice. This was chosen because, at the beginning of this work, the Lewis acid doping mechanism was still largely unknown. Yet, BCF was found to undergo integer charge transfer with P3HT, both in solutions and films, similar to the traditional molecular p-dopant F_4TCNQ. Unlike F_4TCNQ, BCF is much easier to work with due to its high solubility. Moreover, the absorption signal of the BCF anion does not interfere with that of the P3HT polaron, making it easier to observe the doping-induced changes on the polymer backbone. Therefore, this made for an interesting system to carry out further studies.

A critical challenge encountered at the initial phase of this project was the slow and inconsistent polaron formation in the BCF-doped rreP3HT solutions. Hence, the first course of action was to determine what external factors influence polaron formation in this system. This is the focus of Chapter-4. Since it was previously suggested that the presence of aggregates may improve doping efficiency,[113] we studied the kinetics of polaron formation in a BCF-doped *pre-aggregated* rreP3HT solution using UV-Vis-NIR spectroscopy. Our results showed that pre-aggregation does not improve the kinetics of polaron formation in BCF. However, we found that 1) exposure to white light, 2) the duration of light exposure, and 3) the solvent polarity impacted the concentration of polarons in the BCF-doped rreP3HT solution. For example, in the absence of white light, BCF barely dopes rreP3HT in *chloroform*, but within minutes of light exposure, the polaron level observed by UV-Vis-NIR spectroscopy increases. Alternatively, in *chlorobenzene*, BCF was found to dope rreP3HT even in the absence of light. Nevertheless, light was found to significantly increase the concentration of polarons, even in chlorobenzene-based solutions.

Around this time, the Nguyen group at Santa Barbara, USA reported a study elucidating the Lewis acid doping mechanism.[163] Based on their hypothesis that BCF doping involves an *endothermic* rate-limiting *polymer protonation* step, we were able to conclude that light exposure helps in overcoming the energetic barrier to P3HT protonation, resulting in increased polaron concentration. Importantly, this finding resolved the problems in sample inconsistency, as care was taken in all subsequent experiments to also ensure consistent levels of light exposure during sample preparation, amongst other standard parameters such as polymer and dopant concentration.

With an established sample preparation routine, the next step was aimed at studying the interplay between the polymer backbone arrangement, the dopant size/structure and the doping mechanism. To that end, two forms of P3HT – rreP3HT and rraP3HT, whose chains differ in their ability to planarize and aggregate, and three different dopants – F_4TCNQ, $Mo(tfd\text{-}CO_2Me)_3$ and BCF, which differ in size and/or type, were chosen. This was the focus of Chapter-5. To carry out reliable qualitative as well as quantitative estimations, we complemented the UV-Vis-NIR absorption measurements with EPR spectroscopy, the latter of which is selectively sensitive to the presence of paramagnetic species such as polarons. This powerful spectroscopic combination allowed for a comprehensive study of the dopant:polymer solutions, which led to an unambiguous differentiation of the optical signatures of the resultant doping-induced species into 1) *delocalized polarons* on aggregated chains, 2) *localized polarons* on isolated chains and 3) *charge-transfer complexes*. Using ENDOR spectroscopy on frozen solutions, we demonstrated that at low temperatures, the polaron formed by integer charge transfer is delocalized over 12 thiophene units in the case of doped rreP3HT chains. In doped rraP3HT, however, we found that the rather small fraction of polarons that are present, are delocalized over only 6 thiophene rings. By correlating the optical signatures obtained from UV-Vis-NIR and the *spin density* obtained from EPR spectroscopy, we were also able to estimate the *molar extinction coefficient* of all three doping-induced species in P3HT, which has not been reported previously in the scientific community.

A key contribution of this work is regarding the role of structural order on the type of doping-induced species formed. Our studies showed that irrespective of their shape/size, all three dopants lead to delocalized polarons on the rreP3HT backbone, with identical extents of charge delocalization (at low temperatures). However, when the ability of the polymer chains to aggregate is inhibited, either intrinsically as in rraP3HT, or extrinsically by elevating the solution temperature, the nature of the dopant-polymer interactions change. This is illustrated in Figure 7.1. This suggests that <u>rather than the dopant size or type, the polymer backbone arrangement plays a</u>

more crucial role in determining the nature of the doping-induced species (doping mechanism) and the ionization efficiency. Although limited by the sample size, this is an important insight for the design and selection of semiconducting polymers for doping in the future.

Another surprising observation was that all 3 dopants produce identical polaronic absorption features in the rreP3HT solutions despite differences in the chemical nature of the dopants, doping process, and interactions between the dopant-polymer (see Figure 7.1). This led us to hypothesize that the often reported differences in the NIR region of the optical absorption spectra in the *solid-state* (i.e. doped films) in the literature stem from mechanical strain of the polymer chains.

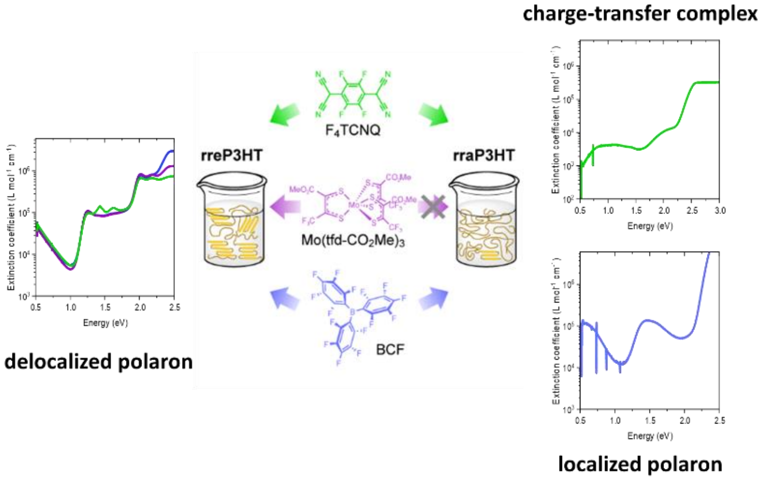

Figure 7.1. Illustration depicting the influence of polymer structure and dopant size on the nature and optical signature of doping-induced species in p-doped P3HT in solution. All three dopants form identical delocalized polarons with rreP3HT whose chains are able to aggregate. Conversely, when the chains are unable to aggregate, as in rraP3HT, inefficient charge transfer mechanisms prevail

The final part of this thesis, i.e. Chapter-6, dealt with the morphological and optoelectronic properties of doped films. The aims of this chapter were to 1) build upon previously conducted research on BCF-doped rreP3HT films[49] by studying the film microstructure and morphology in order to gain a better overall understanding of the doping process in films, and 2) verify whether bulky dopants such as BCF can also be incorporated into the film via *sequential doping* techniques.

Atomic force microscopy and grazing incidence X-ray diffraction studies showed that mixed-solution BCF-doped rreP3HT chains tend to form long nanofibrillar structures in the solid-state, with the chains within the crystalline domains adopting an edge-on orientation. Such highly ordered morphologies in P3HT films are typically obtained only through special processing techniques,[204] indicating that BCF-rreP3HT is indeed a unique system to investigate.

It was shown that unlike *mixed-solution* F_4TCNQ-doped rreP3HT films, BCF-doped rreP3HT films exhibit a homogeneous morphology even at higher doping levels. This directly resulted in a high electrical conductivity of 10 S m^{-1} for the 1:10 BCF-doped rreP3HT film, which is in contrast to the 1:10 F_4TCNQ-doped film whose morphology was severely compromised by doping-induced aggregation.

In the second part of Chapter-6 we demonstrated that even higher conductivity values up to ca. 350 S m^{-1} could be attained for BCF-rreP3HT films by sequential *dip-doping*, in which the dopant is introduced into the pre-cast polymer film by dipping the film in a dopant-orthogonal solvent mixture for a specific duration. This modification in the processing technique allowed for a more homogeneous film morphology with the aggregated domains interconnected by *tie chains* that facilitate efficient charge transport through the film. Although optical absorption from the dip doped films did not reveal an increase in the polaron concentration beyond 1 h of dip-doping, the conductivity of the films increased further with increased dipping time. Based on morphology studies, this was assigned to the orthogonal solvent-induced growth in the size of the aggregated domains, and the passivation of pre-existing voids, both of which can positively influence charge transport.

Although this thesis answered several questions regarding the underlying doping mechanism in semiconducting polymers, some aspects remain yet unclear and require additional investigations. For example, in dip-doped BCF-rreP3HT films, we were unsuccessful in examining the impact of dipping time on the film microstructure due to experimental and time constrains. However, as suggested in Chapter-6, this can be easily studied using GIXRD and a modification in the sample preparation. Based on our solution and film studies of BCF- and F_4TCNQ-doped rreP3HT, we hypothesized that a low/delayed ionization efficiency of the dopant in the polymer solution may be a design strategy for obtaining a well-ordered homogeneous morphology without premature doping-induced aggregation in mixed-solution doped films. This may be verified by extending the optical and morphological studies to include Mo(tfd-CO_2Me)$_3$-doped rreP3HT films, and other dopant:host combinations which exhibit a similar behavior. In Chapter-4, we identified that light helps in overcoming the energetic barrier to polymer protonation in the Lewis acid doping mechanism. The fact that this effect is more pronounced in certain solvents demonstrates the complex relationship between the polymer chain conformation, solvent polarity, the reaction mechanism, and calls for further multidisciplinary research to disentangle the various factors influencing doping process.

This work demonstrated that optical and electron paramagnetic resonance spectroscopy jointly serve as a powerful tool for studying doping processes in organic semiconductors. In *doped rreP3HT solutions*, our ENDOR experiments revealed similar extents of charge delocalization for all 3 considered dopants, but preliminary ENDOR experiments on *doped rreP3HT films* suggested differences in the extent of charge delocalization. Expanding the study of doped films further with optical and EPR techniques, for rraP3HT as well as other polymer-dopant systems can provide valuable insight into the doping mechanism in polymers.

In conclusion, this thesis has furthered our understanding of molecular doping process in semiconducting polymers in solution and films. The ideas shared here, in the form of experimental methods, results obtained, or theories stated, serve as an important basis for future research in this field.

Appendix

A. Appendix for Chapter-5:

1. Polaron formation in Mo(tfd-CO_2)Me_3 doped solutions

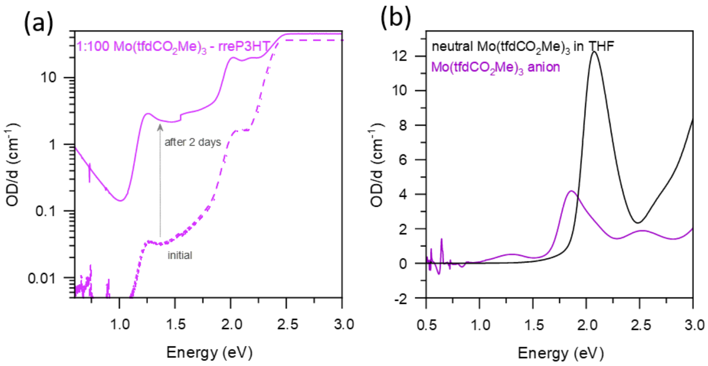

Figure A.1. UV-Vis-NIR absorption spectra of (a) 1:100 ratio Mo(tfd-CO_2Me)$_3$ doped rreP3HT in chloroform, measured immediately (dashed line) and two days (solid line) after mixing. (Note: the kink near 1.5 eV is an artifact caused due to the detector change in the instrument) (b) neutral Mo(tfd-CO_2Me)$_3$ (black line), and Mo(tfd-CO_2Me)$_3$ anion (pink line) in THF solution. The spectra in (b) coincide well with data reported in the literature[93].

2. Rescaled absorption and molar extinction coefficient spectra of the charged species

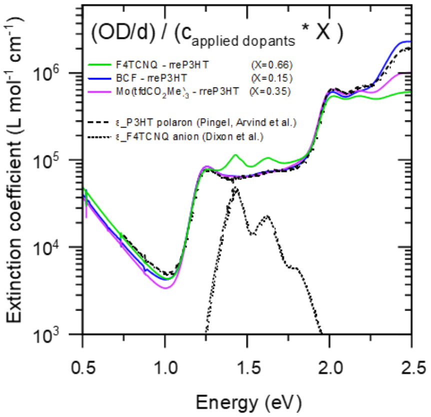

Figure A.2. Molar extinction coefficient of the reference F_4TCNQ anion (according to ref [150]) and P3HT polaron (according to ref [49]), along with the experimental UV-Vis-NIR spectra of the doped solutions that have been rescaled with the appropriate ionization factor (X) to fit the reference curves.

3. UV-Vis-NIR and EPR spectra of the F_4TCNQ radical anion

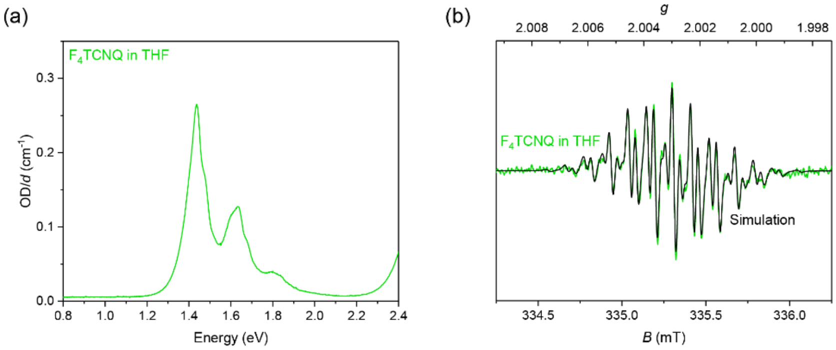

Figure A.3. (a) UV-Vis-NIR spectrum of F_4TCNQ dissolved in THF (ca. 0.5 g L^{-1}) showing the characteristic absorption peaks of the radical anion. (b) X-band room temperature continuous wave EPR spectrum of F_4TCNQ in THF and the corresponding simulation performed for a g-value of 2.00295, four equivalent ^{14}N (I = 1) nuclei with an isotropic hyperfine coupling of 3.11 MHz and four equivalent ^{19}F (I = ½) nuclei with an isotropic hyperfine coupling of 4.26 MHz.

4. Influence of time and illumination on HTFSI-doped rraP3HT

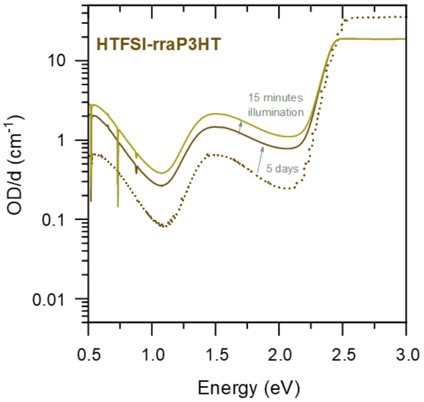

Figure A.4. UV-Vis-NIR absorption spectra of a HTFSI-doped rraP3HT solution (in chloroform) measured initially (brown dotted line), 5 days after preparation (brown solid line), and after 15 minutes of subsequent illumination. The spectra correspond to measurements on the same solution sample.

5. Spin concentration in doped P3HT solutions

Table A.1. Spin concentration (from EPR spectra) in doped rre- and rraP3HT solutions used for estimating the molar extinction coefficient of P3HT polarons shown in Figure 5.9.

Solution	N_{spins} (in 25 µL)	N_{spins} (L^{-1})
rreP3HT – F_4TCNQ	1.94×10^{15}	7.76×10^{19}
rreP3HT – Mo(tfd-CO_2Me)$_3$	9.79×10^{14}	3.92×10^{19}
rreP3HT – BCF	2.09×10^{14}	8.36×10^{18}
1:100 BCF – rraP3HT	4.2×10^{12}	1.7×10^{17}
1:10 BCF – rraP3HT	1.5×10^{13}	6.0×10^{17}
HTFSI – rraP3HT (Sample 1)	6.9×10^{13}	2.8×10^{18}
HTFSI – rraP3HT (Sample 2)	1.6×10^{13}	6.4×10^{17}

Quantitative analysis was done by comparing the double integral of the experimental spectrum with that of a reference sample of known spin concentration (TEMPOL, stable nitroxide radical, in toluene), taking the experimental settings and the Q-factor of the resonator into account. Further details about the analysis procedure can be found in our corresponding joint publication[146].

6. Influence of illumination on the EPR spectra of BCF-doped P3HT solutions

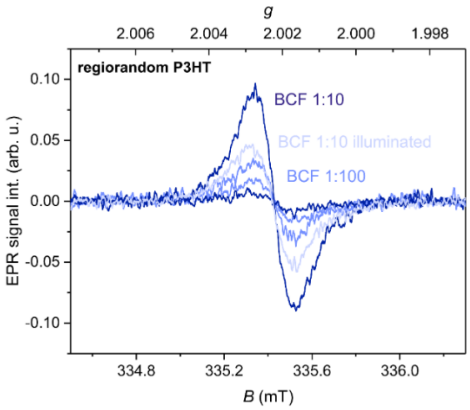

Figure A.5. X-band room temperature cw EPR spectra recorded on solutions of BCF-doped rraP3HT in CF, at doping ratios of 1:100 and 1:10 on two occasions each, and of a 1:10 solution illuminated by white light. The signal intensities are normalized by Q-factor for comparison of the spectral intensities.

7. TDDFT results on protonated nT

Time-dependent density-functional theory (TDDFT) calculations were made using the package Gaussian16.[217] The cc-pVTZ basis set was used in the calculations of protonated oligothiophene. The exchange-correlation potential was approximated with the range-separated CAM-B3LYP hybrid functional.[218] The dispersion interactions were accounted for using the Grimme DFT-D3 scheme.[219] All structures were relaxed until the residual forces were smaller than 10^{-5} Ha/bohr. The solvent was treated implicitly using the polarizable continuum model (PCM)[220] with values of the dielectric constants ε_0=78.36 and ε_∞=1.78 for water, and ε_0=4.71 and ε_∞=2.09 for chloroform.

Figure A.6a shows the simulated absorption spectra of the pristine and protonated 4T oligomer. In the latter, two different protonation sites on the central C_α and C_β are considered.

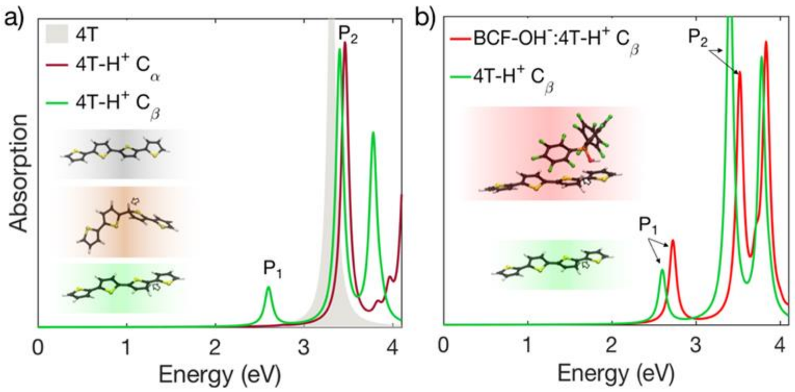

Figure A.6. TDDFT estimated absorption spectra of (a) pristine 4T oligomer (gray shaded area) and of the protonated 4T oligomer at the C_α (brown) and C_β site (green), and (b) protonated 4T doped by the BCF:OH$^-$ complex (red) and of 4T-H+:Cβ (green). A Lorentzian broadening of 100 meV is applied to all the spectra.

Table A.2. The energy, oscillator strength (OS), and composition of the lowest excitations in the TDDFT-estimated absorption spectra of pristine, protonated and charged

System	Energy (eV)	OS	Composition (weight)
4T	3.31	1.28	H → L (93%)
4T-H$^+$ C_α	2.76	< 10^{-3}	H → L (91%)
	3.46	0.79	H-2 → L (57%) H-3 → L (33%)
4T-H$^+$ C_β	2.60	0.11	H → L (79%)
	3.40	0.77	H-1 → L (64%) H → L (14%)
BCF-OH$^-$: 4T-H$^+$ C_β	2.72	0.17	H → L (76%)
	3.52	0.50	H-3 → L (36%) H → L (17%) H-6 → L (14%)
10 T	2.16	3.82	H → L (60%) H-1 → L+1 (28%) H-2→ L+2 (16%)
10T-H$^+$ C_α	2.18	2.19	H-1 → L (82%)
	2.55	< 10^{-2}	H → L (74%)

8. Temperature dependent UV-Vis-NIR spectra of BCF-doped rreP3HT

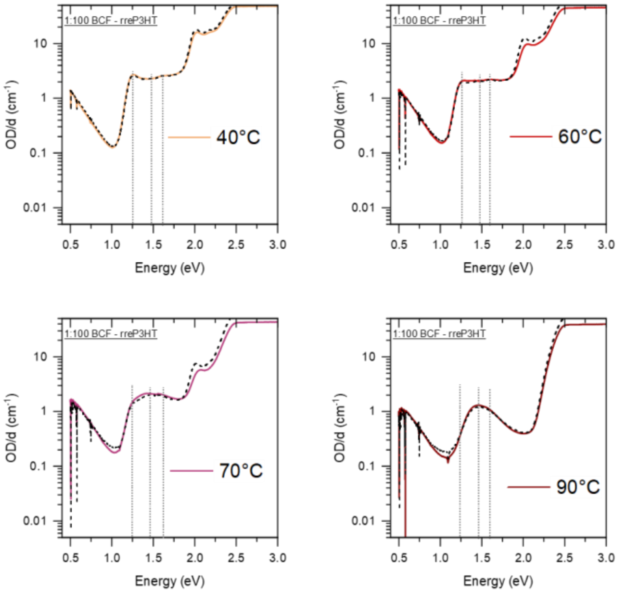

Figure A.7. Experimental and reconstructed UV-Vis-NIR spectra of BCF-doped rreP3HT at select temperatures. The fit parameters are given in Table 5.2

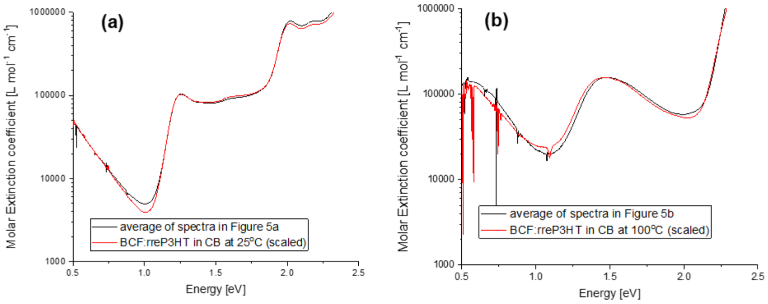

Figure A.8. Comparison of the molar extinction spectra of the delocalized and localized polaron (from Figure 5.9a,b) and the absorption spectra of the BCF-doped rreP3HT solution in CB at (a) 25 °C and (b) 100 °C.

9. Ionization efficiency of F$_4$TCNQ with rreP3HT in chloroform vs. chlorobenzene

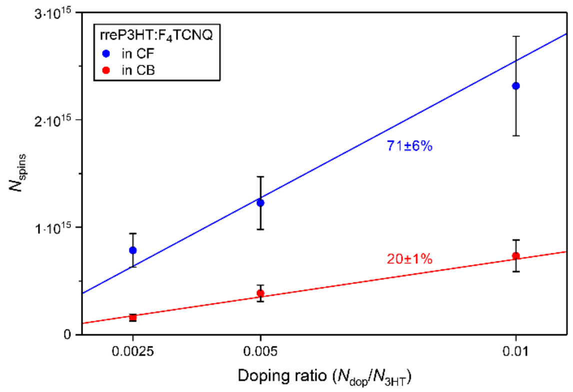

Figure A.9. Spin concentration in F$_4$TCNQ-doped rreP3HT solution for different doping ratios in CF and CB, determined by EPR spectroscopy.

10. Temperature dependent UV-Vis-NIR spectra of F$_4$TCNQ-doped rreP3HT in CB

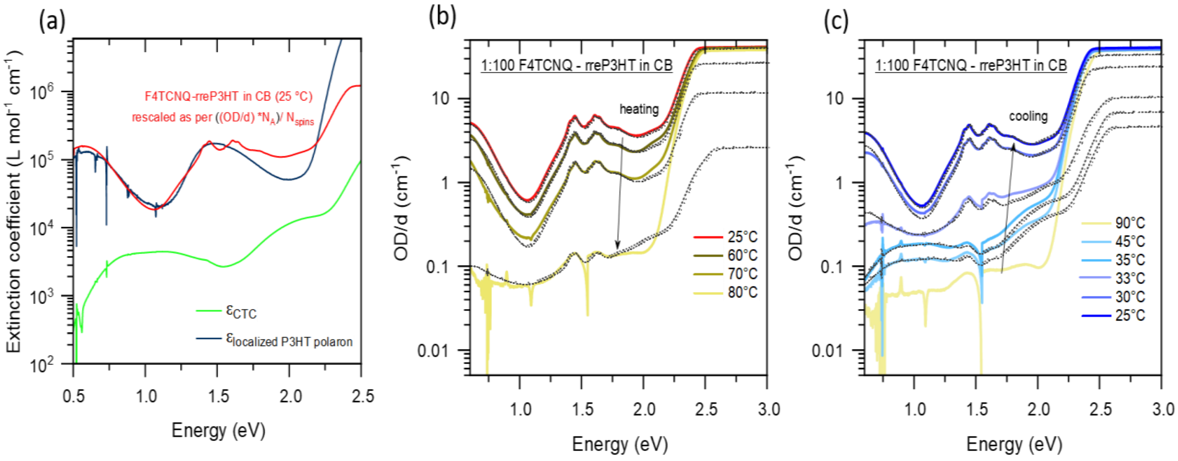

Figure A.10. a) Reference extinction coefficient spectra of the $\text{CTC}_{\text{F4TCNQ-P3HT}}$ (green), localized P3HT polaron (dark blue), and the rescaled 1:100 F$_4$TCNQ-doped rreP3HT (25°C in CB); Absorption spectra of 1:100 F$_4$TCNQ-doped rreP3HT (in CB) recorded during the b) heating cycle and c) cooling cycle. Dotted lines show reconstructed fits for selected temperatures using the extinction coefficient spectra (in (a)).

As shown in Figure A.10a, the rescaled optical spectrum[aa] of F_4TCNQ-rreP3HT in CB coincides well with the localized polaron spectrum, indicating that this dopant:host system predominantly consists of localized P3HT polarons (and the F_4TCNQ counterions) in CB. Therefore, for the fitted spectra shown in Figure A.10b and c, we considered the weighted summation of the rescaled spectrum and the CTC. The fit parameters are shown in Table A.3.

Table A.3. Fit parameters for the reconstructed spectra of the temperature dependent F_4TCNQ-doped rreP3HT in CB shown in Figure A.10b,c.

Solution Temperature	Fraction of added F4TCNQ resulting in,	
	localized P3HT polarons (%)	CTCs (%)
25°C	27	0
60°C	18	0
70°C	8	0
80°C	0.5	10
45°C	0.2	23
35°C	0.2	35
33°C	2.2	26
30°C	15	10
25°C	22	5

[aa] Measured optical spectrum divided by the corresponding spin concentration of P3HT polarons (~ 2×10^{19} L^{-1}) in the solution (obtained from EPR spectroscopy)

B. Appendix for Chapter-6:

1. Integrated intensity from GIXRD images

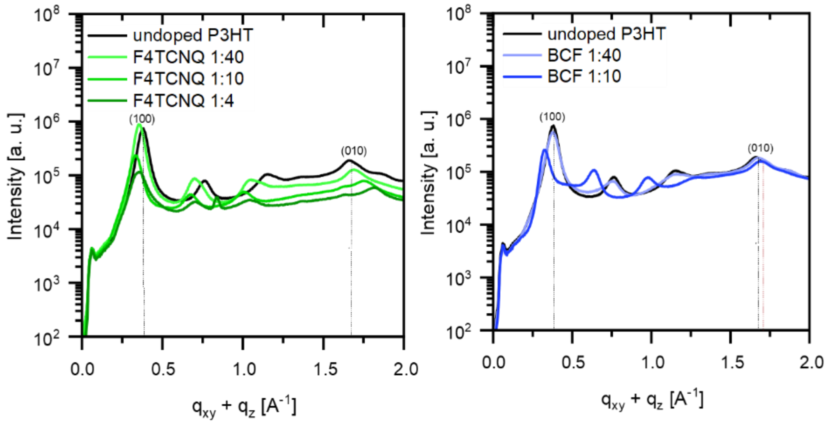

Figure B.1. Integrated intensity of mixed solution F_4TCNQ and BCF-doped rreP3HT films

2. Preliminary ENDOR results of doped rreP3HT films

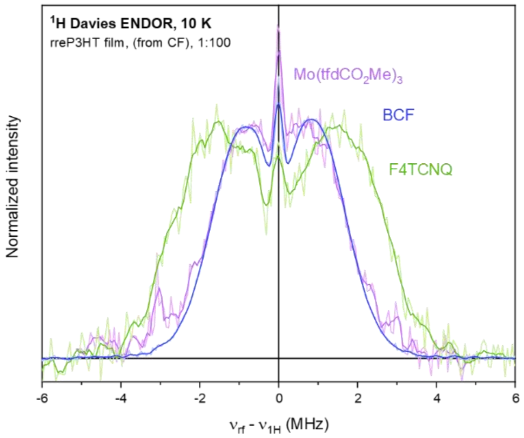

Figure B.2. Q-band ^{1}H Davies ENDOR spectra of frozen films of rreP3HT doped with F_4TCNQ, BCF or Mo(tfd-$CO_2Me)_3$ at doping ratios of 1:100 measured at a temperature of 10 K.

3. AFM images of BCF-doped rraP3HT films

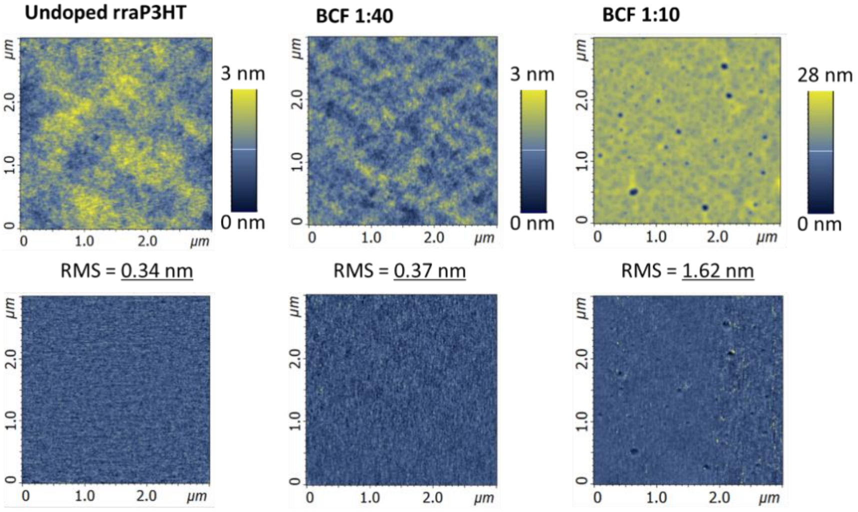

Figure B.3. Topography (top) and phase (bottom) AFM images of undoped and BCF-doped rraP3HT films prepared via mixed solution doping, from CF solutions.

4. Sequential spin coating

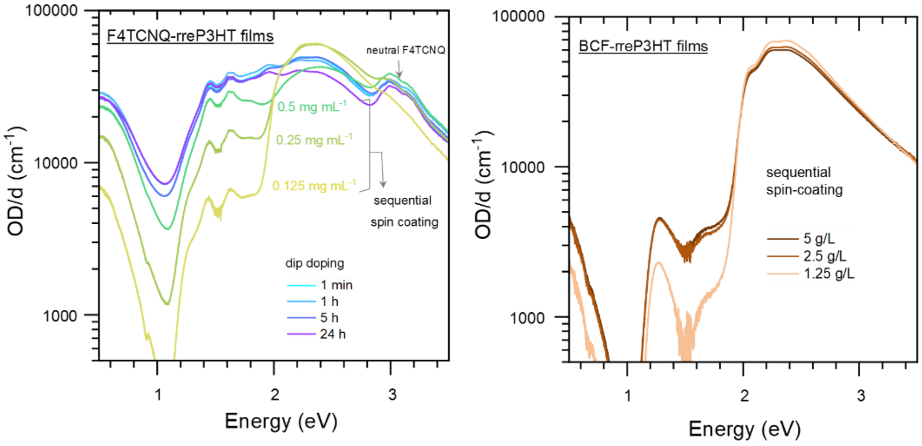

Figure B.4. UV-Vis-NIR spectra of films of F$_4$TCNQ-doped rreP3HT prepared by sequential spin coating and dip doping (right), and sequential spin-coated BCF-doped rreP3HT (left). In this case, the undoped P3HT films were cast from CB. However, for subsequent work shown in Chapter-6 and here, CF was used as the solvent.

5. Photoluminescence spectra of dip-doped BCF-rreP3HT films

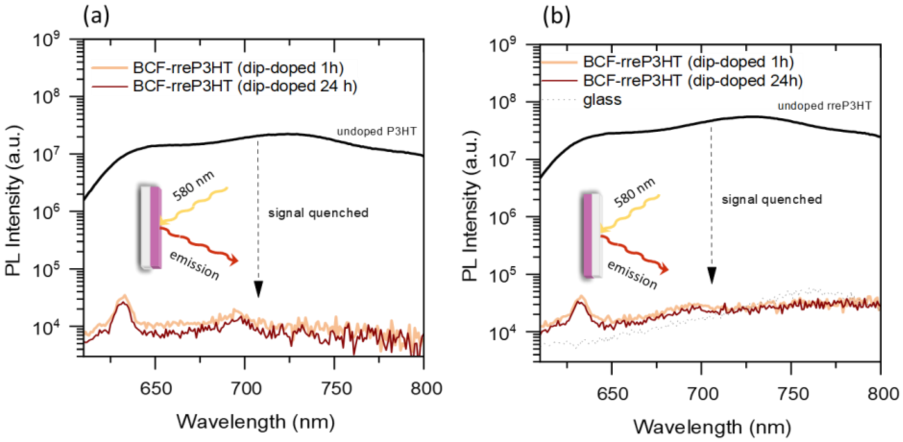

Figure B.5. Photoluminescence (PL) intensity of ca. 280 nm thick films of undoped rreP3HT, 1 h dip doped and 24 h dip doped BCF – P3HT films, measured from the film side (a), and from the glass-side (b), as depicted in the inset. The higher signal intensity in the doped films around 750 nm in (b) is due to the strong emission from glass (grey spectrum) in this region.

Bibliography

1. Evans, D. *The Internet of Things: How the Next Evolution of the Internet Is Changing Everything*; CISCO White Paper, 2011.
2. Someya, T.; Bao, Z.; Malliaras, G. G., The Rise of Plastic Bioelectronics. *Nature* **2016**, *540*, 379.
3. Fitzgerald, A. M., The Internet of Disposable Things Will Be Made of Paper and Plastic Sensors. *IEEE Spectrum* **2018**.
4. infinityPV Heli-on - the World's Most Compact Solar Charger. https://infinitypv.com/products/consumer/heli-on (accessed 22nd October 2019).
5. Takeda, Y.; Hayasaka, K.; Shiwaku, R.; Yokosawa, K.; Shiba, T.; Mamada, M.; Kumaki, D.; Fukuda, K.; Tokito, S., Fabrication of Ultra-Thin Printed Organic Tft Cmos Logic Circuits Optimized for Low-Voltage Wearable Sensor Applications. *Scientific Reports* **2016**, *6*, 25714.
6. Bohn, D. Hands-on with the Samsung Galaxy Fold: More Than Just a Concept. https://www.theverge.com/2019/4/15/18311109/samsung-galaxy-fold-photos-video-foldable-screen-phone-hands-on-impressions (accessed 22nd October 2019).
7. Mertens, R. Lg Display Aims to Produce Rollable Oled Tvs by 2020. https://www.oled-info.com/lgd-aims-produce-rollable-oled-tvs-2020 (accessed 22nd October 2019).
8. Geoghegan, M.; Hadziioannou, G., *Polymer Electronics*; OUP Oxford, 2013.
9. Shirakawa, H.; Louis, E. J.; MacDiarmid, A. G.; Chiang, C. K.; Heeger, A. J., Synthesis of Electrically Conducting Organic Polymers: Halogen Derivatives of Polyacetylene, (Ch). *J. Chem. Soc., Chem. Commun.* **1977**, 578-580.
10. The Nobel Prize in Chemistry 2000. https://www.nobelprize.org/prizes/chemistry/2000/summary/ (accessed 17 Oct 2019).
11. Clevios™ - Pedot:Pss. https://www.heraeus.com/en/hep/products_hep/clevios/clevios_prod/clevios_1.html (accessed 6th May 2020).
12. Hsin-Fei, M., *Polymer Electronics*; Jenny Stanford Publishing, 2013.

13. Lüssem, B.; Riede, M.; Leo, K., Doping of Organic Semiconductors. *Phys. Status Solidi A* **2013**, *210*, 9-43.

14. Abdou, M. S. A.; Holdcroft, S., Mechanisms of Photodegradation of Poly(3-Alkylthiophenes) in Solution. *Macromolecules* **1993**, *26*, 2954-2962.

15. Maliakal, A.; Raghavachari, K.; Katz, H.; Chandross, E.; Siegrist, T., Photochemical Stability of Pentacene and a Substituted Pentacene in Solution and in Thin Films. *Chem. Mater.* **2004**, *16*, 4980-4986.

16. Kawano, K.; Pacios, R.; Poplavskyy, D.; Nelson, J.; Bradley, D. D. C.; Durrant, J. R., Degradation of Organic Solar Cells Due to Air Exposure. *Sol. Energy Mater. Sol. Cells* **2006**, *90*, 3520-3530.

17. Norrman, K.; Madsen, M. V.; Gevorgyan, S. A.; Krebs, F. C., Degradation Patterns in Water and Oxygen of an Inverted Polymer Solar Cell. *J. Am. Chem. Soc.* **2010**, *132*, 16883-16892.

18. Jørgensen, M.; Norrman, K.; Gevorgyan, S. A.; Tromholt, T.; Andreasen, B.; Krebs, F. C., Stability of Polymer Solar Cells. *Adv. Mater.* **2012**, *24*, 580-612.

19. Curry, J.; Cassidy, E. P., Effect of Halogens on the Resistance of Single Crystals of Copper Phthalocyanine. *J. Chem. Phys.* **1962**, *37*, 2154-2155.

20. Yamamoto, Y.; Yoshino, K.; Inuishi, Y., Electrical Properties of Phthalocyanine-Halogen Complexes. *J. Phys. Soc. Jpn.* **1979**, *47*, 1887-1891.

21. Kido, J.; Matsumoto, T., Bright Organic Electroluminescent Devices Having a Metal-Doped Electron-Injecting Layer. *Appl. Phys. Lett.* **1998**, *73*, 2866-2868.

22. Jun, E.; Toshio, M.; Junji, K., Organic Electroluminescent Devices Having Metal Complexes as Cathode Interface Layer. *Jpn. J. Appl. Phys.* **2002**, *41*, L800.

23. Parthasarathy, G.; Shen, C.; Kahn, A.; Forrest, S. R., Lithium Doping of Semiconducting Organic Charge Transport Materials. *J. Appl. Phys.* **2001**, *89*, 4986-4992.

24. Walzer, K.; Maennig, B.; Pfeiffer, M.; Leo, K., Highly Efficient Organic Devices Based on Electrically Doped Transport Layers. *Chem. Rev.* **2007**, *107*, 1233-1271.

25. Jacobs Ian, E.; Moulé Adam, J., Controlling Molecular Doping in Organic Semiconductors. *Adv. Mater.* **2017**, *29*, 1703063.

26. Selzer, F.; Falkenberg, C.; Hamburger, M.; Baumgarten, M.; Müllen, K.; Leo, K.; Riede, M., Improved Organic P-I-N Type Solar Cells with N-Doped Fluorinated

Hexaazatrinaphthylene Derivatives Hatna-F6 and Hatna-F12 as Transparent Electron Transport Material. *J. Appl. Phys.* **2014**, *115*, 054515.

27. Maennig, B., et al., Organic P-I-N Solar Cells. *Appl. Phys. A* **2004**, *79*, 1-14.
28. Murawski, C.; Fuchs, C.; Hofmann, S.; Leo, K.; Gather, M. C., Alternative P-Doped Hole Transport Material for Low Operating Voltage and High Efficiency Organic Light-Emitting Diodes. *Appl. Phys. Lett.* **2014**, *105*, 113303.
29. Wei, P.; Oh, J. H.; Dong, G.; Bao, Z., Use of a 1h-Benzoimidazole Derivative as an N-Type Dopant and to Enable Air-Stable Solution-Processed N-Channel Organic Thin-Film Transistors. *J. Am. Chem. Soc.* **2010**, *132*, 8852-8853.
30. Lüssem, B.; Tietze, M. L.; Kleemann, H.; Hoßbach, C.; Bartha, J. W.; Zakhidov, A.; Leo, K., Doped Organic Transistors Operating in the Inversion and Depletion Regime. *Nat. Commun.* **2013**, *4*, 2775-2775.
31. Lüssem, B.; Keum, C.-M.; Kasemann, D.; Naab, B.; Bao, Z.; Leo, K., Doped Organic Transistors. *Chem. Rev.* **2016**, *116*, 13714-13751.
32. Luo, J.; Xia, J.; Yang, H.; Chen, L.; Wan, Z.; Han, F.; Malik, H. A.; Zhu, X.; Jia, C., Toward High-Efficiency, Hysteresis-Less, Stable Perovskite Solar Cells: Unusual Doping of a Hole-Transporting Material Using a Fluorine-Containing Hydrophobic Lewis Acid. *Energy & Environmental Science* **2018**, *11*, 2035-2045.
33. Kwon, H., et al., Towards Efficient and Stable Perovskite Solar Cells Employing Non-Hygroscopic F4-TCNQ Doped Tfb as the Hole-Transporting Material. *Nanoscale* **2019**, *11*, 19586-19594.
34. Jung, M.-C.; Raga, S. R.; Ono, L. K.; Qi, Y., Substantial Improvement of Perovskite Solar Cells Stability by Pinhole-Free Hole Transport Layer with Doping Engineering. *Scientific Reports* **2015**, *5*, 9863.
35. Pellaroque, A.; Noel, N. K.; Habisreutinger, S. N.; Zhang, Y.; Barlow, S.; Marder, S. R.; Snaith, H. J., Efficient and Stable Perovskite Solar Cells Using Molybdenum Tris(Dithiolene)S as P-Dopants for Spiro-Ometad. *ACS Energy Letters* **2017**, *2*, 2044-2050.
36. Pingel, P.; Neher, D., Comprehensive Picture of P-Type Doping of P3HT with the Molecular Acceptor F4TCNQ. *Phys. Rev. B* **2013**, *87*, 115209.
37. Salzmann, I., et al., Intermolecular Hybridization Governs Molecular Electrical Doping. *Phys. Rev. Lett.* **2012**, *108*, 035502.

38. Thomas, E. M.; Davidson, E. C.; Katsumata, R.; Segalman, R. A.; Chabinyc, M. L., Branched Side Chains Govern Counterion Position and Doping Mechanism in Conjugated Polythiophenes. *ACS Macro Lett.* **2018**, *7*, 1492-1497.
39. Neelamraju, B.; Watts, K. E.; Pemberton, J. E.; Ratcliff, E. L., Correlation of Coexistent Charge Transfer States in F4TCNQ-Doped P3HT with Microstructure. *J. Phys. Chem. Lett.* **2018**, *9*, 6871-6877.
40. Jacobs, I. E.; Aasen, E. W.; Oliveira, J. L.; Fonseca, T. N.; Roehling, J. D.; Li, J.; Zhang, G.; Augustine, M. P.; Mascal, M.; Moule, A. J., Comparison of Solution-Mixed and Sequentially Processed P3HT:F4TCNQ Films: Effect of Doping-Induced Aggregation on Film Morphology. *J. Mater. Chem. C* **2016**, *4*, 3454-3466.
41. Scholes, D. T.; Hawks, S. A.; Yee, P. Y.; Wu, H.; Lindemuth, J. R.; Tolbert, S. H.; Schwartz, B. J., Overcoming Film Quality Issues for Conjugated Polymers Doped with F4TCNQ by Solution Sequential Processing: Hall Effect, Structural, and Optical Measurements. *J. Phys. Chem. Lett.* **2015**, *6*, 4786-4793.
42. Li, J.; Rochester, C. W.; Jacobs, I. E.; Friedrich, S.; Stroeve, P.; Riede, M.; Moulé, A. J., Measurement of Small Molecular Dopant F4TCNQ and C60f36 Diffusion in Organic Bilayer Architectures. *ACS Appl. Mater. Interfaces* **2015**, *7*, 28420-28428.
43. Welch, G. C.; Coffin, R.; Peet, J.; Bazan, G. C., Band Gap Control in Conjugated Oligomers Via Lewis Acids. *J. Am. Chem. Soc.* **2009**, *131*, 10802-10803.
44. Welch, G. C.; Bazan, G. C., Lewis Acid Adducts of Narrow Band Gap Conjugated Polymers. *J. Am. Chem. Soc.* **2011**, *133*, 4632-4644.
45. Zalar, P.; Kuik, M.; Henson, Z. B.; Woellner, C.; Zhang, Y.; Sharenko, A.; Bazan, G. C.; Nguyen, T.-Q., Increased Mobility Induced by Addition of a Lewis Acid to a Lewis Basic Conjugated Polymer. *Adv. Mater.* **2014**, *26*, 724-727.
46. Yan, H.; Chen, J.; Zhou, K.; Tang, Y.; Meng, X.; Xu, X.; Ma, W., Lewis Acid Doping Induced Synergistic Effects on Electronic and Morphological Structure for Donor and Acceptor in Polymer Solar Cells. *Advanced Energy Materials* **2018**, *0*, 1703672.
47. Panidi, J.; Paterson, A. F.; Khim, D.; Fei, Z.; Han, Y.; Tsetseris, L.; Vourlias, G.; Patsalas, P. A.; Heeney, M.; Anthopoulos, T. D., Remarkable Enhancement of the Hole Mobility in Several Organic Small-Molecules, Polymers, and Small-Molecule:Polymer Blend

Transistors by Simple Admixing of the Lewis Acid P-Dopant B(C6F5)3. *Adv. Sci.* **2018**, *5*, 1700290.

48. Arvind, M. Mechanisms of Molecular P-Doping of Semiconducting Polymers. Master thesis, Universität Potsdam, 2015.
49. Pingel, P.; Arvind, M.; Kölln, L.; Steyrleuthner, R.; Kraffert, F.; Behrends, J.; Janietz, S.; Neher, D., P-Type Doping of Poly(3-Hexylthiophene) with the Strong Lewis Acid Tris(Pentafluorophenyl)Borane. *Adv. Electron. Mater.* **2016**, *2*, 1600204.
50. Qi, Y.; Sajoto, T.; Barlow, S.; Kim, E.-G.; Brédas, J.-L.; Marder, S. R.; Kahn, A., Use of a High Electron-Affinity Molybdenum Dithiolene Complex to P-Dope Hole-Transport Layers. *J. Am. Chem. Soc.* **2009**, *131*, 12530-12531.
51. Dai, A., et al., Enhanced Charge-Carrier Injection and Collection Via Lamination of Doped Polymer Layers P-Doped with a Solution-Processible Molybdenum Complex. *Adv. Funct. Mater.* **2014**, *24*, 2197-2204.
52. Scharsich, C.; Lohwasser, R. H.; Sommer, M.; Asawapirom, U.; Scherf, U.; Thelakkat, M.; Neher, D.; Köhler, A., Control of Aggregate Formation in Poly(3-Hexylthiophene) by Solvent, Molecular Weight, and Synthetic Method. *J. Polym. Sci., Part B: Polym. Phys.* **2012**, *50*, 442-453.
53. Khlaifia, D.; Ewels, C. P.; Massuyeau, F.; Chemek, M.; Faulques, E.; Duvail, J.-L.; Alimi, K., Unraveling the Real Structures of Solution-Based and Surface-Bound Poly(3-Hexylthiophene) (P3HT) Oligomers: A Combined Theoretical and Experimental Study. *RSC Adv.* **2016**, *6*, 56174-56182.
54. Sirringhaus, H., et al., Two-Dimensional Charge Transport in Self-Organized, High-Mobility Conjugated Polymers. *Nature* **1999**, *401*, 685-688.
55. Ludwigs, S., *P3HT Revisited – from Molecular Scale to Solar Cell Devices*; Springer Berlin Heidelberg, 2014.
56. Ihn, K. J.; Moulton, J.; Smith, P., Whiskers of Poly(3-Alkylthiophene)S. *J. Polym. Sci., Part B: Polym. Phys.* **1993**, *31*, 735-742.
57. Zen, A.; Pflaum, J.; Hirschmann, S.; Zhuang, W.; Jaiser, F.; Asawapirom, U.; Rabe, J. P.; Scherf, U.; Neher, D., Effect of Molecular Weight and Annealing of Poly(3-Hexylthiophene)S on the Performance of Organic Field-Effect Transistors. *Adv. Funct. Mater.* **2004**, *14*, 757-764.

58. Méndez, H., et al., Charge-Transfer Crystallites as Molecular Electrical Dopants. *Nat. Commun.* **2015**, *6*, 8560.
59. Müller, L., et al., Charge-Transfer–Solvent Interaction Predefines Doping Efficiency in P-Doped P3HT Films. *Chem. Mater.* **2016**, *28*, 4432-4439.
60. Köhler, A.; Bässler, H., *Electronic Processes in Organic Semiconductors: An Introduction*; Wiley, 2015.
61. Brinkmann, M., Structure and Morphology Control in Thin Films of Regioregular Poly(3-Hexylthiophene). *J. Polym. Sci., Part B: Polym. Phys.* **2011**, *49*, 1218-1233.
62. Peierls, R. E.; Rudolf Ernst Peierls, S. R. E. P.; Peierls, R. S.; Press, O. U., *Quantum Theory of Solids*; Clarendon Press, 1955.
63. Himmelberger, S.; Duong, D. T.; Northrup, J. E.; Rivnay, J.; Koch, F. P. V.; Beckingham, B. S.; Stingelin, N.; Segalman, R. A.; Mannsfeld, S. C. B.; Salleo, A., Role of Side-Chain Branching on Thin-Film Structure and Electronic Properties of Polythiophenes. *Adv. Funct. Mater.* **2015**, *25*, 2616-2624.
64. Zaumseil, J., P3HT and Other Polythiophene Field-Effect Transistors. In *P3HT Revisited – from Molecular Scale to Solar Cell Devices*, Ludwigs, S., Ed. Springer Berlin Heidelberg: Berlin, Heidelberg, 2014; pp 107-137.
65. Donley, C. L.; Zaumseil, J.; Andreasen, J. W.; Nielsen, M. M.; Sirringhaus, H.; Friend, R. H.; Kim, J.-S., Effects of Packing Structure on the Optoelectronic and Charge Transport Properties in Poly(9,9-Di-N-Octylfluorene-Alt-Benzothiadiazole). *J. Am. Chem. Soc.* **2005**, *127*, 12890-12899.
66. Zhang, R., et al., Nanostructure Dependence of Field-Effect Mobility in Regioregular Poly(3-Hexylthiophene) Thin Film Field Effect Transistors. *J. Am. Chem. Soc.* **2006**, *128*, 3480-3481.
67. Verilhac, J.-M.; LeBlevennec, G.; Djurado, D.; Rieutord, F.; Chouiki, M.; Travers, J.-P.; Pron, A., Effect of Macromolecular Parameters and Processing Conditions on Supramolecular Organisation, Morphology and Electrical Transport Properties in Thin Layers of Regioregular Poly(3-Hexylthiophene). *Synth. Met.* **2006**, *156*, 815-823.
68. Kline, R. J.; McGehee, M. D.; Kadnikova, E. N.; Liu, J.; Fréchet, J. M. J.; Toney, M. F., Dependence of Regioregular Poly(3-Hexylthiophene) Film Morphology and Field-Effect Mobility on Molecular Weight. *Macromolecules* **2005**, *38*, 3312-3319.

69. Dang, M. T.; Hirsch, L.; Wantz, G.; Wuest, J. D., Controlling the Morphology and Performance of Bulk Heterojunctions in Solar Cells. Lessons Learned from the Benchmark Poly(3-Hexylthiophene):[6,6]-Phenyl-C61-Butyric Acid Methyl Ester System. *Chem. Rev.* **2013**, *113*, 3734-3765.

70. Chang, J.-F.; Sun, B.; Breiby, D. W.; Nielsen, M. M.; Sölling, T. I.; Giles, M.; McCulloch, I.; Sirringhaus, H., Enhanced Mobility of Poly(3-Hexylthiophene) Transistors by Spin-Coating from High-Boiling-Point Solvents. *Chem. Mater.* **2004**, *16*, 4772-4776.

71. Park, Y. D.; Lee, H. S.; Choi, Y. J.; Kwak, D.; Cho, J. H.; Lee, S.; Cho, K., Solubility-Induced Ordered Polythiophene Precursors for High-Performance Organic Thin-Film Transistors. *Adv. Funct. Mater.* **2009**, *19*, 1200-1206.

72. Lu, G. H.; Li, L. G.; Yang, X. N., Achieving Perpendicular Alignment of Rigid Polythiophene Backbones to the Substrate by Using Solvent-Vapor Treatment. *Adv. Mater.* **2007**, *19*, 3594-3598.

73. Crossland, E. J. W.; Rahimi, K.; Reiter, G.; Steiner, U.; Ludwigs, S., Systematic Control of Nucleation Density in Poly(3-Hexylthiophene) Thin Films. *Adv. Funct. Mater.* **2011**, *21*, 518-524.

74. McCulloch, I., et al., Liquid-Crystalline Semiconducting Polymers with High Charge-Carrier Mobility. *Nat. Mater.* **2006**, *5*, 328-333.

75. Cho, S.; Lee, K.; Yuen, J.; Wang, G.; Moses, D.; Heeger, A. J.; Surin, M.; Lazzaroni, R., Thermal Annealing-Induced Enhancement of the Field-Effect Mobility of Regioregular Poly(3-Hexylthiophene) Films. *J. Appl. Phys.* **2006**, *100*, 114503.

76. Tietze, M. L. Molecular Doping Processes in Organic Semiconductors Investigated by Photoelectron Spectroscopy. Dresden, 2014.

77. Warta, W.; Karl, N., Hot Holes in Naphthalene: High, Electric-Field-Dependent Mobilities. *Phys. Rev. B* **1985**, *32*, 1172-1182.

78. Sakanoue, T.; Sirringhaus, H., Band-Like Temperature Dependence of Mobility in A solution-Processed Organic Semiconductor. *Nat. Mater.* **2010**, *9*, 736-740.

79. Bässler, H., Charge Transport in Disordered Organic Photoconductors a Monte Carlo Simulation Study. *physica status solidi (b)* **1993**, *175*, 15-56.

80. Jacoboni, C.; Canali, C.; Ottaviani, G.; Alberigi Quaranta, A., A Review of Some Charge Transport Properties of Silicon. *Solid·State Electron.* **1977**, *20*, 77-89.

81. Nitta, J.; Miwa, K.; Komiya, N.; Annese, E.; Fujii, J.; Ono, S.; Sakamoto, K., The Actual Electronic Band Structure of a Rubrene Single Crystal. *Scientific Reports* **2019**, *9*, 9645.

82. Coropceanu, V.; Cornil, J.; da Silva Filho, D. A.; Olivier, Y.; Silbey, R.; Brédas, J.-L., Charge Transport in Organic Semiconductors. *Chem. Rev.* **2007**, *107*, 926-952.

83. Salzmann, I.; Heimel, G.; Oehzelt, M.; Winkler, S.; Koch, N., Molecular Electrical Doping of Organic Semiconductors: Fundamental Mechanisms and Emerging Dopant Design Rules. *Acc. Chem. Res.* **2016**, *49*, 370-378.

84. Müller, L. On the Correlation between Structural Order and Molecular Doping in Semiconducting Polymers. Universität Heidelberg, Heidelberg, 2018.

85. Jacobs, I. E.; Cendra, C.; Harrelson, T. F.; Bedolla Valdez, Z. I.; Faller, R.; Salleo, A.; Moulé, A. J., Polymorphism Controls the Degree of Charge Transfer in a Molecularly Doped Semiconducting Polymer. *Mater. Horiz.* **2018**, *5*, 655-660.

86. Melby, L. R.; Harder, R. J.; Hertler, W. R.; Mahler, W.; Benson, R. E.; Mochel, W. E., Substituted Quinodimethans. Ii. Anion-Radical Derivatives and Complexes of 7,7,8,8-Tetracyanoquinodimethan. *J. Am. Chem. Soc.* **1962**, *84*, 3374-3387.

87. Gao, W.; Kahn, A., Controlled P-Doping of Zinc Phthalocyanine by Coevaporation with Tetrafluorotetracyanoquinodimethane: A Direct and Inverse Photoemission Study. *Appl. Phys. Lett.* **2001**, *79*, 4040-4042.

88. Gao, Z. Q.; Mi, B. X.; Xu, G. Z.; Wan, Y. Q.; Gong, M. L.; Cheah, K. W.; Chen, C. H., An Organic P-Type Dopant with High Thermal Stability for an Organic Semiconductor. *Chem. Commun.* **2008**, 117-119.

89. Hase, H.; O'Neill, K.; Frisch, J.; Opitz, A.; Koch, N.; Salzmann, I., Unraveling the Microstructure of Molecularly Doped Poly(3-Hexylthiophene) by Thermally Induced Dedoping. *J. Phys. Chem. C* **2018**, *122*, 25893-25899.

90. Meerheim, R.; Olthof, S.; Hermenau, M.; Scholz, S.; Petrich, A.; Tessler, N.; Solomeshch, O.; Lüssem, B.; Riede, M.; Leo, K., Investigation of C60f36 as Low-Volatility P-Dopant in Organic Optoelectronic Devices. *J. Appl. Phys.* **2011**, *109*, 103102.

91. Solomeshch, O.; Yu, Y. J.; Goryunkov, A. A.; Sidorov, L. N.; Tuktarov, R. F.; Choi, D. H.; Jin, J.-I.; Tessler, N., Ground-State Interaction and Electrical Doping of Fluorinated C60 in Conjugated Polymers. *Adv. Mater.* **2009**, *21*, 4456-4460.

92. Qi, Y., et al., A Molybdenum Dithiolene Complex as P-Dopant for Hole-Transport Materials: A Multitechnique Experimental and Theoretical Investigation. *Chem. Mater.* **2010**, *22*, 524-531.

93. Mohapatra, S. K.; Zhang, Y.; Sandhu, B.; Fonari, M. S.; Timofeeva, T. V.; Marder, S. R.; Barlow, S., Synthesis, Characterization, and Crystal Structures of Molybdenum Complexes of Unsymmetrical Electron-Poor Dithiolene Ligands. *Polyhedron* **2016**, *116*, 88-95.

94. Piers, W. E.; Chivers, T., Pentafluorophenylboranes: From Obscurity to Applications. *Chem. Soc. Rev.* **1997**, *26*, 345-354.

95. Erker, G., Tris(Pentafluorophenyl)Borane: A Special Boron Lewis Acid for Special Reactions. *Dalton Trans.* **2005**, 1883-1890.

96. Ye, T.; Wang, J.; Chen, W.; Yang, Y.; He, D., Improved Performance and Reproducibility of Perovskite Solar Cells by Well-Soluble Tris(Pentafluorophenyl)Borane as a P-Type Dopant. *ACS Appl. Mater. Interfaces* **2017**, *9*, 17923-17931.

97. Ye, T.; Chen, W.; Jin, S.; Hao, S.; Zhang, X.; Liu, H.; He, D., Enhanced Efficiency of Planar Heterojunction Perovskite Solar Cells by a Light Soaking Treatment on Tris(Pentafluorophenyl)Borane-Doped Poly(Triarylamine) Solution. *ACS Appl. Mater. Interfaces* **2019**, *11*, 14004-14010.

98. Ivory, D. M.; Miller, G. G.; Sowa, J. M.; Shacklette, L. W.; Chance, R. R.; Baughman, R. H., Highly Conducting Charge-Transfer Complexes of Poly(P-Phenylene). *J. Chem. Phys.* **1979**, *71*, 1506-1507.

99. Haddon, R. C., et al., Conducting Films of C60 and C70 by Alkali-Metal Doping. *Nature* **1991**, *350*, 320-322.

100. Ramsey, M. G.; Steinmüller, D.; Netzer, F. P., Explicit Evidence for Bipolaron Formation: Cs-Doped Biphenyl. *Phys. Rev. B* **1990**, *42*, 5902-5905.

101. Nollau, A.; Pfeiffer, M.; Fritz, T.; Leo, K., Controlled N-Type Doping of a Molecular Organic Semiconductor: Naphthalenetetracarboxylic Dianhydride (Ntcda) Doped with Bis(Ethylenedithio)-Tetrathiafulvalene (Bedt-TTF). *J. Appl. Phys.* **2000**, *87*, 4340-4343.

102. Tanaka, S.; Kanai, K.; Kawabe, E.; Iwahashi, T.; Nishi, T.; Ouchi, Y.; Seki, K., Doping Effect of Tetrathianaphthacene Molecule in Organic Semiconductors on Their Interfacial Electronic Structures Studied by Uv Photoemission Spectroscopy. *Jpn. J. Appl. Phys.* **2005**, *44*, 3760-3763.

103. Chan, C. K.; Amy, F.; Zhang, Q.; Barlow, S.; Marder, S.; Kahn, A., N-Type Doping of an Electron-Transport Material by Controlled Gas-Phase Incorporation of Cobaltocene. *Chem. Phys. Lett.* **2006**, *431*, 67-71.

104. Werner, A.; Li, F.; Harada, K.; Pfeiffer, M.; Fritz, T.; Leo, K.; Machill, S., N-Type Doping of Organic Thin Films Using Cationic Dyes. *Adv. Funct. Mater.* **2004**, *14*, 255-260.

105. Li, F.; Werner, A.; Pfeiffer, M.; Leo, K.; Liu, X., Leuco Crystal Violet as a Dopant for N-Doping of Organic Thin Films of Fullerene C60. *The Journal of Physical Chemistry B* **2004**, *108*, 17076-17082.

106. Guo, S.; Mohapatra, S. K.; Romanov, A.; Timofeeva, T. V.; Hardcastle, K. I.; Yesudas, K.; Risko, C.; Brédas, J.-L.; Marder, S. R.; Barlow, S., N-Doping of Organic Electronic Materials Using Air-Stable Organometallics: A Mechanistic Study of Reduction by Dimeric Sandwich Compounds. *Chemistry – A European Journal* **2012**, *18*, 14760-14772.

107. Mohapatra, S. K.; Fonari, A.; Risko, C.; Yesudas, K.; Moudgil, K.; Delcamp, J. H.; Timofeeva, T. V.; Brédas, J.-L.; Marder, S. R.; Barlow, S., Dimers of Nineteen-Electron Sandwich Compounds: Crystal and Electronic Structures, and Comparison of Reducing Strengths. *Chemistry – A European Journal* **2014**, *20*, 15385-15394.

108. Guo, S.; Kim, S. B.; Mohapatra, S. K.; Qi, Y.; Sajoto, T.; Kahn, A.; Marder, S. R.; Barlow, S., N-Doping of Organic Electronic Materials Using Air-Stable Organometallics. *Adv. Mater.* **2012**, *24*, 699-703.

109. Qi, Y.; Mohapatra, S. K.; Bok Kim, S.; Barlow, S.; Marder, S. R.; Kahn, A., Solution Doping of Organic Semiconductors Using Air-Stable N-Dopants. *Appl. Phys. Lett.* **2012**, *100*, 083305.

110. Ostroverkhova, O., *Handbook of Organic Materials for Optical and (Opto)Electronic Devices: Properties and Applications*; Elsevier Science, 2013.

111. Duong, D. T.; Wang, C.; Antono, E.; Toney, M. F.; Salleo, A., The Chemical and Structural Origin of Efficient P-Type Doping in P3HT. *Org. Electron.* **2013**, *14*, 1330-1336.

112. Zhang, Y.; de Boer, B.; Blom Paul, W. M., Controllable Molecular Doping and Charge Transport in Solution-Processed Polymer Semiconducting Layers. *Adv. Funct. Mater.* **2009**, *19*, 1901-1905.

113. Gao, J.; Niles, E. T.; Grey, J. K., Aggregates Promote Efficient Charge Transfer Doping of Poly(3-Hexylthiophene). *J. Phys. Chem. Lett.* **2013**, *4*, 2953-2957.

114. Cochran, J. E.; Junk, M. J. N.; Glaudell, A. M.; Miller, P. L.; Cowart, J. S.; Toney, M. F.; Hawker, C. J.; Chmelka, B. F.; Chabinyc, M. L., Molecular Interactions and Ordering in Electrically Doped Polymers: Blends of Pbttt and F4TCNQ. *Macromolecules* **2014**, *47*, 6836-6846.

115. Bredas, J. L.; Street, G. B., Polarons, Bipolarons, and Solitons in Conducting Polymers. *Acc. Chem. Res.* **1985**, *18*, 309-315.

116. Heeger, A. J.; Kivelson, S.; Schrieffer, J. R.; Su, W. P., Solitons in Conducting Polymers. *Rev. Mod. Phys.* **1988**, *60*, 781-850.

117. Campbell, D. K.; Bishop, A. R.; Fesser, K., Polarons in Quasi-One-Dimensional Systems. *Phys. Rev. B* **1982**, *26*, 6862-6874.

118. Österbacka, R.; An, C. P.; Jiang, X. M.; Vardeny, Z. V., Two-Dimensional Electronic Excitations in Self-Assembled Conjugated Polymer Nanocrystals. *Science* **2000**, *287*, 839.

119. Wang, C.; Duong, D. T.; Vandewal, K.; Rivnay, J.; Salleo, A., Optical Measurement of Doping Efficiency in Poly(3-Hexylthiophene) Solutions and Thin Films. *Phys. Rev. B* **2015**, *91*, 085205.

120. Winkler, S.; Amsalem, P.; Frisch, J.; Oehzelt, M.; Heimel, G.; Koch, N., Probing the Energy Levels in Hole-Doped Molecular Semiconductors. *Mater. Horiz.* **2015**, *2*, 427-433.

121. Heimel, G., The Optical Signature of Charges in Conjugated Polymers. *ACS Cent. Sci.* **2016**, *2*, 309-315.

122. Chia, P.-J.; Sivaramakrishnan, S.; Zhou, M.; Png, R.-Q.; Chua, L.-L.; Friend, R. H.; Ho, P. K. H., Direct Evidence for the Role of the Madelung Potential in Determining the Work Function of Doped Organic Semiconductors. *Phys. Rev. Lett.* **2009**, *102*, 096602.

123. Png, R.-Q.; Ang, M. C. Y.; Teo, M.-H.; Choo, K.-K.; Tang, C. G.; Belaineh, D.; Chua, L.-L.; Ho, P. K. H., Madelung and Hubbard Interactions in Polaron Band Model of Doped Organic Semiconductors. *Nat. Commun.* **2016**, *7*, 11948.

124. Hubbard, J.; Flowers, B. H., Electron Correlations in Narrow Energy Bands. *Proceedings of the Royal Society of London. Series A. Mathematical and Physical Sciences* **1963**, *276*, 238-257.

125. Schwedhelm, R.; Kipp, L.; Dallmeyer, A.; Skibowski, M., Experimental Band Gap and Core-Hole Electron Interaction in Epitaxial C_{60} Films. *Phys. Rev. B* **1998**, *58*, 13176-13180.

126. Frisch, J.; Vollmer, A.; Rabe, J. P.; Koch, N., Ultrathin Polythiophene Films on an Intrinsically Conducting Polymer Electrode: Charge Transfer Induced Valence States and Interface Dipoles. *Org. Electron.* **2011**, *12*, 916-922.

127. Kanai, K.; Akaike, K.; Koyasu, K.; Sakai, K.; Nishi, T.; Kamizuru, Y.; Nishi, T.; Ouchi, Y.; Seki, K., Determination of Electron Affinity of Electron Accepting Molecules. *Appl. Phys. A* **2009**, *95*, 309-313.

128. Brown, P. J.; Sirringhaus, H.; Harrison, M.; Shkunov, M.; Friend, R. H., Optical Spectroscopy of Field-Induced Charge in Self-Organized High Mobility Poly(3-Hexylthiophene). *Phys. Rev. B* **2001**, *63*, 125204.

129. Brabec, C. J.; Dyakonov, V.; Parisi, J.; Sariciftci, N. S., *Organic Photovoltaics: Concepts and Realization*; Springer Berlin Heidelberg, 2013.

130. Kim, Y. H.; Spiegel, D.; Hotta, S.; Heeger, A. J., Photoexcitation and Doping Studies of Poly(3-Hexylthienylene). *Phys. Rev. B* **1988**, *38*, 5490-5495.

131. Meneghetti, M.; Pecile, C., Charge–Transfer Organic Crystals: Molecular Vibrations and Spectroscopic Effects of Electron–Molecular Vibration Coupling of the Strong Electron Acceptor TCNQF4. *J. Chem. Phys.* **1986**, *84*, 4149-4162.

132. Eaton, G. R.; Eaton, S. S.; Barr, D. P.; Weber, R. T., *Quantitative EPR*; Springer Vienna, 2010.

133. Olthof, S. S. Photoelectron Spectroscopy on Doped Organic Semiconductors and Related Interfaces. Technische Universität Dresden, Germany, 2010.

134. Blochwitz, J.; Fritz, T.; Pfeiffer, M.; Leo, K.; Alloway, D. M.; Lee, P. A.; Armstrong, N. R., Interface Electronic Structure of Organic Semiconductors with Controlled Doping Levels. *Org. Electron.* **2001**, *2*, 97-104.

135. Lim, E.; Jung, B.-J.; Chikamatsu, M.; Azumi, R.; Yoshida, Y.; Yase, K.; Do, L.-M.; Shim, H.-K., Doping Effect of Solution-Processed Thin-Film Transistors Based on Polyfluorene. *J. Mater. Chem.* **2007**, *17*, 1416-1420.

136. Duong Duc, T.; Phan, H.; Hanifi, D.; Jo Pil, S.; Nguyen, T. Q.; Salleo, A., Direct Observation of Doping Sites in Temperature-Controlled, P-Doped P3HT Thin Films by Conducting Atomic Force Microscopy. *Adv. Mater.* **2014**, *26*, 6069-6073.

137. Patel, S. N.; Glaudell, A. M.; Peterson, K. A.; Thomas, E. M.; O'Hara, K. A.; Lim, E.; Chabinyc, M. L., Morphology Controls the Thermoelectric Power Factor of a Doped Semiconducting Polymer. *Science Advances* **2017**, *3*, e1700434.

138. Pfeiffer, M.; Beyer, A.; Fritz, T.; Leo, K., Controlled Doping of Phthalocyanine Layers by Cosublimation with Acceptor Molecules: A Systematic Seebeck and Conductivity Study. *Appl. Phys. Lett.* **1998**, *73*, 3202-3204.

139. Pingel, P.; Schwarzl, R.; Neher, D., Effect of Molecular P-Doping on Hole Density and Mobility in Poly(3-Hexylthiophene). *Appl. Phys. Lett.* **2012**, *100*, 143303.

140. Olthof, S.; Singh, S.; Mohapatra, S. K.; Barlow, S.; Marder, S. R.; Kippelen, B.; Kahn, A., Passivation of Trap States in Unpurified and Purified C60 and the Influence on Organic Field-Effect Transistor Performance. *Appl. Phys. Lett.* **2012**, *101*, 253303.

141. Zhang, Y.; de Boer, B.; Blom, P. W. M., Trap-Free Electron Transport in Poly(P-Phenylene Vinylene) by Deactivation of Traps with N-Type Doping. *Phys. Rev. B* **2010**, *81*, 085201.

142. Zuo, G.; Li, Z.; Andersson, O.; Abdalla, H.; Wang, E.; Kemerink, M., Molecular Doping and Trap Filling in Organic Semiconductor Host–Guest Systems. *J. Phys. Chem. C* **2017**, *121*, 7767-7775.

143. Kang, K., et al., 2d Coherent Charge Transport in Highly Ordered conducting Polymers Doped by Solid State diffusion. *Nat. Mater.* **2016**, *15*, 896-902.

144. Clark, J. A Double Beam Uv-Visible Absorption Spectrometer. https://www.chemguide.co.uk/analysis/uvvisible/spectrometer.html (accessed 14th April).

145. Cary 4000/5000/6000i Internal Diffuse Reflectance Accessory Manual.

146. Arvind, M., et al., Quantitative Analysis of Doping-Induced Polarons and Charge-Transfer Complexes of Poly(3-Hexylthiophene) in Solution. *The Journal of Physical Chemistry B* **2020**, *124*, 7694-7708.

147. Lawrence, E. J.; Oganesyan, V. S.; Wildgoose, G. G.; Ashley, A. E., Exploring the Fate of the Tris(Pentafluorophenyl)Borane Radical Anion in Weakly Coordinating Solvents. *Dalton Trans.* **2013**, *42*, 782-789.

148. Guan, Z.-L.; Kim, J. B.; Wang, H.; Jaye, C.; Fischer, D. A.; Loo, Y.-L.; Kahn, A., Direct Determination of the Electronic Structure of the Poly(3-Hexylthiophene):Phenyl-[6,6]-C61 Butyric Acid Methyl Ester Blend. *Org. Electron.* **2010**, *11*, 1779-1785.

149. Ko, S., et al., Controlled Conjugated Backbone Twisting for an Increased Open-Circuit Voltage While Having a High Short-Circuit Current in Poly(Hexylthiophene) Derivatives. *J. Am. Chem. Soc.* **2012**, *134*, 5222-5232.

150. Dixon, D. A.; Calabrese, J. C.; Miller, J. S., Crystal and Molecular Structure of the 2:1 Charge-Transfer Salt of Decamethylferrocene and Perfluoro-7,7,8,8-Tetracyano-P-Quinodimethane: [[Fe(C5Me5)2]+.cntdot.]2[TCNQF4]2-. The Electronic Structure of [TCNQF4]N (N = 0, 1-, 2-). *J. Phys. Chem.* **1989**, *93*, 2284-2291.

151. Kwaan, R. J.; Harlan, C. J.; Norton, J. R., Generation and Characterization of the Tris(Pentafluorophenyl)Borane Radical Anion. *Organometallics* **2001**, *20*, 3818-3820.

152. McFarland, F. M.; Bonnette, L. R.; Acres, E. A.; Guo, S., The Impact of Aggregation on the P-Doping Kinetics of Poly(3-Hexylthiophene). *J. Mater. Chem. C* **2017**, *5*, 5764-5771.

153. Tsoi, W. C., et al., Effect of Crystallization on the Electronic Energy Levels and Thin Film Morphology of P3HT:Pcbm Blends. *Macromolecules* **2011**, *44*, 2944-2952.

154. Skompska, M.; Szkurłat, A., The Influence of the Structural Defects and Microscopic Aggregation of Poly(3-Alkylthiophenes) on Electrochemical and Optical Properties of the Polymer Films: Discussion of an Origin of Redox Peaks in the Cyclic Voltammograms. *Electrochim. Acta* **2001**, *46*, 4007-4015.

155. Gao, J.; Roehling, J. D.; Li, Y.; Guo, H.; Moulé, A. J.; Grey, J. K., The Effect of 2,3,5,6-Tetrafluoro-7,7,8,8-Tetracyanoquinodimethane Charge Transfer Dopants on the Conformation and Aggregation of Poly(3-Hexylthiophene). *J. Mater. Chem. C* **2013**, *1*, 5638-5646.

156. Rughooputh, S. D. D. V.; Hotta, S.; Heeger, A. J.; Wudl, F., Chromism of Soluble Polythienylenes. *J. Polym. Sci., Part B: Polym. Phys.* **1987**, *25*, 1071-1078.

157. Xu, W.; Li, L.; Tang, H.; Li, H.; Zhao, X.; Yang, X., Solvent-Induced Crystallization of Poly(3-Dodecylthiophene): Morphology and Kinetics. *The Journal of Physical Chemistry B* **2011**, *115*, 6412-6420.

158. Yamamoto, T., et al., Extensive Studies on Π-Stacking of Poly(3-Alkylthiophene-2,5-Diyl)S and Poly(4-Alkylthiazole-2,5-Diyl)S by Optical Spectroscopy, NMR Analysis, Light Scattering Analysis, and X-Ray Crystallography. *J. Am. Chem. Soc.* **1998**, *120*, 2047-2058.

159. Kiriy, N., et al., One-Dimensional Aggregation of Regioregular Polyalkylthiophenes. *Nano Lett.* **2003**, *3*, 707-712.

160. Gallaher, J. K.; Chen, K.; Huff, G. S.; Prasad, S. K. K.; Gordon, K. C.; Hodgkiss, J. M., Evolution of Nonmirror Image Fluorescence Spectra in Conjugated Polymers and Oligomers. *J. Phys. Chem. Lett.* **2016**, *7*, 3307-3312.

161. Sperlich, A.; Kraus, H.; Deibel, C.; Blok, H.; Schmidt, J.; Dyakonov, V., Reversible and Irreversible Interactions of Poly(3-Hexylthiophene) with Oxygen Studied by Spin-Sensitive Methods. *The Journal of Physical Chemistry B* **2011**, *115*, 13513-13518.

162. Reichardt, C., Solvatochromic Dyes as Solvent Polarity Indicators. *Chem. Rev.* **1994**, *94*, 2319-2358.

163. Yurash, B., et al., Towards Understanding the Doping Mechanism of Organic Semiconductors by Lewis Acids. *Nat. Mater.* **2019**, *18*, 1327–1334.

164. Manceau, M.; Rivaton, A.; Gardette, J.-L.; Guillerez, S.; Lemaître, N., The Mechanism of Photo- and Thermooxidation of Poly(3-Hexylthiophene) (P3HT) Reconsidered. *Polym. Degrad. Stab.* **2009**, *94*, 898-907.

165. Kim, J.; Kim, G.; Choi, Y.; Lee, J.; Heum Park, S.; Lee, K., Light-Soaking Issue in Polymer Solar Cells: Photoinduced Energy Level Alignment at the Sol-Gel Processed Metal Oxide and Indium Tin Oxide Interface. *J. Appl. Phys.* **2012**, *111*, 114511.

166. Lim, F. J.; Set, Y. T.; Krishnamoorthy, A.; Ouyang, J.; Luther, J.; Ho, G. W., Addressing the Light-Soaking Issue in Inverted Organic Solar Cells Using Chemical Bath Deposited Fluorinated Tiox Electron Transport Layer. *Journal of Materials Chemistry A* **2015**, *3*, 314-322.

167. Stephan, D. W., “Frustrated Lewis Pairs”: A Concept for New Reactivity and Catalysis. *Organic & Biomolecular Chemistry* **2008**, *6*, 1535-1539.

168. Heun, S.; Mahrt, R. F.; Greiner, A.; Lemmer, U.; Bassler, H.; Halliday, D. A.; Bradley, D. D. C.; Burn, P. L.; Holmes, A. B., Conformational Effects in Poly(P-Phenylene Vinylene)S Revealed by Low-Temperature Site-Selective Fluorescence. *J. Phys.: Condens. Matter* **1993**, *5*, 247-260.

169. Guo, J.; Ohkita, H.; Benten, H.; Ito, S., Charge Generation and Recombination Dynamics in Poly(3-Hexylthiophene)/Fullerene Blend Films with Different Regioregularities and Morphologies. *J. Am. Chem. Soc.* **2010**, *132*, 6154-6164.

170. Beljonne, D.; Cornil, J.; Sirringhaus, H.; Brown, P. J.; Shkunov, M.; Friend, R. H.; Brédas, J. L., Optical Signature of Delocalized Polarons in Conjugated Polymers. *Adv. Funct. Mater.* **2001**, *11*, 229-234.

171. Valencia, A. M.; Cocchi, C., Electronic and Optical Properties of Oligothiophene-F4TCNQ Charge-Transfer Complexes: The Role of the Donor Conjugation Length. *J. Phys. Chem. C* **2019**, *123*, 9617-9623.

172. Yee, P. Y.; Scholes, D. T.; Schwartz, B. J.; Tolbert, S. H., Dopant-Induced Ordering of Amorphous Regions in Regiorandom P3HT. *J. Phys. Chem. Lett.* **2019**, *10*, 4929-4934.

173. Mansour, A. E.; Lungwitz, D.; Schultz, T.; Arvind, M.; Valencia, A. M.; Cocchi, C.; Opitz, A.; Neher, D.; Koch, N., The Optical Signatures of Molecular-Doping Induced Polarons in Poly(3-Hexylthiophene-2,5-Diyl): Individual Polymer Chains Versus Aggregates. *J. Mater. Chem. C* **2020**, *8*, 2870-2879.

174. Aguirre, A.; Gast, P.; Orlinskii, S.; Akimoto, I.; Groenen, E. J. J.; El Mkami, H.; Goovaerts, E.; Van Doorslaer, S., Multifrequency EPR Analysis of the Positive Polaron in I2-Doped Poly(3-Hexylthiophene) and in Poly[2-Methoxy-5-(3,7-Dimethyloctyloxy)]-1,4-Phenylenevinylene. *PCCP* **2008**, *10*, 7129-7138.

175. Sproules, S.; Banerjee, P.; Weyhermüller, T.; Yan, Y.; Donahue, J. P.; Wieghardt, K., Monoanionic Molybdenum and Tungsten Tris(Dithiolene) Complexes: A Multifrequency EPR Study. *lnorg. Chem.* **2011**, *50*, 7106-7122.

176. Fekl, U.; Sarkar, B.; Kaim, W.; Zimmer-De Iuliis, M.; Nguyen, N., Tuning of the Spin Distribution between Ligand- and Metal-Based Spin: Electron Paramagnetic Resonance of Mixed-Ligand Molybdenum Tris(Dithiolene) Complex Anions. *lnorg. Chem.* **2011**, *50*, 8685-8687.

177. Tomkiewicz, Y.; Taranko, A. R.; Torrance, J. B., Spin Susceptibility of Tetrathiafulvalene Tetracyanoquinodimethane, TTF-TCNQ, in the Semiconducting Regime: Comparison with Conductivity. *Phys. Rev. B* **1977**, *15*, 1017-1023.

178. Nordio, P. L.; Soos, Z. G.; McConnell, H. M., Spin Excitations in Ionic Molecular Crystals. *Annu. Rev. Phys. Chem.* **1966**, *17*, 237-260.

179. Hoffman, B. M.; Hughes, R. C., ESR of TMPD–TCNQ: Spin Excitations of the Heisenberg Regular Linear Chain. *J. Chem. Phys.* **1970**, *52*, 4011-4023.

180. Kampar, E.; Neilands, O., Degree of Charge Transfer in Donor–Acceptor Systems of the Π–Π Type. *Russ. Chem. Rev.* **1986**, *55*, 334-342.

181. Pingel, P.; Zhu, L.; Park, K. S.; Vogel, J.-O.; Janietz, S.; Kim, E.-G.; Rabe, J. P.; Brédas, J.-L.; Koch, N., Charge-Transfer Localization in Molecularly Doped Thiophene-Based Donor Polymers. *J. Phys. Chem. Lett.* **2010**, *1*, 2037-2041.

182. H. Doerrer, L.; L. H. Green, M., Oxidation of [M(H-C5H5)2], M = Cr, Fe or Co, by the New Brønsted Acid H2O·B(C6F5)3 Yielding the Salts [M(H-C5H5)2]+a–, Where a– = [(C6F5)3b(μ-Oh)B(C6F5)3]– or [(C6F5)3BOH · · · H2OB(C6F5)3]–†. *J. Chem. Soc., Dalton Trans.* **1999**, 4325-4329.

183. Zhao, W.; Sun, J., Triflimide (Hntf2) in Organic Synthesis. *Chem. Rev.* **2018**, *118*, 10349-10392.

184. Hofmann, A. I.; Kroon, R.; Yu, L.; Müller, C., Highly Stable Doping of a Polar Polythiophene through Co-Processing with Sulfonic Acids and Bistriflimide. *J. Mater. Chem. C* **2018**, *6*, 6905-6910.

185. Han, C. C.; Elsenbaumer, R. L., Protonic Acids: Generally Applicable Dopants for Conducting Polymers. *Synth. Met.* **1989**, *30*, 123-131.

186. Valencia, D.; Whiting, G. T.; Bulo, R. E.; Weckhuysen, B. M., Protonated Thiophene-Based Oligomers as Formed within Zeolites: Understanding Their Electron Delocalization and Aromaticity. *PCCP* **2016**, *18*, 2080-2086.

187. Ghani, F.; Opitz, A.; Pingel, P.; Heimel, G.; Salzmann, I.; Frisch, J.; Neher, D.; Tsami, A.; Scherf, U.; Koch, N., Charge Transfer in and Conductivity of Molecularly Doped Thiophene-Based Copolymers. *J. Polym. Sci., Part B: Polym. Phys.* **2015**, *53*, 58-63.

188. Niklas, J., et al., Highly-Efficient Charge Separation and Polaron Delocalization in Polymer-Fullerene Bulk-Heterojunctions: A Comparative Multi-Frequency EPR and DFT Study. *PCCP* **2013**, *15*, 9562-9574.

189. Steyrleuthner, R.; Zhang, Y.; Zhang, L.; Kraffert, F.; Cherniawski, B. P.; Bittl, R.; Briseno, A. L.; Bredas, J.-L.; Behrends, J., Impact of Morphology on Polaron Delocalization in a Semicrystalline Conjugated Polymer. *PCCP* **2017**, *19*, 3627-3639.

190. Ratcliff, E. L.; Lee, P. A.; Armstrong, N. R., Work Function Control of Hole-Selective Polymer/ITO Anode Contacts: An Electrochemical Doping Study. *J. Mater. Chem.* **2010**, *20*, 2672-2679.

191. Enengl, C.; Enengl, S.; Pluczyk, S.; Havlicek, M.; Lapkowski, M.; Neugebauer, H.; Ehrenfreund, E., Doping-Induced Absorption Bands in P3HT: Polarons and Bipolarons. *ChemPhysChem* **2016**, *17*, 3836-3844.

192. Scholes, D. T.; Yee Patrick, Y.; Lindemuth Jeffrey, R.; Kang, H.; Onorato, J.; Ghosh, R.; Luscombe Christine, K.; Spano Frank, C.; Tolbert Sarah, H.; Schwartz Benjamin, J., The Effects of Crystallinity on Charge Transport and the Structure of Sequentially Processed F4TCNQ-Doped Conjugated Polymer Films. *Adv. Funct. Mater.* **2017**, *27*, 1702654.

193. Colaneri, N.; Nowak, M.; Spiegel, D.; Hotta, S.; Heeger, A. J., Bipolarons in Poly(3-Methylthiophene): Spectroscopic, Magnetic, and Electrochemical Measurements. *Phys. Rev. B* **1987**, *36*, 7964-7968.

194. Ziemelis, K. E.; Hussain, A. T.; Bradley, D. D. C.; Friend, R. H.; Rühe, J.; Wegner, G., Optical Spectroscopy of Field-Induced Charge in Poly(3-Hexyl Thienylene) Metal-Insulator-Semiconductor Structures: Evidence for Polarons. *Phys. Rev. Lett.* **1991**, *66*, 2231-2234.

195. Prosa, T. J.; Winokur, M. J.; Moulton, J.; Smith, P.; Heeger, A. J., X-Ray Structural Studies of Poly(3-Alkylthiophenes): An Example of an Inverse Comb. *Macromolecules* **1992**, *25*, 4364-4372.

196. Liu, J.; Arif, M.; Zou, J.; Khondaker, S. I.; Zhai, L., Controlling Poly(3-Hexylthiophene) Crystal Dimension: Nanowhiskers and Nanoribbons. *Macromolecules* **2009**, *42*, 9390-9393.

197. Aziz, E. F.; Vollmer, A.; Eisebitt, S.; Eberhardt, W.; Pingel, P.; Neher, D.; Koch, N., Localized Charge Transfer in a Molecularly Doped Conducting Polymer. *Adv. Mater.* **2007**, *19*, 3257-3260.

198. Harrelson, T. F.; Cheng, Y. Q.; Li, J.; Jacobs, I. E.; Ramirez-Cuesta, A. J.; Faller, R.; Moulé, A. J., Identifying Atomic Scale Structure in Undoped/Doped Semicrystalline P3HT Using Inelastic Neutron Scattering. *Macromolecules* **2017**, *50*, 2424-2435.

199. Hamidi-Sakr, A.; Biniek, L.; Bantignies, J. L.; Maurin, D.; Herrmann, L.; Leclerc, N.; Lévêque, P.; Vijayakumar, V.; Zimmermann, N.; Brinkmann, M., A Versatile Method to Fabricate Highly in-Plane Aligned Conducting Polymer Films with Anisotropic Charge Transport and Thermoelectric Properties: The Key Role of Alkyl Side Chain Layers on the Doping Mechanism. *Adv. Funct. Mater.* **2017**, *27*, 1700173.

200. Liu, W.; Müller, L.; Ma, S.; Barlow, S.; Marder, S. R.; Kowalsky, W.; Köhn, A.; Lovrincic, R., Origin of the Π–Π Spacing Change Upon Doping of Semiconducting Polymers. *J. Phys. Chem. C* **2018**, *122*, 27983-27990.

201. Thelen, J. L.; Wu, S.-L.; Javier, A. E.; Srinivasan, V.; Balsara, N. P.; Patel, S. N., Relationship between Mobility and Lattice Strain in Electrochemically Doped Poly(3-Hexylthiophene). *ACS Macro Lett.* **2015**, *4*, 1386-1391.

202. Guardado, J. O.; Salleo, A., Structural Effects of Gating Poly(3-Hexylthiophene) through an Ionic Liquid. *Adv. Funct. Mater.* **2017**, *27,* 1701791.

203. McFarland, F. M.; Ellis, C. M.; Guo, S., The Aggregation of Poly(3-Hexylthiophene) into Nanowires: With and without Chemical Doping. *J. Phys. Chem. C* **2017**, *121*, 4740-4746.

204. Sun, S.; Salim, T.; Wong, L. H.; Foo, Y. L.; Boey, F.; Lam, Y. M., A New Insight into Controlling Poly(3-Hexylthiophene) Nanofiber Growth through a Mixed-Solvent Approach for Organic Photovoltaics Applications. *J. Mater. Chem.* **2011**, *21*, 377-386.

205. Chew, A. R.; Ghosh, R.; Shang, Z.; Spano, F. C.; Salleo, A., Sequential Doping Reveals the Importance of Amorphous Chain Rigidity in Charge Transport of Semi-Crystalline Polymers. *J. Phys. Chem. Lett.* **2017**, *8*, 4974-4980.

206. Jacobs, I. E.; Li, J.; Burg, S. L.; Bilsky, D. J.; Rotondo, B. T.; Augustine, M. P.; Stroeve, P.; Moulé, A. J., Reversible Optical Control of Conjugated Polymer Solubility with Sub-Micrometer Resolution. *ACS Nano* **2015**, *9*, 1905-1912.

207. Fujimoto, R.; Yamashita, Y.; Kumagai, S.; Tsurumi, J.; Hinderhofer, A.; Broch, K.; Schreiber, F.; Watanabe, S.; Takeya, J., Molecular Doping in Organic Semiconductors: Fully Solution-Processed, Vacuum-Free Doping with Metal-Organic Complexes in an Orthogonal Solvent. *J. Mater. Chem. C* **2017**, *5*, 12023-12030.

208. Ingram, I. D. V.; Tate, D. J.; Parry, A. V. S.; Sebastian Sprick, R.; Turner, M. L., A Simple Method for Controllable Solution Doping of Complete Polymer Field-Effect Transistors. *Appl. Phys. Lett.* **2014**, *104*, 153304.

209. Hynynen, J.; Kiefer, D.; Müller, C., Influence of Crystallinity on the Thermoelectric Power Factor of P3HT Vapour-Doped with F4TCNQ. *RSC Adv.* **2018**, *8*, 1593-1599.

210. Arkhipov, V. I.; Heremans, P.; Emelianova, E. V.; Bässler, H., Effect of Doping on the Density-of-States Distribution and Carrier Hopping in Disordered Organic Semiconductors. *Phys. Rev. B* **2005**, *71*, 045214.

211. Noriega, R.; Rivnay, J.; Vandewal, K.; Koch, F. P. V.; Stingelin, N.; Smith, P.; Toney, M. F.; Salleo, A., A General Relationship between Disorder, Aggregation and Charge Transport in Conjugated Polymers. *Nat Mater* **2013**, *12*, 1038-1044.

212. Wang, T.; Pearson, A. J.; Lidzey, D. G.; Jones, R. A. L., Evolution of Structure, Optoelectronic Properties, and Device Performance of Polythiophene:Fullerene Solar Cells During Thermal Annealing. *Adv. Funct. Mater.* **2011**, *21*, 1383-1390.

213. Aguirre Jordan, C.; Hawks Steven, A.; Ferreira Amy, S.; Yee, P.; Subramaniyan, S.; Jenekhe Samson, A.; Tolbert Sarah, H.; Schwartz Benjamin, J., Sequential Processing for Organic Photovoltaics: Design Rules for Morphology Control by Tailored Semi-Orthogonal Solvent Blends. *Advanced Energy Materials* **2015**, *5*, 1402020.

214. Kroon, R.; Kiefer, D.; Stegerer, D.; Yu, L.; Sommer, M.; Müller, C., Polar Side Chains Enhance Processability, Electrical Conductivity, and Thermal Stability of a Molecularly P-Doped Polythiophene. *Adv. Mater.* **2017**, *29*, 1700930.

215. Watts, K. E.; Neelamraju, B.; Moser, M.; McCulloch, I.; Ratcliff, E. L.; Pemberton, J. E., Thermally Induced Formation of Hf4tcnq– in F4TCNQ-Doped Regioregular P3HT. *J. Phys. Chem. Lett.* **2020**, *11*, 6586-6592.

216. Li, J.; Rochester, C. W.; Jacobs, I. E.; Aasen, E. W.; Friedrich, S.; Stroeve, P.; Moulé, A. J., The Effect of Thermal Annealing on Dopant Site Choice in Conjugated Polymers. *Org. Electron.* **2016**, *33*, 23-31.

217. Frisch, M. J., et al. *Gaussian 16*, Wallingford, CT, 2016.

218. Yanai, T.; Tew, D. P.; Handy, N. C., A New Hybrid Exchange–Correlation Functional Using the Coulomb-Attenuating Method (CAM-B3LYP). *Chem. Phys. Lett.* **2004**, *393*, 51-57.

219. Grimme, S.; Antony, J.; Ehrlich, S.; Krieg, H., A Consistent and Accurate Ab Initio Parametrization of Density Functional Dispersion Correction (DFT-D) for the 94 Elements H-Pu. *J. Chem. Phys.* **2010**, *132*, 154104.

220. Cammi, R.; Mennucci, B., Linear Response Theory for the Polarizable Continuum Model. *J. Chem. Phys.* **1999**, *110*, 9877-9886.

Acknowledgement

The successful completion of this work would have been impossible without the contribution, support, and encouragement of several people.

First of all, I would like to sincerely thank my supervisor Prof. Dieter Neher for giving me the opportunity to work in his group, encouraging me to participate in several scientific conferences, and critically analyzing my results. His guidance, support and encouragement were instrumental in shaping this work. Thank you, Dieter!

Thanks to Prof. Thuc-Quyen Nguyen and Prof. Sabine Ludwigs for agreeing to review this thesis.

I am extremely grateful to all our scientific collaborators for their valuable inputs over the years.

I'd like to thank our FoMEDOS project partners at the *Humboldt-Universität zu Berlin*: Norbert Koch and Caterina Cocchi, for their fruitful discussions about molecular doping of organic semiconductors. In particular, I appreciate the help of Ahmed Mansour for the FTIR measurements and Michele Guerrini for providing the DFT results presented in this thesis. Many thanks to Ingo Salzmann who was initially in this project, for carrying out the GIXRD measurements and raising important questions in the early stages of this work.

Thanks are due to Jan Behrends and team at *Freie Universität Berlin* for the support provided through EPR measurements and discussions. My deepest, sincere thanks go to Claudia Tait, who performed the EPR and ENDOR measurements and analysis that were key towards elucidating the doping process in our dopant:host systems. Thank you for agreeing to repeat the measurements numerous times until we figured out what was going on, for patiently and meticulously reviewing the several drafts of our research paper, for providing feedback on my thesis, for your insightful comments and wisdom. I must also acknowledge the EPR insights and discussions about BCF-rreP3HT gained initially through the work of Kelvin Yao and Robert Steyrleuthner, which helped me realize that it wasn't me, but the system that behaved inconsistently (that was a huge relief!).

This work benefited greatly from having the molybdenum-based dopant that was provided by Seth Marder's group at *Georgia Tech, USA*. Many thanks to Seth and Steve Barlow, for their critical feedback on our work and providing a chemist's perspective.

I must also thank our collaborators who are close by at the *Fraunhofer IAP* in Golm: Silvia Janietz for lending us their 4PP setup for a few months, and Patrick Pingel, who originally initiated our interest in BCF, for providing guidance and direction in the initial stages of my work.

I wish to gratefully acknowledge the Deutsche Forschungsgemeinschaft (DFG) for having funded my research work.

My work in Potsdam would have been incredibly hard and dull without the help and support of the wonderful members of the "Physik weiche Materie" group, past and present.

Special thanks to Frank, for educating me about how to properly use the instruments and equipment, for always being ready and able to resolve issues with them, and answering my numerous questions. Thanks to Andreas Horka for helping me procure materials and equipment for the lab, and always greeting me with a cheerful smile. I am grateful to Burkhard for teaching me how to collect nice AFM images, Florian for his help with the metal evaporators and 4PP setup, and Elke for taking care of all the paperwork. Thanks to APu for building the 4PP setup, and always accompanying me enthusiastically for lunch (I will miss our routine lunches at the Mensa!). Thanks to Steffen for training me, and instilling good lab etiquettes in me when I first joined this group as a student assistant. Many thanks to Elisa for taking an interest in my work, providing valuable feedback and encouragement, reviewing parts of this thesis, and being a great friend outside of work (I miss our after-work Zumba sessions!). Thanks to Ulli for his friendship, wisdom and encouragement, particularly when I was facing hardships. Many thanks to Lorena for her help and support in the labs; whether in the reconfiguration of the conductivity setup, or for checking if I had forgotten anything when I rushed to catch the train. Thank you for listening to my work-woes and organizing fun activities outside of work (those karaoke nights at Schlachtensee were the best!). Thanks also to Meysam for being a good listener and friend, through good times and bad times. Several others in the group have helped me in some way or the other, but this list would go on if I were to mention them all. Instead: thank you all for enriching my work life in Golm during the last few years!

My heartfelt thanks to all my other friends and my relatives in India, Europe and USA for providing the much needed distraction from my PhD life. I couldn’t have done it without your encouragement and support!

I am forever indebted to my parents. You have supported me through everything, and always given me the freedom and facilities to choose my path and realize my potential. Words aren’t enough to express my gratitude. Special thanks to my brother and sister for their unwavering faith in me that has served as a constant source of motivation.

Last but not the least, I would like to thank my husband Anupam, for believing that I could do this even when I didn’t myself, for keeping me accountable, for cycling 40 km (one way!) in the middle of a pandemic to retrieve my lab books from a friend, so that I could focus on writing, for questioning my limiting beliefs, and being my best friend. Without you, I wouldn’t be what I am today.

Eigenständigkeitserklärung

Ich erkläre hiermit, dass ich diese Arbeit selbstständig verfasst und keine anderen als die angegebenen Hilfsmittel benutzt habe. Diese Arbeit wurde an keiner anderen Hochschule eingereicht.

Potsdam, den

Malavika Arvind